Spring 5-15-2018

Development and Function of Retinal Ganglion Cell Circuits

Nai-Wen Tien
Washington University in St. Louis

WASHINGTON UNIVERSITY IN ST. LOUIS

Division of Biology and Biomedical Sciences
Neurosciences

Dissertation Examination Committee:
Daniel Kerschensteiner, Chair
Timothy E. Holy
Peter D. Lukasiewicz
Steven J. Mennerick
Josh L. Morgan

Development and Function of Retinal Ganglion Cell Circuits

by
Nai-Wen Tien

A dissertation presented to
The Graduate School
of Washington University in
partial fulfillment of the
requirements for the degree
of Doctor of Philosophy

May 2018
St. Louis, Missouri

Table of Contents

List of Figures

Acknowledgments

I would like to express my appreciation to the many people who contributed to my wonderful time in graduate school. This dissertation would not have been possible without the support I received from my many mentors, lab mates, friends and family.

Special mention first goes to my PhD advisor, Daniel Kerschensteiner: You have not only been an excellent scientific role model, but also the best mentor in the world. Thank you for your guidance and endless patience, and for giving me so many wonderful research experiences and opportunities. During these 5 years, I learned how to ask and approach strong scientific questions, as well as how to tell compelling stories from my data. I will miss the time we spent during our weekly one-on-one meetings, both discussing science and arguing why pink is a reasonable color for presenting data. I credit you with the scientific growth I have made over the course of my graduate career, despite my taste in color.

I gratefully acknowledge my dissertation committee members: Drs. Tim Holy, Peter Lukasiewicz, Steve Mennerick and Josh Morgan. Thank you for giving me insightful feedback on my research, for providing valuable advice on my career development, and for teaching me how to be a better speaker and writer. I sincerely hope that I can continue to rely on you as mentors as I continue my adventure in science.

I would also like to thank all members of the Kerschensteiner lab, past and present, for inspiring me scientifically and supporting me spiritually. I would particularly like to acknowledge Lei Zhao: thank you for always being there when I need help for experiments and when I am hungry. I will miss you (and your food). Please do not forget the promise we made to one another.

Thank you to all my friends for your support and encouragement throughout graduate school. Special thanks to Chia-Hsin Chen and Yi-Lin Hu: thank you for always patiently listening to my excited stories about experiments, for cheering me up during dark times, and for making my PhD an unforgettable journey.

Lastly, but most importantly, I thank my family. I am grateful for my aunt, Tina: thank you for traveling to St. Louis to help me settle down and find my home when I started my PhD. Thank you to my mom, dad, and sister, Fei-Wen, for raising me in such a loving environment and showing me how to live with integrity. Thank you for always supporting me and encouraging me to pursue my dreams without expecting anything in return. I am so lucky to be your daughter and your sister. I love you.

Nai-Wen Tien

Washington University in St. Louis

May 2018

Dedicated to Santiago Ramón y Cajal.

ABSTRACT OF THE DISSERTATION

Development and Function of Retinal Ganglion Cells Circuits

by

Nai-Wen Tien

Doctor of Philosophy in Biology and Biomedical Sciences

Neurosciences

Washington University in St. Louis, 2018

Associate Professor Daniel Kerschensteiner, Chair

The function of our nervous system relies on specific patterns of synaptic connections between diverse neuronal cell types. My thesis research addressed how cell-type-specific patterns of connectivity emerge in the developing mouse retina and how they enable mature retinal neurons to detect specific sensory stimuli.

Spike trains of the approximately 40 retinal ganglion cell (RGC) types in mammals encode specific features and events in the visual world, and are the sole source of visual information to the brain. Recent studies have begun to dissect the presynaptic circuits underlying diverse RGC light responses, but how cell-type-specific retinal circuits emerge during development is poorly understood. The first part of my dissertation explored the plasticity of the ON alpha (ONα-) RGC circuit. I found that developmental removal of the dominant excitatory input to ONα-RGCs triggers cell-type-specific rewiring, which precisely preserves ONα-RGCs' characteristic light responses including high contrast sensitivity.

Spiking neurons, including RGCs, typically encode sensory information by increasing firing rates in the presence of preferred stimuli. Suppressed-by-Contrast (SbC-) RGCs are unique in that they signal changes in luminance (i.e., contrast) by decreasing rather than increasing

spiking. Taking advantages of mouse genetics, in the second part of my thesis, I characterized SbC-RGCs' responses to complex stimuli and identified the synaptic mechanisms underlying their suppressive contrast encoding. Interestingly, I found that VGluT3-expressing amacrine cells (VG3-ACs) are dual transmitter neurons that release excitatory and inhibitory transmitters in a target-specific manner, and VG3-ACs specifically contributes to OFF inhibition to SbC-RGCs in response to small stimuli. Finally, using an intersectional transgenic approach, I preferentially labeled SbC-RGCs and mapped their central projections to explore the contribution of SbC-RGCs to vision.

Chapter 1 : Introduction

1.1 Homeostatic Plasticity in Developing Neural Circuits

Throughout life, neural circuits undergo changes in connectivity, especially during development, when neurons frequently extend and retract dendrites and axons, and form and eliminate synapses. Thus, nervous systems face a constant challenge: how to maintain flexibility and stability at the same time. Neural circuits must stay flexible to allow for changes in connectivity and synaptic strength. As changes in connectivity push neural circuits away from equilibrium, they need to maintain their activity within a working range and avoid extremes of quiescence and saturation. Functional stability is maintained by homeostatic plasticity, which is defined broadly as a set of neuronal changes that restore activity to a setpoint following a perturbation (Davis 2013, Turrigiano & Nelson 2004). Recent studies have identified diverse homeostatic plasticity mechanisms triggered by a variety of perturbations. These mechanisms regulate dendritic and axonal connectivity of a neuron, as well as its intrinsic excitability (Desai et al 2002, Grubb & Burrone 2010, Turrigiano et al 1998).

In addition to maintaining the activity of individual neurons, homeostatic plasticity can act at a network level to coordinate changes in connectivity and excitability across multiple neurons in a circuit to stabilize its function (Maffei & Fontanini 2009, Slomowitz et al 2015). Recent advances in single-cell RNA sequencing together with large-scale morphological and functional surveys have identified diverse excitatory and inhibitory cell types, which serve distinct circuit functions (Cembrowski et al 2016, Tasic et al 2016). With those technical advances, several studies have shown that homeostatic plasticity can act in a cell-type-specific

manner to stabilize circuit activity (Bartley et al 2008, Maffei et al 2004). While it is evident that homeostatic plasticity stabilizes average firing rates, how homeostatic plasticity regulates specific sensory computations of neural circuits is not known.

1.2 Visual Information Processing Pathways

Vision does not strive for a comprehensive and physically accurate representation of the world like cameras do; instead, our visual systems extract salient features to represent relevant information while discarding irrelevant information (Field et al 1993). Visual signals diverge and converge across subsequent stages of visual processing, starting in the retina (Gollisch & Meister 2010, Masland & Martin 2007). As discussed in more detail in the following sections, the outcomes of retinal circuit computations are encoded in spike trains of distinct retinal ganglion cells (RGC) types. Different RGC types transmit distinct information to diverse subcortical targets (Berson 2008, Chalupa & Williams 2008, Van Essen et al 1992). The retinogeniculate pathway is one of the major visual pathways in mammals, transmitting information from the retina to the primary visual cortex (V1) via the dorsal lateral geniculate nucleus (dLGN) of the thalamus. Another prominent retinorecipient target is the superior colliculus (SC), which is involved in directing gaze to visual targets. Neurons locating in the superficial layers of the SC also project to the dorsal lateral geniculate nucleus (dLGN) and pulvinar, the latter also connecting to V1 and extrastriate visual cortex (Berson 2008, Seabrook et al 2017, Van Essen et al 1992). In addition to image-forming circuits, RGCs project to subcortical areas serving non-image-forming functions, such as the accessory optic system, which mediates gaze-stabilizing eye movements, the olivary pretectal nucleus for the pupillary light reflex, and the suprachiasmatic nucleus for the entrainment of circadian rhythms (Berson 2008).

While historically insights into visual processing mostly came from cats, macaques, and rabbits, recently studies of the mouse visual system have accelerated progress in understanding the neural basis of vision, owing to the powerful genetic tools, the capacity of large-scale monitoring neural activity, and a growing number of behavioral assays available in mice (Huberman & Niell 2011, Seabrook et al 2017, Wang & Krauzlis 2018). Despite differences in visual acuity, recent anatomical and physiological findings of mouse visual systems reveal a high degree of similarities between mice and primates, in the eye and in the brain (Chalupa & Williams 2008, Glickfeld et al 2014, Huberman & Niell 2011, Masland 2001a, Niell & Stryker 2008, Van Hooser 2007). These similarities allow us to use mice as a model system to address fundamental questions and identify core principles of visual processing (Huberman & Niell 2011).

1.3 Fundamental Organization of the Retina

The retina is part of the CNS and sits at back of the eye looking out onto the world. As light falls onto the retina, it converts light information into electrical signals that the brain can interpret. The retina, which is approximately 200 µm thick, is a highly structured and densely packed neural tissue (Masland 2001a, Masland 2012a). Mammalian retina consists of five major neural classes: photoreceptors, horizontal cells (HCs), bipolar cells (BCs), amacrine cells (ACs) and RGCs. These five neural classes organize in three somatic layers and two synaptic layers, directing information flow into vertical propagation (photoreceptors to BCs to RGCs) and horizontal modulation (HCs and ACs) (Fig. 1.1).

The outer nuclear layer (ONL) contains the somata of photoreceptors, rods and cones, which are activated at dim and bright light levels, respectively (Kefalov 2012). In the dark,

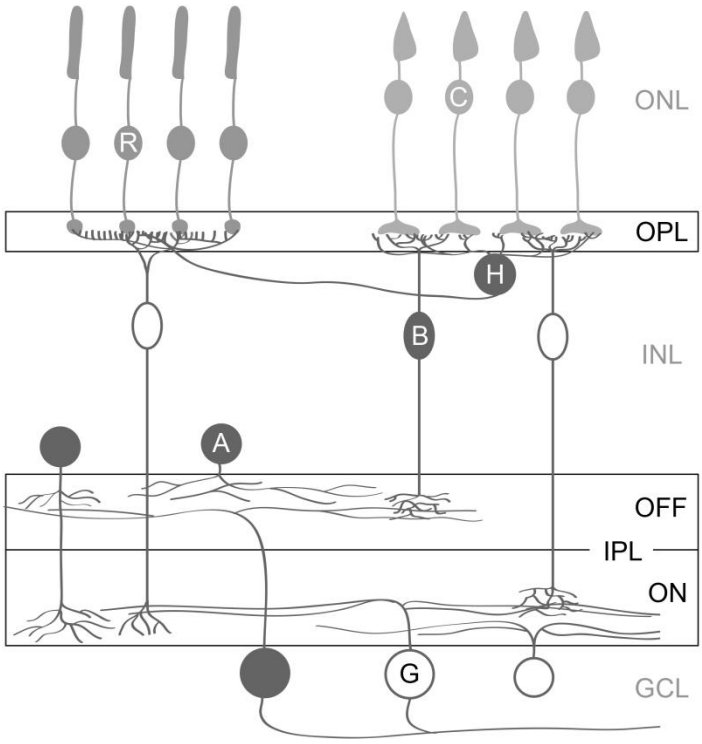

Figure 1.1 Fundamental organization of the mammalian retina

Rod (R) and cone (C) photoreceptors reside in the outer nuclear layer (ONL), and provide inputs to horizontal (H) cells and bipolar (B) cells in the outer plexiform layer (OPL). The inner nuclear layer (INL) contains horizontal cells, bipolar cells and amacrine (A) cells. Bipolar cells and amacrine cells connect to the retinal output neurons, retinal ganglion cells (G) in the inner plexiform layer (IPL), which can be subdivided into ON and OFF sublaminae.

photoreceptors are depolarized and release neurotransmitter glutamate constantly (Arshavsky et al 2002, Ebrey & Koutalos 2001). Upon illumination, photon absorption by visual pigments in the photoreceptor outer segments initiates a transduction cascade that results in membrane hyperpolarization, decreasing glutamate in proportion to increases in light intensity. Photoreceptors synapse onto HCs and BCs in the outer plexiform layer (OPL). HCs reside at the outer edge of the inner nuclear layer (INL) and provide negative feedback to photoreceptor terminals (Masland 2012a). HCs have extensive lateral arborizations and are electrically coupled to their neighbors. HCs, therefore, measure light intensity over large areas and mediate surround suppression of photoreceptors (Chapot et al 2017, Masland 2012a).

BCs reside in the INL, and relay photoreceptor signals from the outer retina to ACs and RGCs in the inner retina. Depending on their glutamate receptor composition in dendrites, BCs can be broadly grouped into ON and OFF BCs, activated by light increment and decrement, respectively (Masland 2001a). OFF BCs express ionotropc glutamate receptors (AMPA/kainite receptors), and undergo membrane depolarization as receiving glutamate from photoreceptors in the dark. By contrast, the metabotropic glutamate receptor 6 (mGluR6) expressed in dendrites of ON BCs "sign-inverte" the signals from photoreceptors (Nawy & Jahr 1990, Nawy & Jahr 1991). Thus, ON BCs hyperpolarize in the dark in response to glutamate, but depolarize in response to light when photoreceptors decrease glutamate release. In mammals including mice, ON and OFF BCs can be distinguished by the stratification of their axonal terminals: ON (OFF) BCs release glutamate and provide excitatory inputs to ON (OFF) ACs and ON (OFF) RGCs in the inner (outer) half of the inner plexiform layer (IPL), respectively. BCs are non-spiking neurons and continuously change glutamate release rates as a function of their membrane potential.

ACs, the most diverse neural class in the retina, also reside in the INL, and shape light responses of BCs, RGCs, and other ACs (Masland 2012a, Masland 2012b). Most ACs are axonless inhibitory neurons. Generally, wide-field ACs are GABAergic and narrow-field ACs are glycinergic, mediating lateral inhibition and vertical "crossover inhibition" in the IPL, respectively (Eggers & Lukasiewicz 2011, Werblin 2011). In addition to fast neurotransmission, ACs can slowly and broadly modulate retinal circuits by releasing dopamine, serotonin, neuropeptides or nitric oxide (Hartveit & Veruki 2012, Marshak 1989, Masland 2012b, Vaney 1986).

RGCs, the retinal output neurons, are located in the innermost layer of the retina and are excitatory spiking neurons. Their dendrites stratify in different layers of the IPL, and receive different combinations of excitatory and inhibitory inputs from BCs and ACs (Masland 2012a). Broadly, ON (OFF) RGCs stratify and receive excitatory inputs from ON (OFF) BCs in the inner (outer) half of the IPL, whereas dendrites of ON-OFF RGCs stratify in both ON and OFF sublaminae. Selective visual features are encoded in patterns of spike activity of individual RGC types, and transmitted to different brain areas, eventually eliciting a variety of visually guided behaviors (Dhande & Huberman 2014, Dhande et al 2015, Seabrook et al 2017).

In sum, the retina is composed of vertical and horizontal pathways: photoreceptors transmit light signals to BCs, which provide excitatory inputs to RGCs. This vertical pathway is modulated by horizontal inhibition from HCs and ACs.

As RGC spikes are the sole source of visual information to the brain, identifying the full complement of RGC types and brain areas each type projects to, characterizing light responses of RGC types, and delineating the circuits underlying these responses are goals fundamental to understanding vision and a major focus of this dissertation.

1.4 Cell-Type Specific Connectivity Gives Rise to Diverse Retinal Circuits

The retina, the first stage of visual processing, is an ideal model system for studying neural computation (Azeredo da Silveira & Roska 2011). The five retinal neuron classes comprise diverse cell types (Fig. 1.2), which assemble into multiple circuits, each detecting specific visual features that are encoded in spike trains of specific RGC types. Anatomical and electrophysiological approaches have identified approximately 40 RGCs in mice (Baden et al

2016, Coombs et al 2006, Dhande et al 2015, Sanes & Masland 2015, Sumbul et al 2014). Connectomic reconstructions, light microscopy, physiological recordings, and genetic tools have revealed that cell-type-specific combinations of presynaptic inputs and intrinsic excitability account for the distinct light response properties of individual RGC types (Dunn & Wong 2014, Helmstaedter et al 2013, Margolis & Detwiler 2007, Morgan et al 2011).

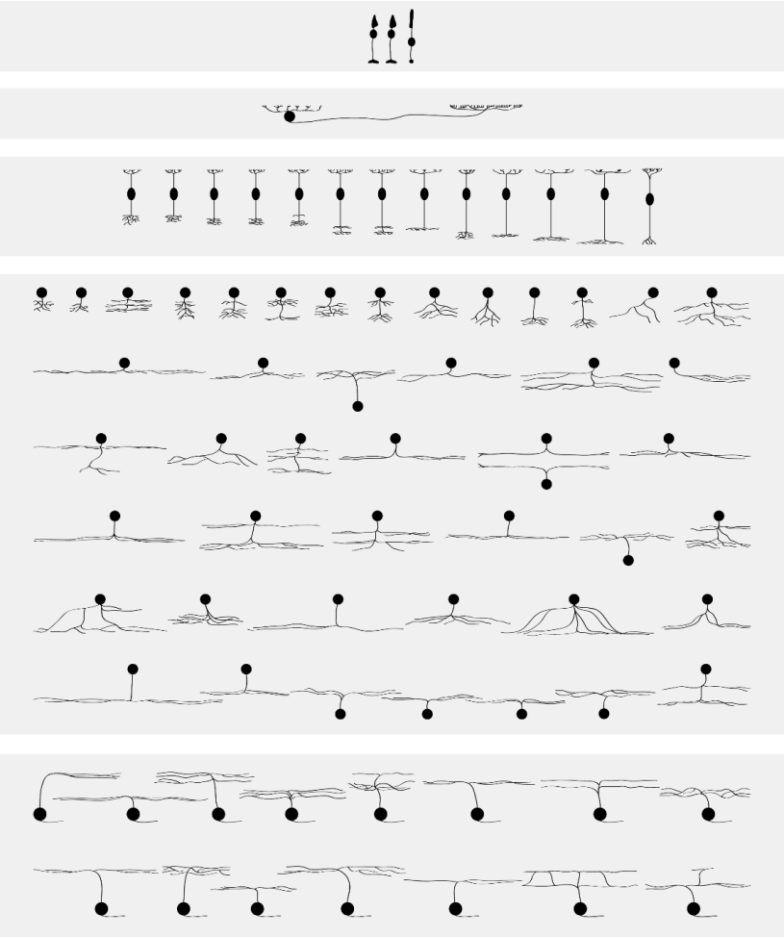

Figure 1.2 Neuronal diversity in the mouse retina

The five retinal neural classes comprise diverse cell types. From the top to the bottom are photoreceptors, horizontal cells, bipolar cells, amacrine cells and retinal ganglion cells. The amenability of mouse genetics enables systematically identification and characterization of individual cell types. The illustration was inspired by Masland (Masland 2001a).

In addition to a single type of rods, mammalian retinas contain two or three types of cones, which express opsin with different absorption spectra and form the basis of color vision (Jacobs 1993, Masland 2001a). The mouse retina contains two types of cones: S cones, which express only short wavelength sensitive (S-) opsin (with peak sensitivity to UV light, 360 nm), and M/S cones, which co-express S- and medium wavelength sensitive (M-, peak 530 nm) opsins (Baden et al 2013b, Haverkamp et al 2005). The distribution of S cones is homogenous across the retina. However, M/S cones express M-opsin (dorsal: high, ventral: low) and S-opsin (dorsal: low, ventral: high) in opposite dorsoventral gradients across the retina (Wang et al 2011). Dichromatic opponency of RGCs can arise by cone-selective connectivity (Marshak & Mills 2014). Type 9 ON BCs (B9 BCs) specifically synapse with S cones and avoid M/S cones, representing blue ON pathway (Haverkamp et al 2005). In M-opsin-dominant dorsal retina, type 1 OFF BCs (B1 BCs) show green-biased responses, and may represent a green OFF pathway (Behrens et al 2016, Breuninger et al 2011). Therefore, specific connections to B1 and B9 BCs in the dorsal retina can render RGCs color opponent. In the opsin transitional zone, where S- and M-opsin gradients in M/S cones invert, color opponent response can arise without cone-type-selective wiring (Chang et al 2013, Marshak & Mills 2014).

In the INL, BCs respond to photoreceptor input differently in contrast and temporal profiles, diversifying visual processing channels beyond ON/OFF and chromatic channels (Euler et al 2014). In mice, 15 BC types, including one rod BCs (RBCs), have been identified, each stratifying and thus providing inputs to postsynaptic targets at different depth in the IPL (Franke et al 2017, Greene et al 2016, Helmstaedter et al 2013). Single BC type innervate more than one RGC type, ranging from few synapses with multiple RGC types to many synapses with few RGC types (Dunn & Wong 2014). In addition to diverging, multiple BC types converge onto

individual RGC types forming synapses in stereotypic ratios and giving rise to characteristic RGC light responses (Dunn & Wong 2014, Helmstaedter et al 2013, Masland 2012a, Morgan et al 2011, Schwartz et al 2012). For example, ONα-RGCs have been shown to receive excitatory input from multiple ON cone BC types. A majority of the respective synapses is formed by B6 BCs, which contribute to the sustained ON responses of ONα-RGCs (Morgan et al 2011, Schwartz et al 2012).

Alongside BC diversity, ACs contain multiple 30-50 types in different species (Helmstaedter et al 2013, Masland 2001b). Few AC types have been studied in detail (Franke & Baden 2017, Jadzinsky & Baccus 2013, Masland 2012b). For example, AII ACs serve a bridge function between the rod pathway and RGCs in night vision, by transmitting ON signals from RBCs to several, if not all of the ON (electrical synapses) and OFF (glycinergic synapses) cone BC types (Masland 2001a). AII ACs are also operational during daytime vision: they are driven by multiple ON cone BCs via the same electrical synapses used at night, and provide ON inhibition to OFF RGCs (i.e., crossover inhibition) as well as to OFF BCs to rectify OFF pathways (Liang & Freed 2010, Oesch et al 2011). In contrast to AII ACs' multifaceted contributions to visual processing via connections with multiple BC types, starburst ACs (SACs) are specifically involved in one RGC circuit that computes the direction of image motion, the direction-selective ganglion cell circuit (DSGCs) (Franke & Baden 2017, Oesch et al 2011). The mechanisms underlying the direction selectivity of SAC-DSGC circuits include electrically isolated dendritic compartments of SACs allowing local processing, as well as asymmetrical connectivity between SACs and DSGCs (Briggman et al 2011, Euler et al 2002). Aside from AII ACs and SACs , the connectivity and function most AC types remains unknown (Franke & Baden 2017, Masland 2001a, Oesch et al 2011).

In summary, diverse cell types and cell-type-specific connectivity patterns underlie the computational prowess of the retina. At the first synapse, different BC types extract distinct temporal, chromatic, and contrast components of the shared photoreceptor input signals, giving rise to more than a dozen parallel channels from the outer to the inner retina. In the inner retina, BC signals diverge and converge, and interact with signals from diverse AC types to enable RGCs to detect specific features and events in the visual world.

1.5 Scope of Dissertation

This dissertation addresses two fundamental questions in neuroscience. (1) What mechanisms guide the emergence of specific connectivity during development? (2) What mechanisms enable mature circuits to encode specific sensory information? In the first part, I used a mouse RGC circuit to address three questions about the development of cell-type-specific connectivity patterns: (a) Is cell-type-specific connectivity hard-wired or shaped by plasticity? (b) How does homeostatic plasticity, which is known to control synapse strength and intrinsic excitability of individual neurons, act at a circuit level? (c) How does homeostatic plasticity, which is known to stabilize average firing rates, regulate specific sensory computations (Tien et al 2017)? Next, I identified one unique type of RGCs in the mouse retina— suppressed-by-contrast (SbC-) RGCs, characterized their responses, and dissected circuit mechanisms that generate their suppressive light responses (Tien et al 2016, Tien et al 2015). Finally, to gain insights into the contributions of SbC-RGCs to visual processing, I mapped SbC-RGC projections in the brain using an intersectional transgenic strategy. Examination of SbC-RGCs' innervation across development also revealed that SbC-RGCs' axon target matching is highly accurate, and does not follow the general rule that time of axon arrival correlates with the number of incorrect, transient target innervation as shown in other RGC types which have been studied so far.

Chapter 2 : Homeostatic Plasticity Shapes Cell-Type-Specific Wiring in the Retina

Convergent input from different presynaptic partners shapes the responses of postsynaptic neurons. Whether developing postsynaptic neurons establish connections with each presynaptic partner independently, or balance inputs to attain specific responses is unclear. Retinal ganglion cells (RGCs) receive convergent input from bipolar cell types with different contrast responses and temporal tuning. Here, using optogenetic activation and pharmacogenetic silencing, we found that type 6 bipolar cells (B6) dominate excitatory input to ONα-RGCs. We generated mice in which B6 cells were selectively removed from developing circuits (*B6-DTA*). In *B6-DTA* mice, ONα-RGCs adjusted connectivity with other bipolar cells in a cell-type-specific manner. They recruited new partners, increased synapses with some existing partners, and maintained constant input from others. Patch clamp recordings revealed that anatomical rewiring precisely preserved contrast- and temporal frequency response functions of ONα-RGCs, indicating that homeostatic plasticity shapes cell-type-specific wiring in the developing retina to stabilize visual information sent to the brain.

2.1 Introduction

To extract specific information, postsynaptic neurons combine input from different presynaptic cell types in precise ratios. During development, molecular interactions between pre- and postsynaptic partners set up initial connectivity patterns, which are subsequently refined (Sanes & Yamagata 2009, Williams et al 2010, Yogev & Shen 2014). Refinement occurs at many levels, from the molecular composition and the architecture of individual synapses (Turrigiano & Nelson 2004, Wefelmeyer et al 2016), the formation of new synapses and elimination of existing

ones (Morgan et al 2011, Purves & Lichtman 1980), to the large-scale organization of neuronal projections and cell numbers (Antonini & Stryker 1993, Riccomagno & Kolodkin 2015, Yu et al 2004). Remarkably, refinement balances changes across all levels to stabilize activity in emerging circuits (i.e. homeostatic plasticity). The importance of homeostatic plasticity to circuit development is underscored by recent evidence for its failures in many neurodevelopmental disorders (Ebert & Greenberg 2013, Ramocki & Zoghbi 2008, Turrigiano & Nelson 2004). Homeostatic plasticity is known to mediate interactions between pre- and postsynaptic partners that maintain constant average firing rates of neurons by controlling synaptic scaling (Davis & Muller 2015, Hengen et al 2013, Pozo & Goda 2010). Whether homeostatic plasticity also mediates interactions between different presynaptic inputs and adjusts patterns of convergent innervation (i.e. circuit-level plasticity) to stabilize specific computations of postsynaptic neurons is unknown.

In the mammalian retina, approximately 15 types of bipolar cells relay photoreceptor signals from the outer to the inner plexiform layer (IPL) (Euler et al 2014, Shekhar et al 2016). Bipolar cell types differ in their contrast responses and in their temporal filtering of photoreceptor signals (Baden et al 2013a, Borghuis et al 2013, Euler et al 2014, Franke et al 2017, Ichinose et al 2014). In the IPL, bipolar cell types converge in specific ratios onto the dendrites of 30-40 RGC types (Calkins & Sterling 2007, Dunn & Wong 2014, Helmstaedter et al 2013), which inherit the contrast responses and temporal tuning of their combined inputs (Baden et al 2016, Murphy & Rieke 2006). The relationship of bipolar cell innervation and light responses has been characterized particularly well for ONα-RGCs. Compared to other RGCs, ONα-RGCs encode contrast linearly and with high sensitivity (Murphy & Rieke 2006, Zaghloul et al 2003). Anatomical circuit reconstructions suggest that ONα-RGCs are innervated by several

bipolar cell types, with B6 cells accounting for approximately 70 % of excitatory synapses on their dendrites (Morgan et al 2011, Schwartz et al 2012). The responses of ONα-RGCs are accurately predicted by their excitatory input (Grimes et al 2014, Murphy & Rieke 2006, Zaghloul et al 2003), and a receptive field model based on B6 innervation alone captures many response features (Schwartz et al 2012). However, whether B6 cells provide functional input to ONα-RGCs has not been directly tested, and whether during development ONα-RGCs form connections with converging bipolar cells independently or balance inputs to attain specific responses is unclear.

Here, using optogenetic activation and acute pharmacogenetic silencing, we found that in wild-type mice ONα-RGC responses rely on excitatory input from B6 cells. We generated mice in which B6 cells were selectively removed from developing circuits by transgenic expression of diphtheria toxin. Anatomical circuit reconstructions and patch clamp recordings revealed that B6 cell removal elicited circuit-level plasticity in which other bipolar cell types took over innervation in specific ratios that precisely conserved contrast responses and temporal tuning of excitatory inputs and spiking of ONα-RGCs.

2.2 Materials and Methods

2.1.1 Mice

Throughout this study, we used *CCK-ires-Cre* (Taniguchi et al 2011) mice (i) crossed to a tdTomato reporter strain (*Ai9*) (Madisen et al 2010), (ii) crossed to a channelrhodopsin-2 reporter strain (*Ai32*) (Madisen et al 2012), (iii) crossed to mice in which a 9 kb fragment of the *Grm6* promoter (i.e. $Grm6_L$) (Ueda et al 1997) drives expression of YFP or, upon Cre-mediated recombination, of an attenuated version of diphtheria toxin $Grm6_L$-*YFP-DTA*^{con} (Morgan et al

2011), or (iv) injected with AAVs. For our experiments, we isolated retinas from young adult (postnatal day 20-40) mice of both sexes. All procedures were approved by the Animal Studies Committee of Washington University School of Medicine and performed in compliance with the National Institutes of Health *Guide for the Care and Use of Laboratory Animals*.

2.2.2 Adeno-associated viruses

To label ON cone bipolar and rod bipolar cells, we generated adeno-associated viruses (AAVs) in which four concatenated repeats of a 200 bp fragment of the *Grm6* promoter (*Grm6$_S$*) (Lagali et al 2008) drive expression of tdTomato, a red fluorescent protein (plasmid: *pAAV-Grm6$_S$-tdT*). The *pAAV-Grm6$_S$-PSAM^{con}* vector for pharmacogenetic silencing was derived by replacing tdTomato sequences of *pAAV-Grm6$_S$-tdT* with a *FLEX-rev-PSAM$^{L141F,\ Y115F}$-GlyR-IRES-GFP* cassette (Addgene plasmid: 32480) (Magnus et al 2011). The *pAAV-Grm6$_s$-GFP^{con}* plasmid was generated by removing PSAM-IRES sequences from *pAAV-Grm6$_S$-PSAM^{con}*. Viral particles were packaged and purified as previously described (Grimm et al 2003, Klugmann et al 2005). Briefly, AAV1/2 chimeric virions were produced by co-transfecting HEK-293 cells with *pAAV-Grm6$_S$-tdT*, *pAAV-Grm6$_S$-PSAM^{con}* or *pAAV-Grm6$_s$-GFP^{con}*, and helper plasmids encoding Rep2 and the Cap for serotype 1 and Rep2 and the Cap for serotype 2. Forty-eight hours after transfection, cells and supernatant were harvested and viral particles purified using heparin affinity columns (Sigma). Viruses (250 nL) were injected with a NanojectII (Drummond) into the vitreous chamber of newborn mice anesthetized on ice.

2.2.3 Tissue preparation

Mice were euthanized with CO_2 followed by decapitation and enucleation. For imaging, eyes were transferred into oxygenated mouse artificial cerebrospinal fluid (mACSF$_{HEPES}$) containing

(in mM): 119 NaCl, 2.5 KCl, 1 NaH_2PO_4, 2.5 $CaCl_2$, 1.3 $MgCl_2$, 20 HEPES, and 11 glucose (pH adjusted to 7.37 using NaOH). Retinas were either isolated and mounted flat on filter paper, or left in the eyecup for 30 min fixation with 4 % paraformaldehyde in $mACSF_{HEPES}$ (Tien et al 2016). For patch clamp recordings, mice were dark adapted at least 2 hr before their retinas were isolated under infrared illumination (> 900 nm) in oxygenated $mACSF_{NaHCO3}$ containing (in mM) 125 NaCl, 2.5 KCl, 1 $MgCl_2$, 1.25 NaH_2PO_4, 2 $CaCl_2$, 20 glucose, 26 $NaHCO_3$ and 0.5 L-glutamine equilibrated with 95 % O_2 / 5 % CO_2 (Tien et al 2016).

2.2.4 Immunohistochemistry

After blocking for 2 hr with 5 % Normal Donkey Serum in PBS, vibratome slices (60 µm in thickness) embedded in 4 % agarose (Sigma) were incubated overnight at 4 °C with primary antibodies. Slices were then washed in PBS (3 × 20 min) and incubated in secondary antibodies for 2 hr at room temperature. Flat-mount preparations were frozen and thawed three times after cryoprotection (1 hr 10 % sucrose in PBS at RT, 1 hr 20 % sucrose in PBS at RT, and overnight 30 % sucrose in PBS at 4 °C), blocked with 5 % Normal Donkey Serum in PBS for 2 hr, and then incubated with primary antibodies for 5 d at 4 °C and washed in PBS (3 × 1 hr) at RT. Subsequently, flat mounts were incubated with secondary antibodies for 1 d at 4 °C and washed in PBS (3 × 1 hr) at room temperature. The following primary antibodies were used in this study: mouse anti-synaptotagmin II (znp-1, 1:500, Zebrafish International Resource Center), rabbit anti-tdTomato (1:1000, Clontech Laboratories), guinea pig anti-VGluT1 (1:500, Millipore), chicken anti-GFP (1:500, thermos Fisher Scientific) and mouse anti-CtBP2 (1:500, BD Biosciences). Secondary antibodies were Alexa 568- and Alexa 633 conjugates (1:1000, Invitrogen).

2.2.5 Electrophysiology

Cell-attached and whole-cell patch clamp recordings were obtained in the dorsal halves (Wang et al 2011) of dark-adapted flat-mounted retinas superfused (5-7 mL / min) with warm (30-33 °C) $mACSF_{NaHCO3}$ as previously described (Tien et al 2016). ONα-RGCs were selected under infrared illumination based on their large soma size (diameter > 20 μm); and correct targeting was confirmed by inclusion of Alexa 488 or Alexa 568 (0.1 mM) in the intracellular solution and 2-photon imaging at the end of each recording. The intracellular solution for current-clamp recordings contained (in mM) 125 K-gluconate, 10 NaCl, 1 $MgCl_2$, 10 EGTA, 5 HEPES, 5 ATP-Na_2, and 0.1 GTP-Na (pH adjusted to 7.2 with KOH). The intracellular solution voltage-clamp recordings contained (in mM) 120 Cs-gluconate, 1 $CaCl_2$, 1 $MgCl_2$, 10 Na-HEPES, 11 EGTA, 10 TEA-Cl, 2 Qx314, ATP-Na_2, and 0.1 GTP-Na (pH adjusted to 7.2 with CsOH). Patch pipettes had resistances of 3-6 MΩ (borosilicate glass). Liquid junction potentials were corrected off-line. Signals were amplified with a Multiclamp 700B amplifier (Molecular Devices), filtered at 3 kHz (8-pole Bessel low-pass), and sampled at 10 kHz (Digidata 1440A, Molecular Devices). Excitatory postsynaptic currents (EPSCs) were measured at the reversal potential of inhibitory (-60 mV) conductances. For optogenetic experiments, the following reagents were applied individually or in combinations: L-AP4 (20 μM, Tocris), ACET (10 μM, Tocris), HEX (300 μM, Tocris), D-AP5 (30 μM, Tocris) and NBQX (40 μM, Tocris). For pharmacogenetic silencing, $PSEM^{308}$ (20 μM, Apex Scientific Inc.) was bath-applied for at least 15 min. Meclofenamic acid (MFA, 200 μM, Sigma) was used to block gap junctions. To isolate the spontaneous excitatory synaptic currents (sEPSCs), the tissue was bathed in $mACSF_{NaHCO3}$ with zero calcium concentration to block neurotransmission. In puff experiments, glutamate (1 mM in $mACSF_{NaHCO3}$, Sigma) was focally applied near the primary dendrites of ONα-RGCs by

delivering pressure (5 psi) to a patch pipette via a Picospritzer II (Parker Hannifin). Alexa 488 (0.1 mM) was included in the puff solution to estimate the application area under two-photon imaging (Akrouh & Kerschensteiner 2013). Two to three primary dendrites were tested per cell, and five to six puffs of glutamate of various durations (5-100 ms) were applied to the same location.

2.2.6 Light stimulation

For optogenetic experiments, light from a mercury bulb (Olympus) was band-pass filtered (426-446 nm, Chroma) and focused onto RGC side of the retina (intensity: 3.15×10^{-4} W / mm^2) through a 20 × 0.95 NA water immersion objective. Stimulus timing was controlled by a Uniblitz shutter (Vincent Associates). To probe photoreceptor-mediated light responses, stimuli were written in MATLAB (The MathWorks), presented on an organic light-emitting display (eMagin; refresh rate, 60 Hz) using Cogent graphics extensions (John Romaya, University College London, London, UK), and focused onto the photoreceptor side of the retina via a substage condenser. Stimuli were centered on the soma of the recorded cell with mean intensity of either 1.5 or 1500 rhodopsin isomerization / rod / s (R*). To test contrast sensitivity, short luminance steps (250 ms) were presented every 2.25s in a circular area (diameter: 300 µm). To probe spatiotemporal tuning, the stimulus display was divided into vertical bars (width: 50 µm, height: 600 µm), and the intensity of each bar randomly updated from a Gaussian distribution every 33 ms (refresh rate: 30 Hz) for 15 min.

2.2.7 Biolistic transfection

Gold particles (1.6 µm diameter, Bio-Rad) were coated with plasmids encoding cytosolic tdTomato or YFP under the cytomegalovirus promoter, and postsynaptic density protein 95

(PSD95) fused at its C terminus to CFP (Morgan et al 2011). We used a helium-pressurized gun (40 psi, Bio-Rad) to deliver particles to RGCs and incubated the transfected retinas into $mACSF_{HEPES}$ in a humid oxygenated chamber at 33 °C for 16-18 hr.

2.2.8 Imaging

Images were acquired on an Fv1000 confocal microscope (Olympus) using a 20 × 0.85 NA or 60 × 1.35 NA oil immersion objective. Image stacks of ONα-RGC dendrites and synapse patterns were acquired at a voxel size 0.103-0.3 µm (x/y-z axis). Bipolar cell image stacks were acquired at a voxel size range of 0.11, 0.082 or 0.066 µm-0.3 µm (x/y-z axis). Bipolar cell types were identified by their characteristic axonal and dendritic morphology (Dunn & Wong 2012, Helmstaedter et al 2013, Kerschensteiner et al 2009, Morgan et al 2011).

2.2.9 Electrophysiology analysis

For contrast steps as well as optogenetic stimulation, baseline-subtracted averaged responses (spike rate or conductance) were measured during 100-200 ms time windows. Temporal response profiles were calculated by reverse correlation of the stimulus with the response and averaged for stimulus bars overlaying the receptive field center (i.e. response-weighted stimulus averages) (Kim et al 2015). Frequency tuning was then computed by Fourier transforms of the temporal response profiles. All analyses above were performed using custom scripts written in MATLAB. Area and amplitude thresholds (Mini Analysis, Synaptosoft) were optimized to detect sEPSC events in each recording (Kerschensteiner et al 2009). sEPSCs traces presented in the figures were additionally low-pass filtered at 2 kHz for display. For puff experiments, baseline-subtracted averaged responses (conductance) were normalized by the application area measured by 2-photon imaging of the Alexa 488 included in the puff solution.

2.2.10 Imaging Analysis

ONα-RGC dendrites and synapse patterns were reconstructed from image stacks using local thresholding in Amira (FEI Imaging) and previously described custom software written in MATLAB (Kerschensteiner et al 2009, Morgan et al 2008). For the stratification calculation, dendrites were skeletonized into segments of ~0.5 µm length. For each segment, the distance of its z-position to the median z-position of all segments within a 30-µm radius was computed, and this measure averaged across all segments of a cell to quantify its stratification. Use of a 30-µm radius prevents broader distortions of the tissue from influencing measurements of stratification. Dendritic skeletonization and stratification analysis was performed using custom scripts written in MATLAB (Morgan et al 2011). Colocalization of PSD95 puncta and CtBP2 puncta was assessed visually in Fiji (Schindelin et al 2012). The connectivity of pairs of bipolar cells and ONα-RGCs was analyzed in image stacks as previously described (Morgan et al 2011). Briefly, dendrites of ONα-RGCs and axons of bipolar cells were masked in 3D using local thresholding in Amira. Contacts were defined as points of overlap between axon and dendrite masks exceeding 50 connected voxels; and synapses counted when PSD95 puncta were found within such a volume of axon-dendrite overlap. Bipolar cell axon territories were measured by the area of the smallest convex polygons encompassing their arbors in a maximum intensity projection.

2.2.11 Statistics

Paired and unpaired t-tests were used to assess the statistical significance of differences between single parameter characteristics (e.g. dendrite length) of experimental groups. Cumulative probabilities of sEPSCs amplitudes, Contrast- and temporal frequency response functions of *B6-DTA* mice and wild-type littermates (or before, during and after PSEM^{308} application) were compared using bootstrapping with 10,000 replicates. Differences in the average response curves

of *B6-DTA* and wild-type mice were compared to differences generated by random assignments of data to the two genotypes (confidence interval: 95 %). For all figures significance corresponds to *p < 0.05, **p < 0.01, ***p < 0.001, ****p < 0.0001 for the comparisons indicated in the figure or figure legend.

2.3 Result

2.3.1 B6 cells provide dominant excitatory input to ONα-RGCs

ONα-RGCs receive convergent input from several bipolar cell types (Figure 2.1A). Although anatomical studies suggested that B6 cells account for approximately 70 % of excitatory synapses on ONα-RGC dendrites (Morgan et al 2011, Schwartz et al 2012), the functional input from B6 cells to ONα-RGCs has not yet been explored. To gain genetic access to B6 cells, we screened a set of Cre driver lines (Taniguchi et al 2011) by crossing to a fluorescent reporter strain (*Ai9*, tdTomato) (Madisen et al 2010). In *CCK-ires-Cre Ai9* mice, which were previously shown to label several RGC and amacrine cell types (Tien et al 2015, Zhu et al 2014), tdTomato expression in the bipolar cell layer was restricted to a single cell type. The somata of these cells were arranged in a mosaic (Figures 2.1B and 2.2); their axon terminals stratified in the ON sublamina of the IPL and stained for synaptotagmin II (SytII) (Figure 2.1C) (Fox & Sanes 2007). This identifies the bipolar cells labeled in *Cck-ires-Cre Ai9* mice as B6 cells, consistent with a recent gene expression profiling study, which revealed Cck as a specific marker of B6 cells (Shekhar et al 2016).

To test for functional connectivity of B6 cells with ONα-RGCs, we crossed *Cck-ires-Cre* mice to a strain in which channelrhodopsin-2 is expressed wherever Cre-mediated recombination occurs (*Ai32*) (Madisen et al 2012). With photoreceptor input to bipolar cells blocked by

application of L-AP4 and ACET, and cholinergic transmission blocked by inclusion of hexamethonium, optogenetic stimulation of B6 cells elicited large excitatory postsynaptic currents (EPSCs) in ONα-RGCs (Figure 2.1D and 2.1E). These currents were sensitive to AMPA and NMDA receptor antagonists, demonstrating that B6 cells provide glutamatergic input to ONα-RGCs.

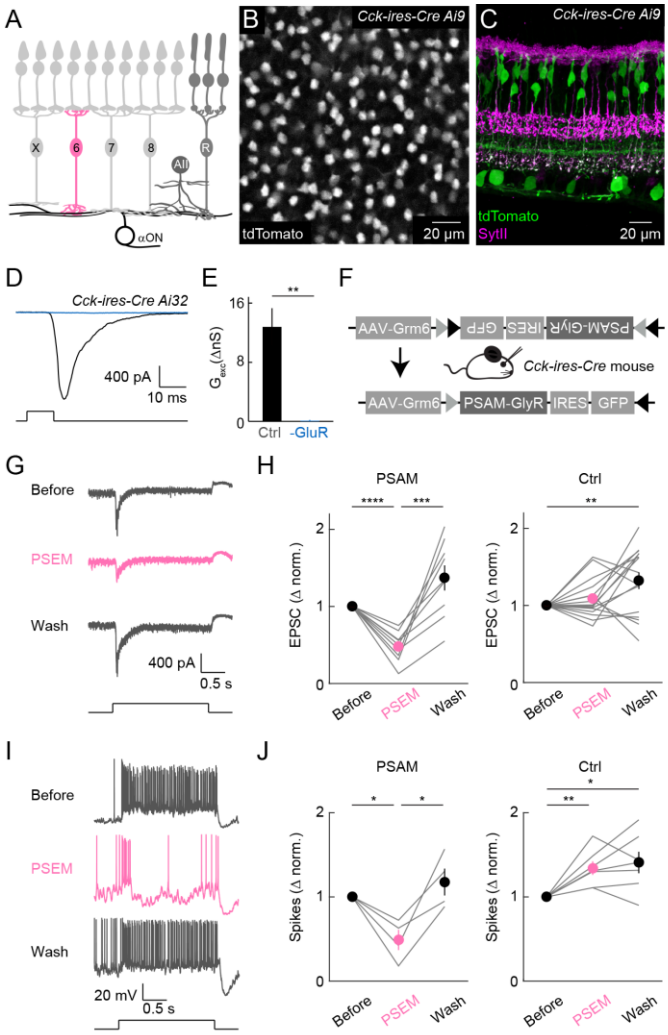

Figure 2.1 B6 cells provide dominant excitatory input to ONα-RGCs

(A) Schematic illustrating converging bipolar cell input to ONα-RGCs. *X*, *6*, *7*, and *8* refer to cone bipolar cell types (Euler et al 2014), whereas *R* indicates rod bipolar cells, which in wild-type mice provide mostly indirect input via AII amacrine cells (*AII*) and cone bipolar cells to ONα-RGCs. (B) Distribution of tdTomato-expressing cells in the inner nuclear layer of a P21 whole-mount *Cck-ires-Cre Ai9* retina. (C) Vibratome section of a P21*Cck-ires-Cre Ai9* retina showing tdTomato expression in some amacrine cells,

RGCs, and B6 cells. The latter is confirmed by immunostaining of synaptotagmin II (*SytII*), an axonal marker of B2 and B6 cells. (D and E) Representative EPSC traces (D) and summary data of excitatory conductances (E) of ONα-RGCs elicited by optogenetic stimulation of B6 cells in the absence (*black*) or presence (*blue*) of AMPA and NMDA receptor antagonists (*Ctrl*: 12.81 ± 2.54 nS, -*GluR*: : 0.08 ± 0.11 nS, n = 8, p = 0.002). L-AP4, ACET and hexamethonium were included in the bath all the time. (F) Schematic of the AAV virus injected for pharmacogenetic silencing experiments. (G and I) Representative EPSC traces (G) and spike responses (I) of ONα-RGCs in *AAV-Grm6$_S$-PSAM^{con}* injected retinas before (*Before*), during (*PSEM*) and after (*Wash*) the addition of PSEM^{308}. (H and J) Summary data of excitatory conductances (H) and spike responses (J) of ONα-RGCs with (*PSAM*) or without (*Ctrl*) *AAV-Grm6$_S$-PSAM^{con}* injection before (*Before*), during (*PSEM*) and after (*Wash*) the addition of PSEM^{308}. *Circles* (*error bar*) indicate mean (±SEM) of respective population. In (H), PSAM: *PSEM* 0.479 ± 0.064 (mean ± SEM); *Wash* 1.370 ± 0.163; *Before* vs *PSEM* p = 4 *10^{-5}; *PSEM* vs *Wash* p = 5 *10^{-4}; *Before* vs *Wash* p = 0.053. In (H), Control: *PSEM* 1.088 ± 0.064; *Wash* 1.321 ± 0.108; *Before* vs *PSEM* p = 0.19; *PSEM* vs *Wash* p = 0.068; *Before* vs *Wash* p = 0.009. In (J), PSAM: *PSEM* 0.489 ± 0.121; *Wash* 1.177 ± 0.160; *Before* vs *PSEM* p = 0.02; *PSEM* vs *Wash* p = 0.03; *Before* vs *Wash* p = 0.349. In (J), Control: *PSEM* 1.343 ± 0.081; *Wash* 1.409 ± 0.127; *Before* vs *PSEM* p = 0.006; *PSEM* vs *Wash* p = 0.53; *Before* vs *Wash* p = 0.02.

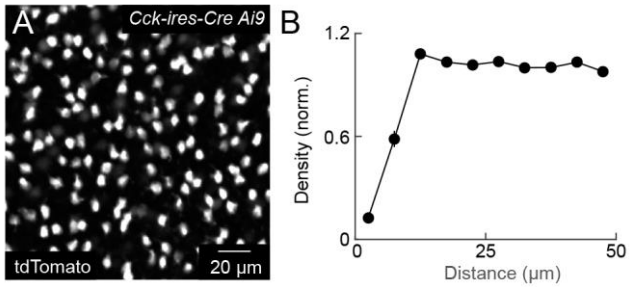

Figure 2.2 Distribution of tdTomato-expressing bipolar cells in *Cck-ires-Cre Ai9*

(A) Representative confocal image of tdTomato-expressing cells in the bipolar cell body layer of a P21 whole-mount *Cck-ires-Cre Ai9* retina. (B) Summary data of the density recovery profiles of tdTomato-expressing cells in the bipolar cell body layer (n = 5 retinas) show an exclusion zone characteristic of labeling of a single cell type.

To probe the contributions of B6 input to photoreceptor-mediated light responses of ONα-RGCs, we generated adeno-associated viruses (AAVs) that drive expression of the pharmacogenetic silencer PSAM$^{L141F,\ Y115F}$-GlyR-IRES-GFP (Magnus et al 2011), PSAM for short, from promoter elements of the metabotropic glutamate receptor 6 (*Grm6$_S$*) (Lagali et al 2008), conditioned upon Cre-mediated recombination (*AAV-Grm6$_S$-PSAM^{con}*, Figure 2.1F). Because *Grm6$_S$* sequences promote transcription only in ON bipolar cells (Lagali et al 2008),

their intersection with *CCK-ires-Cre* should restrict expression to B6 cells. We generated *AAV-Grm6$_S$-GFP^{con}* by removing PSAM-IRES sequences from *AAV-Grm6$_S$-PSAM^{con}*, to improve visualization of GFP. After injection of *AAV-Grm6$_S$-GFP^{con}* intravitreally in *CCK-IRES-Cre Ai9* mice, GFP expression was restricted to the bipolar cell layer, and nearly all GFP-positive cells (99%) were also tdTomato positive (Figure 2.3). This confirmed the cell-type-specificity of our intersectional strategy. Next, we injected *AAV-Grm6$_S$-PSAM^{con}* in *CCK-ires-Cre* mice. In retinas of these mice, application of the exogenous ligand PSEM^{308} greatly reduced light-evoked EPSCs (Figures 2.1G and 2.1H) and spike responses of ONα-RGCs (Figures 2.1I and 2.1J). By contrast, without *AAV-Grm6$_S$-PSAM^{con}* injections, PSEM^{308} had no significant effect on EPSCs of ONα-RGCs (Figure 2.1H) and slightly enhanced their spike responses (Figure 2.1J). EPSCs and firing rates of ONα-RGCs were increased upon washout of PSEM^{308} irrespective of PSAM expression, likely due to off-target effects of the agonist. (Figures 2.1H and 2.1J). Given that AAVs infected only a subset of B6 cells (Figure 2.3), the strong pharmacogenetic suppression of EPSCs, together with previous anatomical studies (Morgan et al 2011, Schwartz et al 2012) and results from optogenetics, suggests that B6 cells dominate excitatory input to and are required for normal light responses of ONα-RGCs.

We next measured excitatory input to ONα-RGCs during brief (250 ms) steps of varying contrast in a 300-μm diameter spot centered on the recorded cell. In addition to reducing the amplitude of tonic and stimulus-evoked EPSCs, application of PSEM^{308} in *AAV-Grm6$_S$-PSAM^{con}*-injected mice, resulted in less inwardly rectified excitatory contrast response functions (Figure 2.3), indicating that the functional properties of B6 input differ from those of non-B6 inputs to ONα-RGCs.

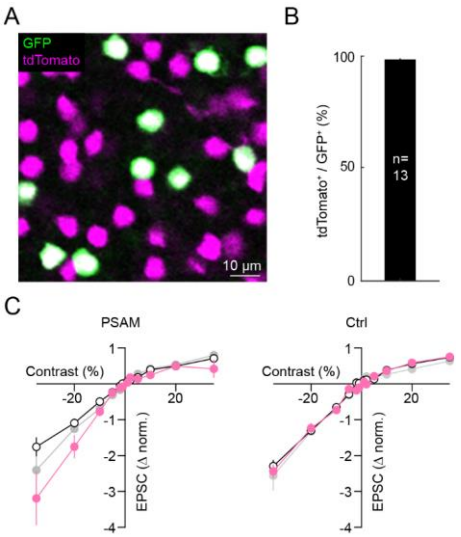

Figure 2.3 Pharmacogenetic silencing of B6 cells changes contrast response functions of ONα-RGCs

(A) Representative image of the INL in a *CCK-ires-Cre Ai9* mouse injected with *AAV-Grm6$_s$-GFP*. (B) 98.5% ± 0.5 of GFP-positive cells in the INL were also tdTomato positive. (C) Contrast response functions of the normalized excitation of ONα-RGCs with (*PSAM*, n = 10) or without (*Ctrl*, n = 9) *AAV-Grm6$_s$-PSAM^{con}* injection before (*Before, black*), during (*PSEM, pink*) and after (*Wash, grey*) the addition of PSEM^{308}. Differences between responses before and during PSEM^{308} application in the *AAV-Grm6$_s$-PSAM^{con}* injected retinas were significantly different (95% confidence interval, see Method).

2.3.2 An intersectional transgenic strategy to remove B6 cells from the developing retina

To probe interactions of converging bipolar cell types during ONα-RGC innervation, we next wanted to remove selectively B6 cells from the developing retina. We devised an intersectional strategy similar to that used for pharmacogenetic silencing of B6 cells (Figure 2.1F), and crossed mice that conditionally express an attenuated version of diphtheria toxin in ON bipolar cells (*Grm6$_L$-YFP-DTA^{con}*, Figure 2.4A) (Morgan et al 2011) to *CCK-ires-Cre* mice. We refer to double transgenic offspring from these crosses as *B6-DTA* mice from here on. To estimate the time course of DTA expression in these mice, we first counted tdTomato-expressing bipolar cells in *CCK-ires-Cre Ai9* mice at different ages. The number of these cells increased dramatically from postnatal day 10 (P10) to P15 (Figure 2.4B). Because *Ai9* can express tdTomato in the

retina at least from birth on (*data not shown*), this time course likely reflects the rise of Cre in B6 cells. By comparison, yellow fluorescent protein (YFP) in *Grm6$_L$-YFP-DTA^{con}* and other fluorescent proteins in other *Grm6$_L$* transgenics become detectable between P3 and P7 (Kerschensteiner et al 2009, Morgan et al 2006, Morgan et al 2011). Thus, the onset of DTA expression in *B6-DTA* mice appears to be limited by Cre expression and falls between P10 and P15.

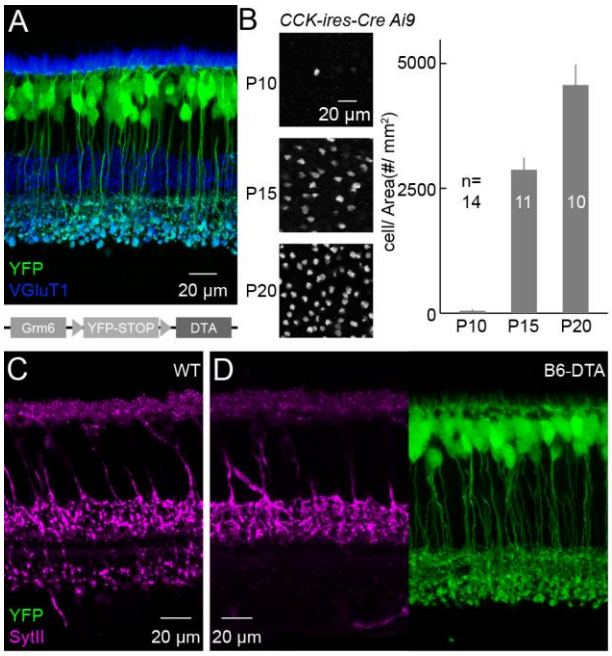

Figure 2.4 An intersectional strategy to remove B6 cells from the developing retina

(A) Representative image of a retinal section showing YFP expression in a *Grm6$_L$-YFP-DTA^{con}* mouse retina without Cre-recombination. Schematic at the *bottom* illustrates the genetic construct used to generate *Grm6$_L$-YFP-DTA^{con}* mice. (B) Representative images (*left*) and summary data (*right*) for the timecourse of tdTomato expression in *CCK-ires-Cre Ai9* mice. P10: 48.5 ± 30.5 # / mm^2 (mean ± SEM); P15: 2872.2 ± 245.6 # / mm^2; P20: 4569.3 ± 411.9 # / mm^2. (C and D) Vertical sections of wild-type (C) and *B6-DTA* (D) retinas stained for SytII and, in (D), YFP. SytII and YFP signals from the same section are shown side by side in (D).

To evaluate the extent and specificity of B6 cell removal in *B6-DTA* mice, we stained sections and flat mounts of P20 retinas for SytII. In wild-type retinas, SytII labeled B2 and B6 axons in the ON and OFF sublamina of the IPL, respectively. In *B6-DTA* mice, SytII staining in

the ON sublamina was lost, but staining in the OFF sublamina was unchanged (Figures 2.4C and 2.4D). In addition, YFP expression in non-B6 ON bipolar cell types was unaffected in *B6-DTA* mice. We quantified these observations in retinal flat mounts (Figure 2.5), confirming that >95 % of B6 cells are removed from *B6-DTA* retinas by P21. Moreover, the reduction in the density of all ON bipolar cells in *B6-DTA* mice matched the density of B6 cells in wild-type mice (Figures 2.4B and 2.5F). Approximately half of the B6 cells in *B6-DTA* retinas were deleted by P15 (Figure 2.5), indicating that the time course of cell removal closely matched that of Cre expression. Together, these results show that B6 cells are removed selectively and nearly completely from *B6-DTA* retinas during the period of bipolar cell-RGC synaptogenesis (Fisher 1979, Morgan et al 2008, Morgan et al 2011).

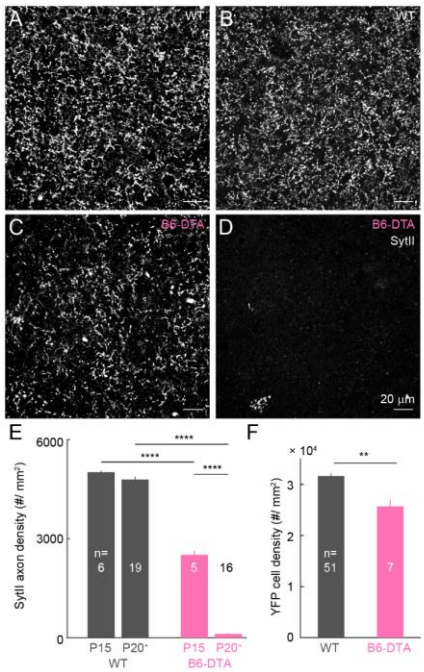

Figure 2.5 Cell-type-specific removal of B6 cells in *B6-DTA* mice

(A-D) Representative images of SytII staining in the ON sublamina of the inner plexiform layer in P15 (A), $P20^{+}$ (i.e. P20 – P30) (B) wild-type and P15 (C) and $P20^{+}$ (D) *B6-DTA* retinas. (E) Summary data of the density of SytII-positive axons in the ON sublamina in wild-type and *B6-DTA* retinas during development. In (E), *P15 WT*: 5015 ± 50 # / mm^2; *$P20^{+}$ WT*: 4792 ± 89 # / mm^2; *P15 B6-DTA*: 2511 ± 124 # / mm^2; *$P20^{+}$ B6-DTA*: 115 ± 40 # / mm^2; *P15 WT* vs *$P20^{+}$ WT* p = 0.48; *P15 WT* vs *P15 B6-DTA*

$p = 5 * 10^{-6}$; *P20*$^{+}$ *WT* vs *P20*$^{+}$ *B6-DTA* $p = 8 * 10^{-26}$; *P15 B6-DTA* vs *P20*$^{+}$ *B6-DTA* $p = 10^{-5}$. (D) Summary data of the density YFP-expressing cells in wild-type (31624 ± 548 # / mm^2) and *B6-DTA* (25699 ± 1269 # / mm^2, p = 0.002) retinas.

2.3.3 Effects of B6 cell removal on ONα-RGC dendrites and synapses

To begin to analyze effects of B6 cell removal on ONα-RGCs, we biolistically labeled these cells with cytosolic tdTomato and postsynaptic density protein 95 fused to YFP (PSD95-YFP), a marker of excitatory synapses (Kerschensteiner et al 2009, Morgan et al 2011). We found that stratification and length of ONα-RGC dendrites were indistinguishable between *B6-DTA* mice and wild-type littermates (Figures 2.6A-2.6D). The density of PSD95-YFP puncta on ONα-RGC dendrites was reduced in *B6-DTA* mice (Figure 2.6E), but only by 30 %, much less than the fraction of synapses (70 %) contributed by B6 cells in wild-type mice (Morgan et al 2011, Schwartz et al 2012). This suggests that either many PSD95-YFP puncta in *B6-DTA* mice are not apposed by presynaptic release sites (i.e. orphan postsynapses), or that other bipolar cells take over ONα-RGC innervation from B6 cells. To distinguish between these possibilities, we stained retinas with biolistically labeled ONα-RGCs for CtBP2, a component of presynaptic ribbons in bipolar cells (Schmitz et al 2000) (Figure 2.6F). An identical fraction (85 %) of PSD95-YFP puncta on ONα-RGC dendrites colocalized with CtBP2 in *B6-DTA* mice and wild-type littermates (Figure 2.6G), indicating that in the absence of B6 cells other bipolar cells increase their connectivity with ONα-RGCs.

2.3.4 Cell-type-specific rewiring of cone bipolar cells with ONα-RGCs in *B6-DTA* mice

Dendrites of ONα-RGCs overlap with axons of several ON cone bipolar cells types (B6, B7, B8, and XBC) (Dunn & Wong 2014, Helmstaedter et al 2013, Morgan et al 2011). We wanted to test

which of these replace input from B6 cells in *B6-DTA* mice, and whether rewiring occurs by uniform upregulation of connectivity or is cell type specific. We sparsely labeled ON bipolar cells by intravitreal injection of a virus expressing tdTomato under control of $Grm6_S$ (*AAV-$Grm6_S$-tdTomato*, Figure 2.7A), and biolistically labeled ONα-RGCs and bipolar cell-RGC synapses with cytosolic YFP and PSD95-CFP, respectively. This allowed us to analyze the connectivity of pairs of individual bipolar cells and ONα-RGCs.

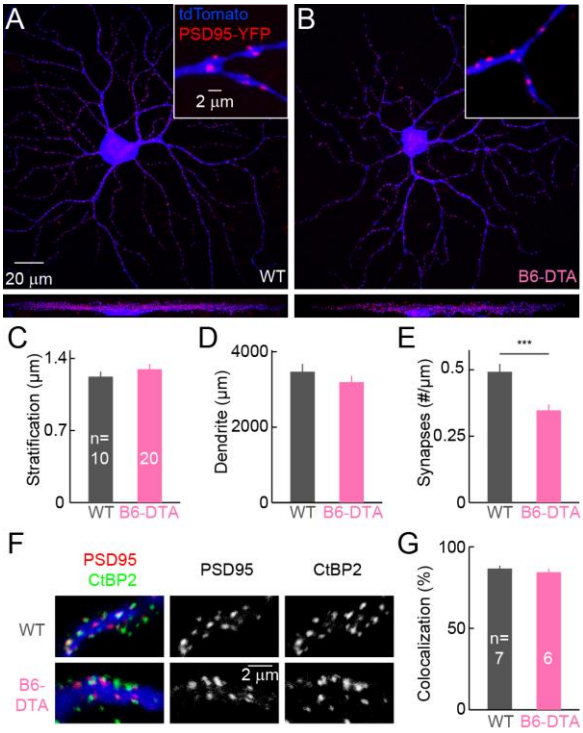

Figure 2.6 Effects of B6 cell removal on ONα-RGC dendrites and synapses

(A and B) Top-down (*top*) and side (*bottom*) views of ONα-RGCs biolistically labeled with cytosolic tdTomato and PSD95-YFP in wild-type (A) and *B6-DTA* (B) retinas. *Insets* show enlarged views of PSD95-YFP puncta along ONα-RGCs dendrites. (C-E) Summary data (mean ± SEM) of dendritic parameters of ONα-RGCs in wild-type (*grey*) and *B6-DTA* (*pink*) mice. In (C), *WT*: 1.22 ± 0.05 µm; *B6-DTA*: 1.29 ± 0.05 µm; $p = 0.17$. In (D), *WT*: 3471 ± 206 µm; *B6-DTA*: 3195 ± 166 µm; $p = 0.31$. In (E), *WT*: 0.492 ± 0.03 synapses / µm; *B6-DTA*: 0.347 ± 0.02 synapses / µm; $p < 0.001$. (F and G) Representative images (F) and summary data (G) showing the colocalization of PSD95-YFP puncta with CtBP2 in wild-type (*top row*) and *B6-DTA* (*bottom row*) ONα-RGCs. In (G), WT: 86.7 ± 1.9 %; B6-DTA: 84.4 ± 2.2 %; $p = 0.44$.

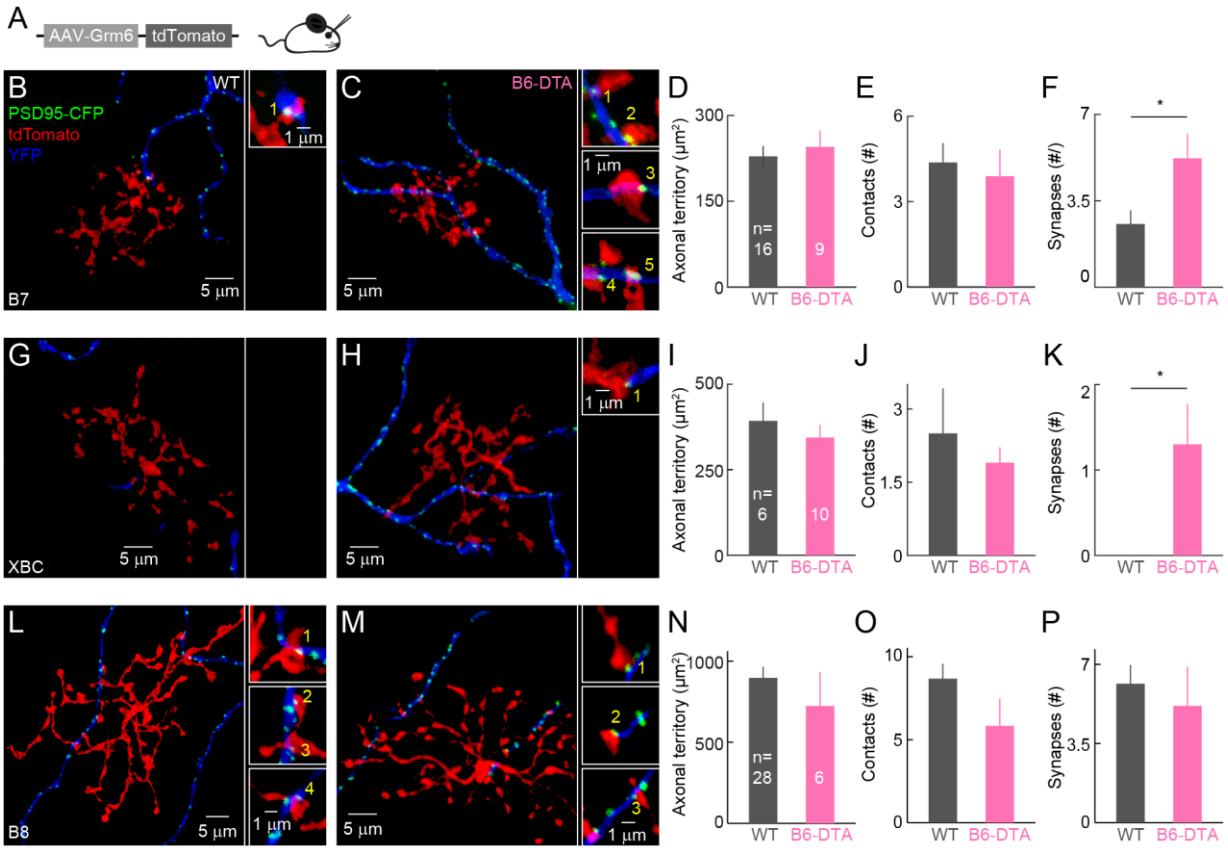

Figure 2.7 Cell-type-specific rewiring of cone bipolar cells with ONα-RGCs following B6 cell removal

(A) Schematic of *AAV-Grm6*$_S$*-tdTomato* injection to sparsely label ON bipolar cells. (B and C) Examples of isolated B7 – ONα-RGC pairs in wild-type (B) and *B6-DTA* (C) retinas. Maximum intensity projections of confocal image stacks are shown on the *left*. The panels on the *right* show single planes from the image stacks at contact points between B7 cell axons (*red*) and ONα-RGC dendrites (*blue*). Synapses were identified by PSD95 puncta (*green*). (D-F) Summary data for axon territories (D), axo-dendritic contacts (E) and synapse numbers (F) for B7 – ONα-RGC pairs in wild-type (*grey*) and *B6-DTA* (*pink*) retinas. In (D), *WT*: 229 ± 18 µm^2 (mean ± SEM); *B6-DTA*: 245 ± 28 µm^2; p = 0.63. In (E), *WT*: 4.38 ± 0.68; *B6-DTA*: 3.89 ± 0.93; p = 0.68. In (F), *WT*: 2.56 ± 0.56; *B6-DTA*: 5.22 ± 0.98; p < 0.05. (G-K) Analogous to B and C (G and H) and D-F (I-K) but for XBC – ONα-RGC pairs. In (I), *WT*: 393 ± 54 µm^2; *B6-DTA*: 344 ± 38 µm^2; p = 0.47. In (J), *WT*: 2.50 ± 0.92; *B6-DTA*: 1.90 ± 0.31; p = 0.56. In (K), *WT*: 0.00 ± 0.00; *B6-DTA*: 1.30 ± 0.47; p = 0.02. (L-P) Analogous to B and C (L and M) and D-F (N-P) but for B8 – ONα-RGC pairs. In (N), *WT*: 897 ± 210 µm^2; *B6-DTA*: 724 ± 210 µm^2; p = 0.47. In (O), *WT*: 8.68 ± 0.9; *B6- DTA*: 5.83 ± 1.66; p = 0.17. In (P), *WT*: 6.14 ± 0.84; *B6-DTA*: 5.17 ± 1.74; p = 0.63.

We distinguished bipolar cell types by their characteristic dendritic and axonal morphologies (Dunn & Wong 2012, Helmstaedter et al 2013, Morgan et al 2011, Wassle et al 2009). B7 cells were previously characterized as a minor input to ONα-RGCs (Morgan et al

2011, Schwartz et al 2012). We confirmed these observations in wild-type mice and found that in *B6-DTA* retinas, B7 cells more than doubled the number of connections with ONα-RGCs (Figures 2.7B, 2.7C, 2.7F). This was accomplished without changes in the axon territories of B7 cells (Figure 2.7D) or the number of contacts between B7 axons and ONα-RGC dendrites (Figure 2.7E), by conversion of a larger fraction of contacts to synapses (i.e. connectivity fraction). In wild-type mice, axons of XBC cells occasionally touched dendrites of ONα-RGCs, but none of these contacts bore synapses (Figures 2.7G, 2.7J, 2.7K). In *B6-DTA* mice, XBC axon size and contact numbers with ONα-RGCs did not change, but nearly all contacts contained synapses (Figures 2.7H-2.7K). However, bipolar cell connectivity was not uniformly upregulated in *B6-DTA* mice, as the large axons of B8 cells, which formed a significant number of synapses with ONα-RGCs in wild-type mice, were unchanged in their morphology and connectivity (Figures 2.7L-2.7P). Thus, B6 cell removal from developing circuits triggers cell-type-specific rewiring of cone bipolar cells with ONα-RGCs, which elevates a minor input to become the major one (B7), recruits a novel input type (XBC), and leaves unaltered the connections of another (B8). Rewiring is accomplished by selective changes in the connectivity fraction of bipolar cell axons without changes to their morphology or the frequency of contacts between bipolar cell axons and ONα-RGC dendrites.

2.3.5 Increased direct input from rod bipolar cells to ONα-RGCs in *B6-DTA* mice

In wild-type mice, rod bipolar cells (RBCs) provide input to ONα-RGCs - and other RGCs - predominantly by an indirect path: RBC axons form excitatory synapses with AII amacrine cells, which are electrically coupled to ON cone bipolar cells, which convey signals to ONα-RGCs

(Bloomfield & Dacheux 2001, Demb & Singer 2015). During development, RBCs initially form synapses with ONα-RGC dendrites, but subsequently eliminate most of their connections as B6 cells increase connectivity with ONα-RGCs (Morgan et al 2011). We wondered whether RBCs retain synapses with ONα-RGCs in *B6-DTA* mice, in which B6 cells are removed during development. We sparsely labeled RBCs by *AAV-Grm6$_S$-tdTomato* injections, and ONα-RGCs and excitatory synapses by biolistics. Similar to our observations for cone bipolar cells, we found that axon territories and the number of contacts with ONα-RGC dendrites did not change for RBCs in *B6-DTA* mice (Figures 2.8A-2.8D). However, the probability of synaptic connections more than doubled (Figure 2.8E), suggesting that RBCs retain synapses with ONα-RGCs when B6 cells are removed.

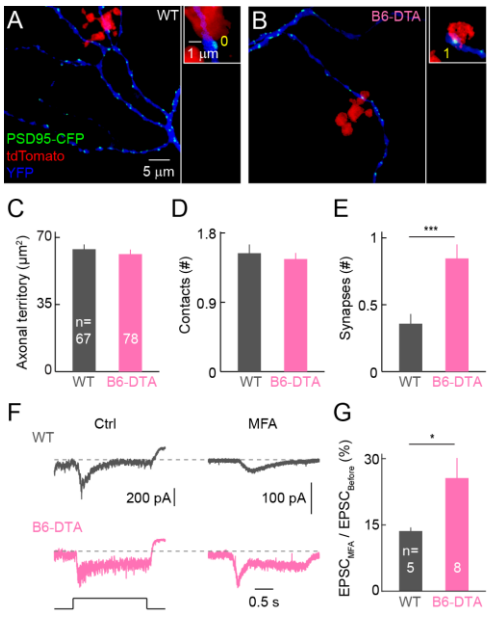

Figure 2.8 Increase in connectivity between rod bipolar cells and ONα-RGCs in *B6-DTA* mice

(A and B) Examples of isolated RBC – ONα-RGC pairs in wild-type (A) and *B6-DTA* (B) retinas. Maximum intensity projections of confocal image stacks are shown on the *left*. The panels on the *right* show single planes from the image stacks at contact points between RBC axons (*red*) and ONα-RGC dendrites (*blue*). (C-E) Summary data of axon territories (C), axo-dendritic contacts (D), and synapses (E)

for RBC – ONα-RGC pairs in wild-type (*grey*) and *B6-DTA* (*pink*) retinas. In (C) *WT*: 63.9 ± 2.5 μm^2; *B6-DTA*: 61.30 ± 2.36 μm^2; p = 0.46. In (D), *WT*: 1.54 ± 0.11; *B6-DTA*: 1.46 ± 0.08; p = 0.58. In (E), *WT*: 0.36 ± 0.07; *B6-DTA*: 0.85 ± 0.11; $p = 2 * 10^{-4}$. (F and G) Representative EPSC traces (F) and summary data (G) of ONα-RGC responses to dim light steps (3 rhodopsin isomerizations / rod /s or R*) in the absence (*left, Ctrl*) or presence (*right, MFA*) of MFA. In (G) *WT*: 13.6 ± 0.8 %; *B6-DTA*: 25.6 ± 4.5 %; p = 0.03.

Indirect input from RBCs to ONα-RGCs depends on gap junctions between AII amacrine cells and ON cone bipolar cells, whereas direct synaptic input does not. In patch clamp recordings from ONα-RGCs, we found that a larger fraction of excitatory input elicited by stimuli that predominantly recruit the RBC pathway (Murphy & Rieke 2006) was resistant to the gap junction blocker meclofenamic acid (MFA) in *B6-DTA* mice compared to wild-type littermates (Figures 2.8F and 2.8G). This shows that anatomical rewiring mediates changes in functional connectivity in *B6-DTA* mice, which involve both cone and rod bipolar cells.

2.3.6 Bipolar cell rewiring precisely preserved light responses of ONα-RGCs in *B6-DTA* mice.

Our pairwise analysis revealed cell-type-specific changes in the connectivity of bipolar cells with ONα-RGCs in *B6-DTA* mice (Figures 2.7 and 2.8). We hypothesized that ONα-RGCs recruit bipolar cell types in specific ratios (Figure 2.9) (see Methods) to best replace the input from B6 cells and to preserve their characteristic light responses. To test this hypothesis, we analyzed light responses of ONα-RGCs using patch clamp recordings. In stark contrast to acute pharmacogenetic silencing of B6 cells (Figures 2.1G-2.1J), the amplitudes of excitatory inputs and spike responses of ONα-RGCs were not significantly different between *B6-DTA* mice and wild-type littermates (Figures 2.10A-2.10H). This was true both for stimuli preferentially activating rods (Figures 2.10A, 2.10B, 2.10D, and 2.10E) and for stimuli preferentially activating cones (Figures 2.10G, 2.10H, 2.10J and 2.10K). Moreover, the characteristic contrast response

functions of ONα-RGC EPSCs and spiking (Murphy & Rieke 2006, Zaghloul et al 2003), were precisely preserved in *B6-DTA* mice in dim (Figures 2.10C and 2.10F) and bright light conditions (Figures 2.10I and 2.10L).

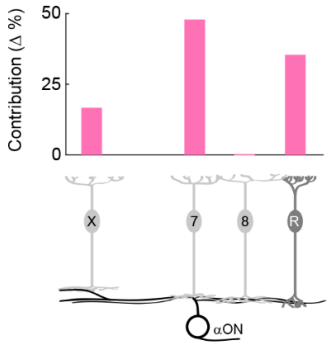

Figure 2.9 Bipolar cell types rewire with ONα-RGC in cell-type-specific ratios in *B6-DTA* mice

In *B6-DTA* mice, the number of excitatory synapses numbers on ONα-RGCs is reduced by 29.5 % compared to wild-type littermates. Given that B6 cells were shown to account for 70 % of the excitatory synapses on ONα-RGCs in wild-type retinas (Schwartz et al., 2012), it follows that non-B6 bipolar cells restore 40.5 % of the lost synapses in *B6-DTA* retinas. We calculated the approximate convergence of each bipolar cell type to ONα-RGCs by dividing the dendritic territory of the later by the axonal territory of the former. We then multiplied the convergence factor by the change in synapses numbers between pairs of individual bipolar cells and ONα-RGCs, to estimate the relative contribution each bipolar cell type to rewiring (XBC 17%, B7 47.4 %, RBC 35.6 %).

In addition to contrast responses, the temporal tuning of RGCs is determined by combined input from different bipolar cell types with unique response kinetics (Baden et al 2013a, Borghuis et al 2013, Franke et al 2017, Ichinose et al 2014). Measuring EPSCs during white noise stimulation, we found that the temporal tuning of bipolar cell input to ONα-RGCs was indistinguishable between *B6-DTA* mice and wild-type littermates (Figure 2.11A-2.11D).

Although our results clearly showed that presynaptic rewiring contributed to the preservation of ONα-RGCs' light responses, it was unclear, whether postsynaptic scaling also played a role in this homeostasis (Pozo & Goda 2010, Turrigiano 2008). To address this

question, we recorded spontaneous EPSCs (sEPSCs) from ONα-RGCs in wild-type and *B6-DTA* retinas. Recordings were performed in conditions that lowered the probability of vesicle fusion (i.e. zero extracellular calcium) to reduce coincidence of bipolar cell release events. We found that the distributions of sEPSC amplitudes were indistinguishable between wild-type and *B6-DTA* retinas (Figure 2.12). To explore further possible postsynaptic plasticity, we focally puffed glutamate onto dendrites of ONα-RGCs while recording EPSCs. We included a fluorescent dye (Alexa 488) in the puff solution and used 2-photon imaging to measure the application area. These experiments revealed smaller amplitudes of EPSCs per application area in *B6-DTA* mice compared to wild-type littermates (Figure 2.12). The amplitude reduction (31.6%) matched closely the reduction in synapse density on ONα-RGCs' dendrites (29%) (Figure 2.6E). Together these findings exclude broad changes in postsynaptic strength as a major contributor to the response homeostasis, and support the notion that, following B6 removal, ONα-RGCs adjust their connectivity with other bipolar cell types in specific ratios to replace the lost input and to preserve precisely their light responses (i.e. circuit-level homeostatic plasticity).

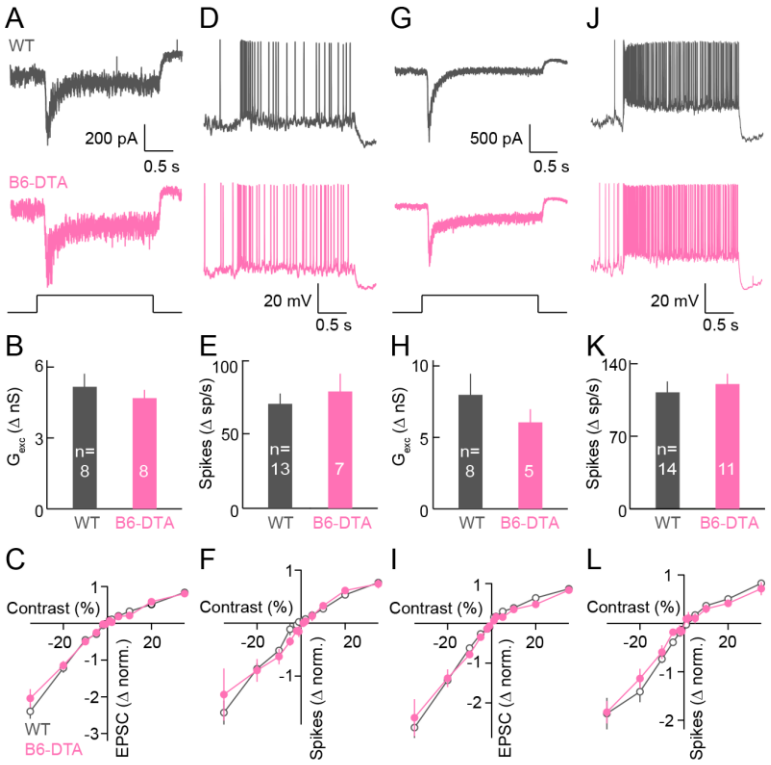

Figure 2.10 Cell-type-specific rewiring preserves contrast responses of ONα-RGCs in *B6-DTA* mice

(A and D) Representative EPSC traces (A) and spike responses (D) of ONα-RGCs in wild-type (*grey*) and *B6-DTA* (*pink*) mice in illumination conditions preferentially activating rods (mean intensity: 1.5 R*). (B and E) Summary data of excitatory conductances (B) and spike responses (E) of ONα-RGCs in wild-type (*grey*) and *B6-DTA* (*pink*) mice in illumination conditions preferentially activating rods. In (B), *WT*: 5.16 ± 0.55 nS; *B6-DTA*: 4.69 ± 0.35 nS; p = 0.48. In (E), *WT*: 70 ± 6.9 sp / s; *B6-DTA*: 78.3 ± 11.9 sp / s; p = 0.56. (C and F) Contrast response functions of the normalized excitation (C, *WT*: n = 11; *B6-DTA*: n = 9) and spike rate (F, *WT*: n = 12; *B6-DTA*: n = 10). (G and J) Analogous to A (G) and D (J), but in conditions preferentially activating cones (mean intensity: 1,500 R*). (H and K) Analogous to B (H) and E (K) but in illumination conditions preferentially activating cones. In (H), *WT*: 7.98 ± 1.48 nS; *B6-DTA*: 6.05 ± 0.92 nS; p = 0.29. In (K), *WT*: 112.4 ± 10.5 sp / s; *B6-DTA*: 120.4 ± 9.9 sp / s; p = 0.59. (I and L) Analogous to C (I, *WT*: n = 9; *B6-DTA*: n = 5) and F (L, *WT*: n = 14; *B6-DTA*: n = 8) but in illumination conditions preferentially activating cones.

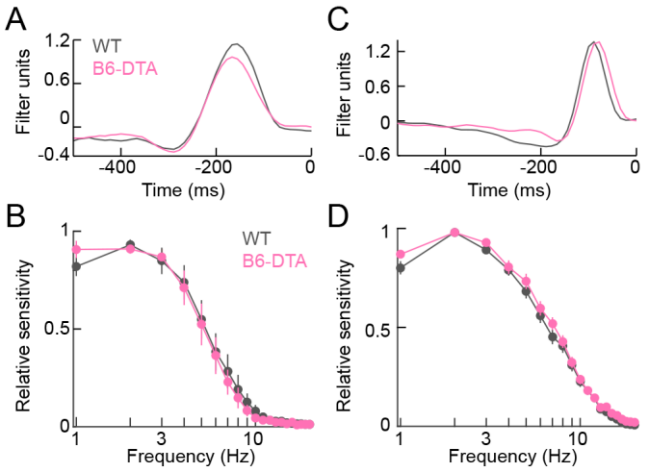

Figure 2.11 Cell-type-specific rewiring preserves temporal tuning of ONα-RGCs in *B6-DTA* mice

(A and C) Representative response-weighted stimulus response profiles of excitatory input to ONα-RGCs in conditions preferentially activating rods (A, mean intensity: 1.5 R*) and in conditions preferentially activating cones (C, mean intensity: 1,500 R*) recorded in wild-type (*grey*) and *B6-DTA* (*pink*) retinas. (B and D) Summary data (mean ± SEM) of temporal frequency-response functions computed from Fourier transforms of response-weighted stimulus response profiles in conditions preferentially activating rods (B, *WT*: n = 9, *grey*; *B6-DTA*: n = 8, *pink*) and in conditions preferentially activating cones (C, *WT*: n = 17, *grey*; *B6-DTA*: n = 17, *pink*).

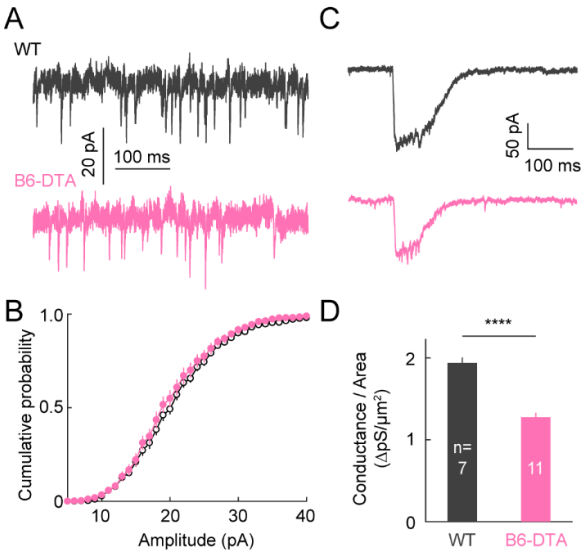

Figure 2.12 Lack of evidence for synaptic scaling in ONα-RGCs of *B6-DTA* mice

(A and B) Representative traces (A) and cumulative distribution curves (B) of sEPSCs recorded from ONα-RGCs in wild-type (n = 10) and *B6-DTA* (n = 5) retinas. (C and D) Representative traces (C) and summary data (D) of currents elicited by glutamate puffs in ONα-RGCs in wild-type (1.9 ± 0.07 pS / μm^2) and *B6-DTA* (1.3 ± 0.05 pS / μm^2, p = 2 *10^{-13}) retinas. The area of each application was estimated by 2-photon imaging of a fluorescent dye (Alexa 488) included in the puff solution.

2.4 Discussion

During development, most postsynaptic neurons recruit multiple presynaptic partners (i.e. convergence), and by establishing precise numbers of synapses with each partner attain specific function. Whether postsynaptic neurons establish cell-type-specific connectivity patterns with each input independently, or balance synapses from different input types to achieve specific function is unclear (Okawa et al 2014b, Yogev & Shen 2014). Here, we addressed this question in the convergent innervation of ONα-RGCs by bipolar cells.

Anatomical studies suggested that ONα-RGCs receive input from multiple bipolar cell types, with B6 cells contributing approximately 70 % of the excitatory synapses (Morgan et al 2011, Schwartz et al 2012, Soto et al 2012). In our study, optogenetic activation of B6 cells elicited large EPSCs in ONα-RGCs (Figure 2.1), indicating that functional connectivity in the inner retina matches anatomical connectivity (Morgan & Lichtman 2013), and that anatomical connectivity was correctly inferred from light microscopic circuit reconstructions (Figures 2.7 and 2.8) (Morgan et al 2011, Schwartz et al 2012, Soto et al 2012).

Understanding how signals from the 15 bipolar cell types are distributed and mixed among the 30-40 RGC types is a major challenge in deciphering the functional organization of the retina (Asari & Meister 2012, Baden et al 2016, Euler et al 2014). The results of our pharmacogenetic silencing experiments (Figure 2.1) indicate that in wild-type mice the light responses of ONα-RGCs are dominated by a single bipolar cell type (B6). These data are consistent with a recent receptive field model, which accurately predicts responses of ONα-RGCs to a variety of stimuli based on their input from B6 cells (Schwartz et al 2012). Whether

dominant input from a single bipolar cell type is the rule or an exception among RGCs remains to be determined (Calkins & Sterling 2007).

Using an intersectional transgenic strategy (*B6-DTA* mice), we selectively removed B6 cells from the developing retina (Figure 2.4). In *B6-DTA* mice, ONα-RGCs increased their connectivity with B7 cells, converting this minor input into the major one, formed connections *de novo* with XBCs (Figures 2.6 and 2.7), and maintained synapses from RBCs (Figure 2.8), which are normally eliminated during circuit maturation (Morgan et al 2011). Connections of B8 cells with ONα-RGCs were unaffected by B6 removal (Figure 2.7). Because B8 cells form synapses with ONα-RGCs in wild-type mice, but XBCs do not, the observed rewiring cannot solely reflect competition between bipolar cells. Rewiring reveals that postsynaptic neurons can dynamically adjust connectivity with converging presynaptic inputs rather than forming a fixed number of synapses with each independently. Thus, synaptic specificity in the inner retina is plastic rather than hard-wired. To what extent this is true of other neural circuits, remains to be determined (Yogev & Shen 2014). Interestingly, in the spinal cord, interneurons fail to innervate alternative partners when their primary targets (i.e. sensory fibers) are removed during development (Betley et al 2009). Differences in the stringency of synaptic specificity may have arisen to limit plasticity to circuits whose function it benefits.

In the retina, as elsewhere in the nervous system, multiple cellular mechanisms are sequentially engaged to establish synaptic specificity (Sanes & Yamagata 2009, Williams et al 2010, Yogev & Shen 2014). Relatively early during development, bipolar cell axons and RGC dendrites stratify in narrow sublaminae of the IPL (Kerschensteiner et al 2009, Kim et al 2010, Morgan et al 2006, Morgan et al 2008). Laminar targeting constrains potential connectivity,

differs between cell types, and is determined by a combination of repulsive and adhesive cues (Duan et al 2014, Matsuoka et al 2011a, Matsuoka et al 2011b, Yamagata & Sanes 2008, Yamagata & Sanes 2012). After lamination is complete, connectivity patterns of co-stratifying bipolar cell axons are initially similar, but subsequently diverge through cell-type-specific changes in the conversion of axo-dendritic contacts into synapses (i.e. connectivity fraction) (Morgan et al 2011). We find that plasticity elicited by B6 removal selectively engages this mechanism. The morphologies of bipolar cell axons and ONα-RGC dendrites, and the numbers of contacts between them are unchanged in *B6-DTA* compared to wild-type mice, but the connectivity fractions of axo-dendritic contacts are altered in a cell-type-specific manner (Figures 2.6-2.8). Because bipolar cell types with similar responses show overlapping axonal stratification patterns (Baden et al 2013a, Borghuis et al 2013, Euler et al 2014, Franke et al 2017), rewiring within a constant laminar position may best allow ONα-RGCs to regain their specific function. Even within a constant laminar position, however, ONα-RGCs make distinct choices in normal development (Morgan et al 2011) and in plasticity (e.g. not to increase connectivity with B8). Furthermore, it is worth noting that the laminar constraint on rewiring is not absolute. Thus, when several ON cone bipolar cell types as well as rod bipolar cells are removed during development, ONα-RGC extend dendritic arbors into outer IPL and recruit input from OFF cone bipolar cells (Okawa et al 2014a).

Homeostatic plasticity had previously been shown to stabilize average firing rates (Hengen et al 2013, Turrigiano & Nelson 2004) and spontaneous activity patterns of neurons (Blankenship & Feller 2010, Kerschensteiner 2014), but how it regulates their unique circuit functions remained unclear. In assessing the functional consequences of plasticity in *B6-DTA* mice, we find that it not only rescues overall activity levels of ONα-RGCs, but indeed precisely

restores their contrast (Figure 2.10) and temporal response properties (Figure 2.11), both of which RGCs inherit from their combined bipolar cell inputs. Our sEPSC recordings and glutamate puff experiments suggest that postsynaptic scaling does not play a major role in this response preservation (Figure 2.12). Instead, homeostatic plasticity controls cell-type-specific wiring of presynaptic inputs (i.e. bipolar cells) expanding its reach beyond the intrinsic and synaptic mechanisms previously characterized at the level of individual neurons (Pozo & Goda 2010, Turrigiano 2008, Wefelmeyer et al 2016). In this way, circuit-level homeostatic plasticity shapes cell-type-specific wiring in the inner retina and stabilizes visual information sent to the brain.

Chapter 3 : Genetically Identified Suppressed-by-Contrast Retinal Ganglion Cells Reliably Signal Self-Generated Visual Stimuli

Spike trains of retinal ganglion cells (RGCs) are the sole source of visual information to the brain; and understanding how the approximately 20 RGC types in mammalian retinas respond to diverse visual features and events is fundamental to understanding vision. Suppressed-by-Contrast RGCs (SbC-RGCs) stand apart from all other RGC types in that they reduce rather than increase firing rates in response to light increments (ON) and decrements (OFF). Here, we genetically identify and morphologically characterize SbC-RGCs in mice, and target them for patch clamp recordings under 2-photon guidance. We find that strong ON inhibition (glycine > GABA) outweighs weak ON excitation, and that inhibition (glycine > GABA) coincides with decreases in excitation at light OFF. These input patterns explain the suppressive spike responses of SbC-RGCs, which are observed in dim and bright light conditions. Inhibition to SbC-RGC is driven by rectified receptive field subunits, leading us to hypothesize that SbC-RGCs could signal pattern-independent changes in the retinal image. Indeed, we find that shifts of random textures matching saccade-like eye movements in mice elicit robust inhibitory inputs and suppress spiking of SbC-RGCs over a wide range of texture contrasts and spatial frequencies. Similarly, stimuli based on kinematic analyses of mouse blinking consistently suppress SbC-RGC spiking. Receiver operating characteristics show that SbC-RGCs are reliable indicators of self-generated visual stimuli that may contribute to central processing of blinks and saccades.

3.1 Introduction

Spiking neurons in sensory systems typically signal stimulus features or events by increasing their firing rate. Accordingly, RGCs are often divided into ON, OFF and ON-OFF types, which enhance firing to increases in luminance, decreases in luminance and both, respectively (Masland 2001a). In 1967, Levick et al. and Rodieck discovered RGCs that deviate from these response patterns and are suppressed by ON and OFF stimuli (Levick 1967, Rodieck 1967). Since the original studies in rabbits and cats, Suppressed-by-Contrast (SbC) RGCs have also been recorded in macaques (de Monasterio 1978), and matching responses have been observed in downstream visual areas: the dorsolateral geniculate nucleus (dLGN) in macaques (Tailby et al 2007), and the dLGN and primary visual cortex in mice (Niell & Stryker 2010, Piscopo et al 2013), suggesting that SbC signals are a conserved output of mammalian retinas and propagate through the early visual system. In spite of recent progress (Sivyer et al 2010), the circuit mechanisms underlying suppressive responses remain incompletely understood and how SbC-RGCs contribute to the detection of specific visual features or events has not been explored in detail.

In addition to changes in the external world, the retina experiences self-generated visual stimuli. These include image shifts caused by saccades or saccade-like eye movements (Sakatani & Isa 2007) and blackouts due to eyelid blinks (Burr 2005). Both saccades and blinks are omitted from conscious visual experience (Burr 2005, Ross et al 2001). Suppression of visual sensitivity during saccades and blinks is thought to contribute to their omission and appears to involve a combination of retinal and extraretinal mechanisms (Burr 2005, Mackay 1970, Noda & Adey 1974). RGC types were shown to differ in their responses to saccades (Noda & Adey 1974, Roska & Werblin 2003), whereas blink responses have not yet been characterized.

Here, we identify SbC-RGCs in mice, and use a combination of transgenic and viral strategies to characterize their dendritic morphology. We target SbC-RGCs under 2-photon guidance for patch clamp recordings and analyze synaptic mechanisms underlying their contrast responses. Based on insights into these mechanisms, we hypothesize that SbC-RGCs could signal self-generated visual stimuli. In support of this notion, we find that SbC-RGCs respond reliably to stimuli mimicking saccade-like eye movements and blinks, suggesting that they may contribute to the central processing of these events.

3.2 Materials and Methods

3.2.1 Mice

Throughout this study, we used young adult (postnatal day 25 - 35) C57BL/6J (*WT*) mice, or *CCK-ires-Cre* (Taniguchi et al 2011) mice crossed to a fluorescent reporter strain (*Ai9*) (Madisen et al 2010) or injected with AAV vectors. All procedures were approved by the Animal Studies Committee of Washington University School of Medicine and performed in compliance with the National Institutes of Health *Guide for the Care and Use of Laboratory Animals*.

3.2.2 Adeno-associated viruses (AAV)

Two Brainbow AAV vectors (AAV9-hEF1a-lox-TagBFP-lox-eYFP-lox-WPRE-hGH-InvBYF and AAV9-hEF1a-lox-mCherry-lox-mTFP1-lox-WPRE-hGH-InvCheTF) (Cai et al 2013) were injected (1:1, 250 nL) into the vitreous of newborn *CCK-ires-Cre* mice as described before (Soto et al 2013).

3.2.3 Tissue preparation

Dark-adapted (> 2 hr) mice were euthanized and retinas isolated under infrared illumination (> 900 nm) as previously described (Akrouh & Kerschensteiner 2013).

3.2.4 Imaging

Fixed retinas (30 min in 4 % paraformaldehyde) were imaged on an Fv1000 confocal microscope (Olympus) using a 60 X 1.35 NA oil-immersion objective. Images were acquired at a voxel size of 0.206 µm - 0.3 µm (x/y-z).

3.2.5 Electrophysiology

Cell-attached and whole-cell patch clamp recordings were obtained in dorsal halves (Wang et al 2011) of dark-adapted retinas superfused (5-7 mL/min) with warm (30-33 °C) mouse artificial cerebrospinal fluid containing (Akrouh & Kerschensteiner 2013). Pharmacological antagonists were used in the following concentrations: 1,2,5,6-500 Tetrahydropyridine-4-yl-methyl phosphinic acid (TPMPA, 50 µM, Sigma), Gabazine (10 µM, Tocris) and Strychnine (1 µM, Sigma). Intracellular voltage- and current-clamp solutions for were identical to those used before (Akrouh & Kerschensteiner 2013). Reported voltages were corrected for liquid junction potentials. Excitatory (EPSCs) and inhibitory postsynaptic currents (IPSCs) were recorded at the reversal potential for Cl^- (-60 mV) and cations (0 mV), respectively. SbC-RGCs were targeted under 2-photon guidance in *CCK-ires-Cre Ai9* mice. Correct targeting was confirmed by monitoring diffusion of a fluorescent dye (Alexa 488) from the recording electrode into the soma during break in and by reconstructing the morphology of dendrites at the end of each recording. MEA recordings were performed with 252-electrode arrays (Multichannel Systems) and spike trains sorted as previously described (Akrouh and Kerschensteiner, 2013). We used MEA data to compare responses of a large population of non-SbC-RGCs to genetically identified SbC-RGCs recorded via patch clamp. Towards this end, we removed RGCs showing suppressive responses to positive and negative contrast steps from our MEA data.

3.2.6 Blink recordings

To measure the kinematics of blinking, freely moving mice were filmed at 500 frames/s with a high speed video camera (IDT). Room lighting (corneal irradiance: 2 x 10^{13} photons/cm^2/s) was supplemented by illumination from an infrared LED (peak wavelength: 940 nm). A total of 11 blinks were recorded from four female *WT* mice. Eyelid separation as a function of time was analyzed using ImageJ (NIH). On average (± SEM) blinks lasted 114 (± 10) ms.

3.2.7 Visual stimuli

Stimuli were written in MATLAB (The Mathworks) using Cogent graphics extensions (John Romaya, University College London) and presented on an organic light-emitting display (eMagin, refresh rate: 60 Hz) focused onto photoreceptors. Stimuli were centered on the soma of the recorded cell (patch clamp) or on the electrode array (MEA). Unless noted otherwise, the mean intensity of stimuli was 1,500 rhodopsin isomerization/rod/s (1,500 R*), calculated based on a collection area of 0.87 μm^2 (Lyubarsky et al 2004). To probe spatial response profiles, the intensity of a circular area of varying size was square-wave-modulated at 0.25 Hz (Michelson contrast: 100 %). To test contrast sensitivity, 250-ms luminance steps from the mean intensity were shown over the receptive field center every 2.25 s. To evaluate responses to saccade-like eye movements, patterns with different contrasts (Michelson contrast: 25 %, 50 % or 100 %) and texture scales (50 μm, 100 μm or 200 μm) were generated by convolving random binary maps with 2D Gaussian filters. Textures were fixed for 1 s followed by 100 ms shifts in random directions over 14˚ of visual space, matching properties of saccade-like eye movements in mice (Sakatani & Isa 2007). Blinks were simulated using the same random patterns and lasted 117 ms (i.e. 7 frames). During the first three frames the random pattern stimulus was dimmed in equal increments from a mean of 1,500 R* to 1.5 R*. The display remained at 1.5 R* for one

additional frame before it brightened back to 1,500 R* over the next three frames. When testing the reliability of eye movement and blink detection, trials of the respective stimuli were alternated.

3.2.8 Analysis

Electrophysiology data were analyzed using scripts written in MATLAB. Responses (spike rate, conductance or charge) were measured as baseline-subtracted averages during 100 - 200 ms time windows. The ability to detect blinks and saccades based on responses of SbC-RCGs was analyzed using receiver operating characteristics (ROC) (Britten et al 1992). To construct ROC curves, we compared firing rates during pre-stimulus (r_{pre}) and stimulus (r_{stim}) time windows to ten threshold values (z) spanning the range of r_{pre} and plotted the hit rate (β) as a function of the false alarm rate (α), with α and β defined by the following probabilities (P):

$$\alpha(z) = P\left(r_{pre} \leq z\right)$$

$$\beta(z) = P(r_{stim} \leq z)$$

The performance of each cell was then quantified by the area under its ROC curve, a parameter that varies from 0.5 for chance performance to a maximal value of 1.

Territories of ON and OFF dendrites were measured as the areas of the smallest convex polygons to encompass the respective arbors in maximum intensity projections in ImageJ.

Population data are reported as mean ± SEM throughout the text. Paired and unpaired t tests were used to assess statistical significance of observed differences.

3.3 Results

Rabbit SbC-RGCs (or uniformity detector RGCs) are bistratified neurons with larger ON arbors in sublaminae 4/5 (S4/5) of the inner plexiform layer and smaller OFF arbors in S1, from where branches frequently dive back to S4/5 (Sivyer et al 2010). RGCs with similar features were recently described in CCK-ires-Cre mice (Zhu et al 2014). To further analyze the morphology of these cells, we injected Brainbow AAVs (Cai et al 2013) into the vitreous of CCK-ires-Cre mice. Approximately half of the RGCs labeled in this way resembled rabbit SbC-RGCs. Their ON dendrites cover larger territories than their OFF dendrites (Fig. 3.1A, 3.1B), and both arbors are connected by numerous ascending and descending processes distributed evenly across dendritic fields (Fig. 3.1C). In targeted patch clamp recordings, these neurons showed high baseline firing rates (18.7 ± 1.7 Hz, n = 16) that were transiently suppressed by light increments and decrements in rod- and cone-dominant conditions, identifying them as SbC-RGCs (Fig. 3.1D).

Probing spatial profiles of ON and OFF responses, we found that spike suppression of SbC-RGCs increases with stimulus size, plateauing for spot diameters greater than 200 μm (Fig. 3.2A, 3.2B). Voltage clamp recordings revealed that SbC-RGCs receive strong synaptic inhibition with moderate surround suppression at light ON and OFF (Fig. 3.2D-3.2F). By comparison, excitatory input was weak and increased at light ON, but decreased from baseline at light OFF (Fig. 3.2G-3.2I), and showed no surround suppression. Aligned with the peak of ON excitation, some SbC-RGCs showed a transient increase in firing preceding spike suppression.

We next characterized the contrast sensitivity of spike responses and synaptic inhibition of SbC-RGCs, presenting 250-ms light steps from a gray background in a circular area (diameter: 200 μm) centered on the cell. Positive and negative contrast steps with increasing amplitudes progressively suppress firing of SbC-RGCs (Fig. 3.3A, 3.3B) and elicit increasing

IPSCs (Fig. 3.3C, 3.3D). Suppression by ON stimuli is weaker than by OFF stimuli and is preceded, on average, by a transient increase in firing. Both features are likely the results of ON excitation (Fig. 3.2G-3.2I).

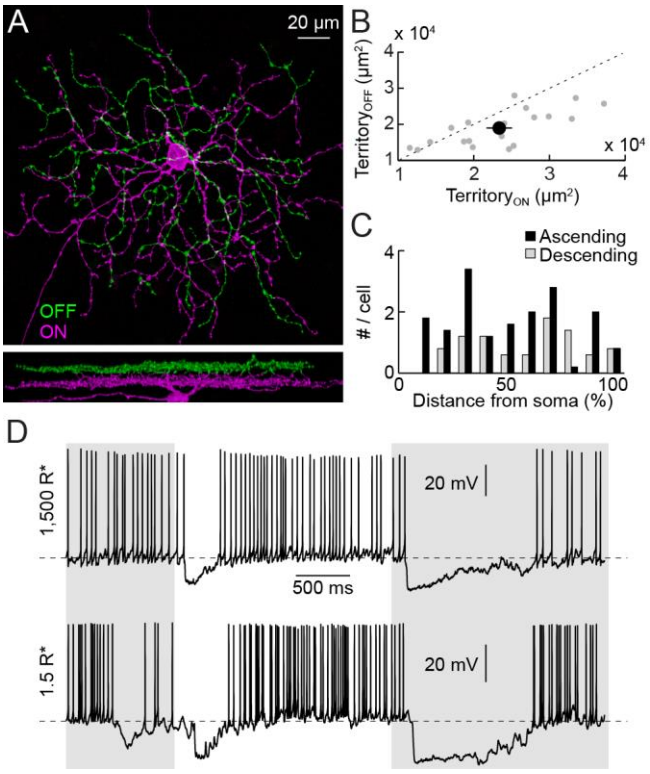

Figure 3.1 Morphology and light responses of SbC-RGCs

(A) Top down (top panel) and side (bottom panel) views of an SbC-RGC labeled by Brainbow AAV infection. Dendrites in the OFF (ON) sublamina are shown in green (magenta). Their stratification in S1 (S4/5) was confirmed by staining for choline acetyltransferase (data not shown). (B) Scatter plot of ON vs. OFF dendritic territories measured as the areas of the smallest convex polygons to encompass the respective arbors in z-projections. Gray dots show data from individual cells (n = 19) and the black circle (errorbars) indicates the mean (± SEM) of the population. (C) Distribution of ascending and descending branches as a function of distance from the soma to the edge of the dendritic field (n = 5). (D) Spike responses of SbC-RGCs to a stimulus in which intensity of a spot (diameter: 200 µm) was modulated by a step function (2 s ON, 3 s OFF) in cone- (mean intensity: 1500 R*, top trace) and rod-dominant illumination conditions (mean intensity: 1.5 R*). Periods of light OFF are shaded in gray. Resting membrane potentials (1,500 R*: -54 mV, 1.5R*: -53 mV) are indicated by dashed lines.

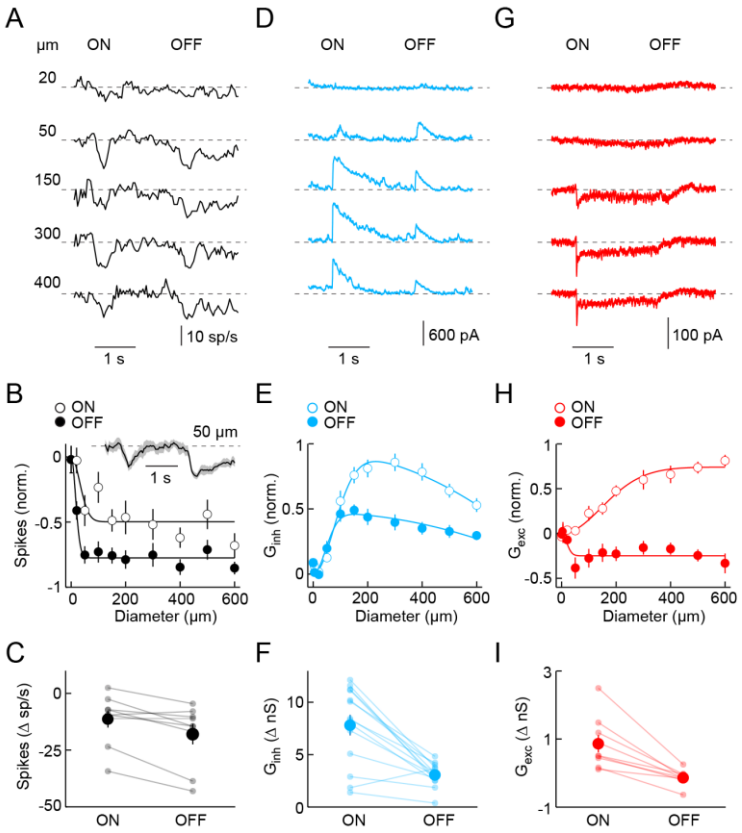

Figure 3.2 Spatial response and synaptic input profiles of SbC-RGCs

(A, D, and G), Representative spike (A, 40-ms bins), IPSC (D) and EPSC (G) responses to stimuli in which intensity in a circular area (diameter noted in A) is modulated by a square wave (2 s ON, 2 s OFF). (B, E, and H), Summary data of ON (open circles) and OFF (filled circles) sensitivity profiles of SbC-RGCs for spike responses (B, n = 9), inhibitory (E, n = 14, G_{inh}) and excitatory synaptic conductances (H, n = 9, G_{exc}). Responses of each cell were normalized to the maximal absolute response amplitude of that cell. The average (± SEM) spike response of SbC-RGCs to 50 μm stimuli is shown as a line (shaded area) inset in B. Single-Gaussian (B, H) and Difference-of-Gaussian (E) fits are shown as solid lines. (C, F, and I), Amplitudes of ON and OFF responses to circles with a diameter of 300 μm. Dots show data from individual cells and circles (errorbars) indicate mean (±SEM) of respective population. Spike suppression was greater at light OFF than ON ($p < 0.01$, n = 9), inhibition (G_{inh}) greater at light ON than OFF ($p < 10^{-4}$, n = 14), and excitation (G_{exc}) greater at light ON than OFF ($p < 0.01$, n = 9).

To elucidate the mechanisms of SbC-RGC inhibition, we applied antagonists of $GABA_A$, $GABA_C$ and glycine receptors. Results from these experiments indicate that glycinergic amacrine cells are the dominant source of ON and OFF inhibition to SbC-RGCs (Fig. 3.3E-3.3G).

GABAergic amacrine cells contribute to the inhibitory input, via a mixture of $GABA_A$ and $GABA_C$ receptors at light ON, and only $GABA_C$ receptors at light OFF. Different amacrine cells and postsynaptic receptors thus cooperate to suppress spiking of SbC-RGCs.

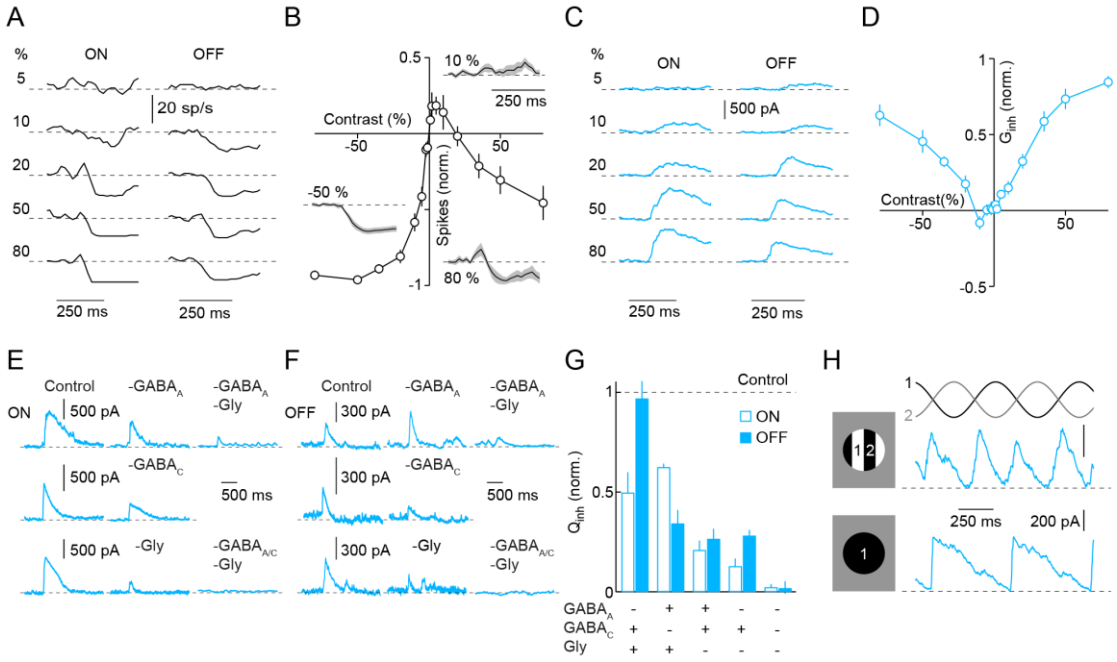

Figure 3.3 Contrast responses functions and pharmacology of SbC-RGCs

(A and C), Representative spike (A, 20-ms bins) and IPSC (C) responses to positive (ON, left column) and negative (OFF, right column) contrast steps presented in a spot (diameter: 200 µm) centered on the recorded cell. Bars indicate the duration of each step. (B and D), Contrast response functions of the normalized spike rate (B, n = 9) and the inhibition (D, n = 6). The average (± SEM) spike responses of SbC-RGCs to -50 %, 10 % and 80 % contrast steps (Weber contrast) are shown as a lines (shaded areas) inset in B. (E and F), Representative IPSC traces elicited by ON and OFF steps (diameter: 200 µm) in the presence of Gabazine (-$GABA_A$), Strychnine (-Gly), TPMPA (-$GABA_C$) and combinations thereof. (G), Normalized charge measurements (Q_{inh}) (mean ± SEM) show decreased ON ($p < 0.003$, n = 5) but not OFF ($p > 0.5$) inhibition in the presence of Gabazine, decreased ON ($p < 0.05$, n = 4) and OFF ($p < 0.05$) inhibition in the presence of TPMPA, decreased ON ($p < 10^{-4}$, n = 5) and OFF ($p < 10^{-3}$) inhibition in the presence of Strychnine, decreased ON ($p < 0.03$, n = 4) and OFF ($p < 0.05$) inhibition in the presence of Gabazine and Strychnine, and decreased ON ($p < 10^{-6}$, n = 4) and OFF ($p < 10^{-5}$) inhibition in the presence of Gabazine and Strychnine and TPMPA. (H), Representative IPSCs elicited by counter-phase-modulation of a narrow grating (bar width: 50 µm) over the receptive field (diameter: 200 µm) (top panel) are compared to IPSCs elicited by uniform sine-wave-modulation of the same area (bottom panel).

Stimulation with narrow sign-inverting gratings elicited frequency doubled IPSCs indicating that inhibitory receptive fields of SbC-RGCs are composed of rectified subunits (Fig. 3.3H) (Enroth-Cugell & Robson 1966, Schwartz et al 2012). The combination of this nonlinear spatial integration and suppression by full-field stimuli (Fig. 3.2), led us to hypothesize that SbC-RGCs could signal pattern-independent global changes in the retinal image. Global image changes are characteristic of self-generated visual stimuli, including eye movements (image shifts) and blinks (blackouts). Random texture images shifted with kinetics matching saccade-like eye movements in mice (Sakatani & Isa 2007), elicited strong inhibitory inputs independent of the image contrast (25 % - 100 %, Fig. 3.4A). As a result, spiking of SbC-RGCs was consistently suppressed by this stimulus, whereas most other RGCs failed to respond or increased their firing (Fig. 3.4B). Similarly invariant synaptic inhibition and spike suppression were observed in SbC-RGCs, and no responses or increased firing in other RGCs, when the texture scales of the shifted images were altered (50 μm - 200 μm, Fig 3.4C, 3.4D). To characterize the reliability of this response, SbC-RGCs were shown a series of ten random image shifts. The consistency of spike suppression reflected in receiver operating characteristic (ROC) curves constructed from their responses suggests that SbC-RGCs can reliably signal saccade-like eye movements (Fig. 3.4E, area under curve: 0.89 ± 0.02, $n = 5$).

We used high speed videography to analyze mouse blinking (Fig. 3.4F). Presentation of image blackouts with dimming kinetics matching recorded blinks consistently suppressed SbC-RGCs irrespective of image patterns preceding and following the blink (Fig. 3.4F). Moreover, blink responses and ROC curves (area under curve: 0.93 ± 0.02, $n = 5$) closely resembled those observed for saccade-like eye movements, suggesting that SbC-RGCs may provide a unified signal for these events, which are similarly omitted from visual experience.

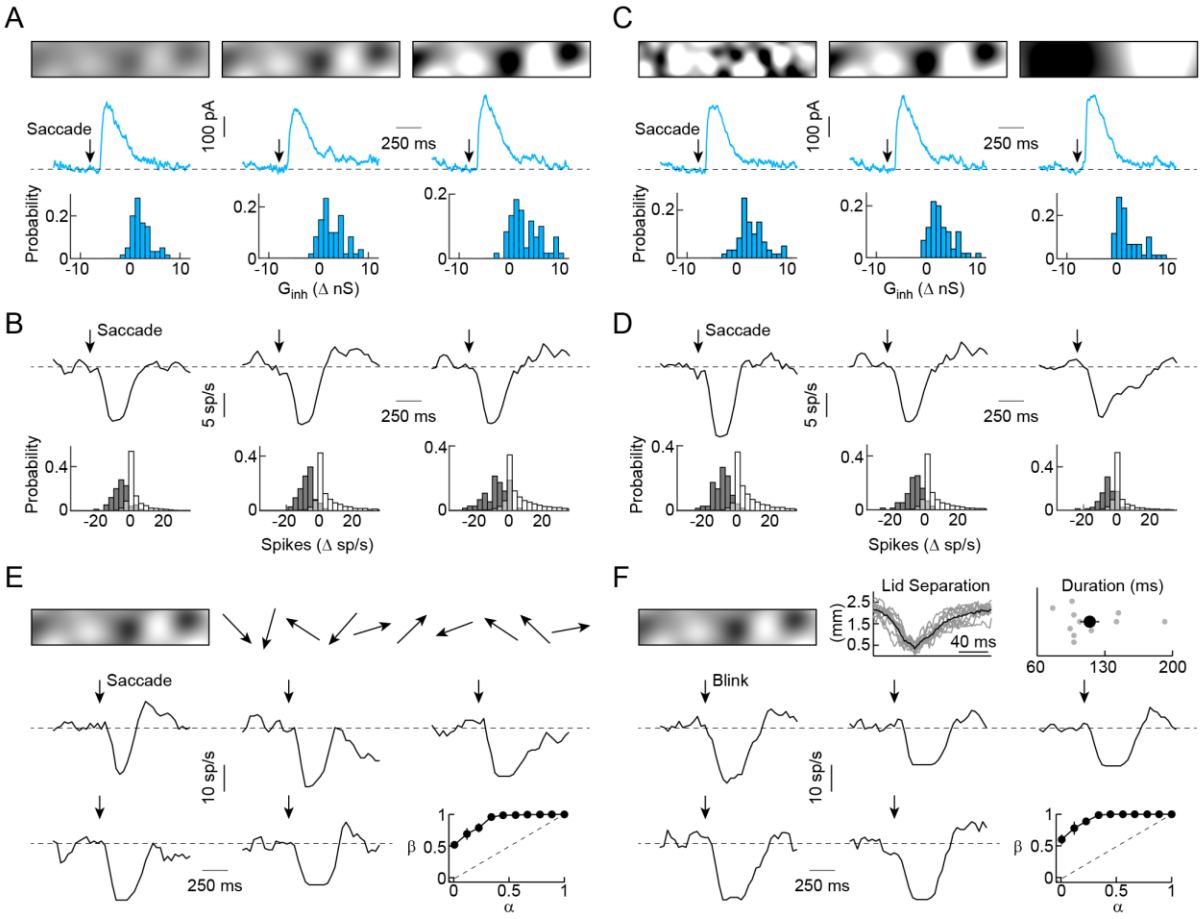

Figure 3.4 SbC-RGC responses to stimuli mimicking saccade-like eye movements and blinks

(A and B), IPSC (A) and spike (B, 40-ms bins) responses to shifts of random textures with different contrasts (25 %, 50 %, 100 %). A, Top: Illustrations of image patterns. Middle: Representative IPSC responses to shifted images with different contrasts (texture scale: 100 µm). Bottom: Probability distribution of inhibitory (G_{inh}) responses to saccade-like stimuli (n = 60 saccades recorded in four SbC-RGCs). B, Top: Representative spike responses to the same stimuli as in A. Bottom: Probability distribution of spike responses of SbC-RGCs (grey bars, n = 105 saccades recorded in seven cells) and non-SbC RGCs (white bars, n = 3,615 saccades recorded in 241 cells on MEAs) (C and D), Analogous to A (C) and B (D), but for shifts of images with different texture scales (50 µm, 100 µm, 200 µm) as illustrated at the top. The same numbers of saccades and cells were recorded in C and D as in A and B, respectively. Traces in A and C, and B and D, were recorded in the same cell and two examples are therefore repeated. (E and F), Representative spike responses to stimuli mimicking a series of saccade-like eye movements (E) and blinks (F). E, Top: Texture images (contrast: 50 %, scale: 100 µm) shifted successively in ten random directions. Below: Representative spike responses (40-ms bins) to image shifts and mean (± SEM) ROC curves (bottom right) illustrating the ability to detect shifts based on SbC-RGC responses (n = 5 cells). The dashed line shows the unity diagonal of hit rate (β) and false-alarm rate (α). F, Top middle: Eyelid separation as a function of time recorded in four WT mice. Thin grey

traces show individual blinks, whereas the thick black line indicates the population average. Top right: The distribution of blink durations. Grey dots show data from each blink (n = 11) and the black circle (errorbar) indicates mean (± SEM) of population. Below: Representative spike responses to blackouts and mean (± SEM) ROC curves (bottom right) illustrating the ability to detect blinks based on SbC-RGC responses (n = 5 cells).

3.4 Discussion

The mouse SbC-RGCs identified here share key response properties with SbC-RGCs in other species (de Monasterio 1978, Levick 1967, Rodieck 1967, Sivyer et al 2010). Morphological features of these cells appear to also be conserved (Fig. 3.1) (Sivyer & Vaney 2010). Bistratification facilitates convergence of ON and OFF inhibitory inputs onto SbC-RGC dendrites, which is critical for their responses. The frequent transitions of dendrites between layers imply that ON and OFF inputs can interact before reaching the soma, but the functional significance of this arrangement remains to be tested.

High spontaneous firing rates of SbC-RGCs lay the foundation for stimulus encoding by suppression. Rabbit SbC-RGCs receive tonic excitation and generate complex spikes, i.e. Na^+ spikelets riding atop slower Ca^{2+}-mediated depolarizations (Sivyer et al 2010). Mouse SbC-RGCs similarly receive tonic excitatory input, but generate simple spikes (Fig. 3.1). Simple spikes tend to be transmitted more reliably than their complex counterparts (Khaliq & Raman 2005), suggesting that responses of SbC-RGCs propagate faithfully through the early visual system of mice and are the source of suppressed-by-contrast responses in dLGN and V1 (Niell & Stryker 2010, Piscopo et al 2013).

In response to positive, but not negative, contrast steps, spike suppression of SbC-RGCs is preceded by a transient increase in firing (Fig. 3.3). This asymmetry, which is explained by differences in synaptic excitation at light ON and OFF (Fig. 3.2), could be used by downstream

areas to determine the direction of contrast transitions (positive or negative), whereas the extent of suppression signals the absolute amplitude of the respective change. It is worth noting, that for patterned stimuli (Fig. 3.4), which simultaneously recruit ON and OFF pathways, responses are purely suppressive, reflecting the overall dominance of inhibitory inputs.

Glycinergic amacrine cells provide a majority of ON and OFF inhibition (Fig. 3.3) (Sivyer et al 2010). The remaining input appears to be mediated by $GABA_A$ and $GABA_C$ receptors at light ON and only $GABA_C$ receptors at light OFF. Because inhibitory receptive fields are composed of rectified subunits, inhibition can be elicited by texture movements irrespective of the precise patterns involved (Fig. 3.4) (Enroth-Cugell & Robson 1966, Schwartz et al 2012). This property combined with suppressive responses to full-field stimuli, led us to hypothesize that SbC-RGCs could signal global changes in the retinal image that occur during eye movements and blinks. The reliable suppression we observe when simulating saccade-like eye movements and blinks support this notion. Given these responses, the conservation of SbC signals across mammalian species (de Monasterio 1978, Levick 1967, Rodieck 1967, Sivyer et al 2010), and their propagation up to primary visual cortex (Niell & Stryker 2010, Piscopo et al 2013, Tailby et al 2007), it is tempting to speculate that SbC-RGCs may contribute to central processing of saccades and blinks (Burr 2005, Noda & Adey 1974).

Although most mouse RGCs failed to respond or showed increased firing to saccade-like stimuli presented here (Fig. 3.4), several non-SbC-RGCs were shown to be suppressed by image shifts in rabbit retinas (Roska & Werblin 2003). Thus, as for other features (i.e. motion direction) multiple RGC types may cooperate in the detection of eye movements. SbC-RGCs are suppressed by a range of stimuli (Levick 1967, Sivyer et al 2010). Given the pattern invariance

of their responses, global image changes during saccade-like eye movements and blinks, are expected to synchronously suppress most SbC-RGCs, generating a specific population signal. The similarity of responses to saccade-like eye movements and blinks suggest that SbC-RGCs may provide a unified signal for these self-generated stimuli.

Chapter 4 : Target-Specific Glycinergic Transmission from VGluT3-Expressing Amacrine Cells Shapes Suppressive Contrast Responses in the Retina

Neurons that release more than one transmitter exist throughout the CNS. Yet, how these neurons deploy multiple transmitters and shape the function of specific circuits is not well understood. VGluT3-expressing amacrine cells (VG3-ACs) provide glutamatergic input to ganglion cells activated by contrast and motion. Using optogenetics, we find that VG3-ACs provide selective glycinergic input to a retinal ganglion cell type suppressed by contrast and motion (SbC-RGCs). Firing of SbC-RGCs is suppressed at light ON and OFF over a broad range of stimulus sizes. Anatomical circuit reconstructions reveal that VG3-ACs form inhibitory synapses preferentially on processes that link ON and OFF arbors of SbC-RGC dendrites. Removal of VG3-ACs from mature circuits reduces inhibition and attenuates spike suppression of SbC-RGCs in a contrast- and size-selective manner, illustrating the modularity of retinal circuits. VG3-ACs thus use dual transmitters in a target-specific manner, and shape suppressive contrast responses in the retina by glycinergic transmission.

4.1 Introduction

Classically, each neuron was thought to use a single transmitter to send uniform signals across all its synapses (i.e. Dale's principle) (Strata & Harvey 1999). In recent years however, it has become clear that the output of neurons can be more diverse (Hnasko & Edwards 2012, Vaaga et al 2014). Neurons that release neuromodulatory peptides or monoamines often release a fast

transmitter as well, emitting parallel signals that act over different spatial and temporal scales (Contini & Raviola 2003, Nusbaum et al 2001, Tritsch et al 2012). In addition, some neurons release two fast transmitters. The identification of dual-transmitter neurons has been facilitated by optogenetics; and co-release of excitatory (Gras et al 2008, Ren et al 2011), inhibitory (Apostolides & Trussell 2013, Jonas et al 1998, Wojcik et al 2006), and excitatory and inhibitory fast transmitters (Noh et al 2010, O'Malley et al 1992, Root et al 2014, Saunders et al 2015) have all been reported. How neurons use dual transmitters to support specific circuit functions, however, is not well understood.

Some dual transmitters share a vesicular transporter (Jonas et al 1998, Tritsch et al 2012, Wojcik et al 2006) or are packaged into the same vesicles by synergistic action of two transporters (Gras et al 2008, Hnasko & Edwards 2012). These transmitters are co-released at all synapses of the respective neurons, which send the same complex signal to all their targets. By contrast, recent studies revealed spatial separation of vesicle pools containing monoamines and fast neurotransmitters in some axons (Chuhma et al 2014, Gagnon & Parent 2014, Onoa et al 2010, Zhang et al 2015). This in principle enables the respective neurons to send different messages to different targets. Whether neurons can selectively deploy two fast transmitters, particularly excitatory and inhibitory ones, to send opposite signals to specific targets and, if so, how these signals shape the function of postsynaptic partners is unclear.

Amacrine cells (ACs) are a diverse class of retinal interneurons. One of the 30-50 distinct AC types in mice expresses the vesicular glutamate transporter 3 (VGluT3). VGluT3-expressing ACs (VG3-ACs) are conserved from rodents to primates (Haverkamp & Wassle 2004, Johnson et al 2004), and prefer light decrements (OFF) to increments (ON) (Grimes et al 2011, Kim et al 2015, Lee et al 2014) and small stimuli to large ones (i.e. size selectivity) (Kim et al 2015, Lee et

al 2014). Recent anatomic and functional studies showed that VG3-ACs provide selective glutamatergic input to several types of retinal ganglion cells (RGCs), output neurons of the eye, which share response properties with VG3-ACs (Kim et al 2015, Krishnaswamy et al 2015, Lee et al 2014). Elsewhere in the nervous system, VGluT3 is associated with dual transmitter phenotypes (Gagnon & Parent 2014, Gras et al 2008, Noh et al 2010). VG3-ACs express an uptake transporter for glycine and accumulate glycine in their cytosol, but appear to lack the transporter for its vesicular packaging (Haverkamp & Wassle 2004, Johnson et al 2004). Thus, whether VG3-ACs release glycine, which RGC types are targets of this putative inhibitory transmission and how their output is shaped by VG3-AC input is unknown.

Unlike other RGCs, Suppressed-by-Contrast RGCs (SbC-RGCs) encode contrast through depressions in tonic firing (Levick 1967, Rodieck 1967). SbC-RGCs are conserved from rodents to primates (de Monasterio 1978, Tien et al 2015), and are suppressed by ON and OFF stimuli, large and small (Jacoby et al 2015, Tien et al 2015). Their responses propagate through the retino-geniculo-cortical pathway (Niell & Stryker 2010, Piscopo et al 2013). The circuit mechanisms giving rise to the unique responses of SbC-RGCs are incompletely understood, but involve strong inhibitory synaptic inputs at light ON and OFF (Sivyer et al 2010, Tien et al 2015). A recent study revealed that ON inhibition is mediated by Crh1-ACs and likely AII-ACs (Jacoby et al 2015). The source of OFF inhibition remains unknown.

Using optogenetics, we discover that VG3-ACs provide selective glycinergic input to SbC-RGCs. Anatomic circuit reconstructions reveal that VG3-ACs form inhibitory synapses preferentially on the ascending and descending processes that link the bistratified dendrites of SbC-RGCs. Genetic deletion of VG3-ACs in mature circuits reduces OFF inhibition to SbC-RGCs particularly in response to small stimuli, and attenuates suppressive spike responses with

similar contrast bias and size selectivity. VG3-ACs thus are dual-transmitter neurons that deploy excitatory and inhibitory transmitters in a target-specific manner, using glycinergic transmission to shape suppressive contrast responses in the retina.

4.2 Materials and Methods

4.2.1 Mice

We used BAC transgenic mice in which Cre recombinase is expressed under control of regulatory sequences of the *Slc17a8* gene, which encodes VGluT3 (*VG3-Cre* mice), to genetically target VG3-ACs (Grimes et al 2011, Kim et al 2015). Ai32 and Ai9 mice, which express channelrhodopsin-2 fused to yellow fluorescent protein (ChR2-YFP) and tdTomato in a Cre-dependent manner (Madisen et al 2012, Madisen et al 2010) were crossed to *VG3-Cre* mice for optogenetic stimulation (*VG3-ChR2* mice) and VG3-AC visualization in anatomical experiments (*VG3-tdT* mice), respectively. Mice in which the diphtheria toxin receptor (DTR) is expressed upon Cre-mediated recombination (Buch et al 2005) were used to remove VG3-ACs after circuit development (*VG3-DTR* mice). Diphtheria toxin (1 μg/50 g body weight) was injected intraperitoneally in *VG3-DTR* mice and Cre-negative or DTR-negative littermate controls (i.e. control mice), once a day every other day for a total of four injections starting at postnatal day 30. Mice were used approximately one week after the last injection. All procedures in this study were approved by the Animal Studies Committee of Washington University School of Medicine and performed in compliance with the National Institutes of Health *Guide for the Care and Use of Laboratory Animals.*

4.2.2 Electrophysiology

Patch clamp recordings of SbC-RGCs were obtained in retinal flat mount preparations. SbC-RGCs were identified based on contrast responses in loose-patch recordings, labeled by inclusion of Alexa 568 (1 mM) in the intracellular solution in subsequent whole-cell recordings, and visualized by 2-photon imaging at the end of each recording. During recordings, tissue was continually perfused (~8 mL/min) with warm (~33 °C) mouse artificial cerebrospinal fluid ($mACSF_{NaHCO3}$) containing (in mM): 125 NaCl, 2.5 KCl, 1 $MgCl_2$, 1.25 NaH_2PO_4, 2 $CaCl_2$, 20 glucose, 26 $NaHCO_3$ and 0.5 L-Glutamine equilibrated with 95% O_2 / 5% CO_2. In optogenetic experiments, L-AP4 (20 μM) and ACET (10 μM) were included in the $mACSF_{NaHCO3}$ to block transmission of photoreceptor signals to ON and OFF bipolar cells, respectively. Strychnine (1 μM) was added to $mACSF_{NaHCO3}$ to block glycinergic transmission. Current clamp recordings were performed with an intracellular solution containing (in mM): 125 K-gluconate, 10 NaCl, 1 $MgCl_2$, 10 EGTA, 5 HEPES, 5 ATP-Na and 0.1 GTP-Na (pH adjusted to 7.2 with KOH). The intracellular solution used in voltage clamp recordings contained (in mM): 120 Cs-gluconate, 1 $CaCl_2$, 1 $MgCl_2$, 10 Na-HEPES, 11 EGTA, 10 TEA-Cl and 2 Qx314 (pH adjusted to 7.2 with CsOH). Patch pipettes had resistances of 4 - 7 MΩ (borosilicate glass). All reported voltages were corrected for liquid junction potentials. For voltage-clamp recordings, series resistance (10 - 15 MΩ) was compensated electronically by ~ 75 %. Signals were amplified with a Multiclamp 700B amplifier (Molecular Devices), filtered at 3 kHz (8-pole Bessel low-pass) and sampled at 10 kHz (Digidata 1440A, Molecular Devices). Inhibitory and excitatory synaptic inputs to SbC-RGCs during photoreceptor-mediated light responses, were isolated by holding cells at the reversal potential of excitatory (0 mV) and inhibitory (-60mV) conductances, respectively. In current clamp recordings, no bias current was injected.

4.2.3 Light stimulation

To activate ChR2, light stimuli were presented through a 20 X 0.95 NA water immersion objective on the RGC-side of the retina. Light from a mercury bulb (Olympus) was bandpass filtered (426 – 446 nm, Chroma) and attenuated by neutral density filters (Chroma). We performed targeted recordings from VG3-ACs to choose an optogenetic stimulus intensity (3.15 * 10^{-4} W mm^{-2}, Figure S1) that matches photoreceptor-mediated light responses (Kim et al 2015). Stimulus timing was controlled by a Uniblitz shutter (Vincent Associates).

To characterize photoreceptor-mediated responses, light stimuli were presented on an organic light-emitting display (eMagin) focused on the photoreceptor-side of the retina via the substage condenser. Intensity of spots of varying size was square-wave-modulated at 0.25 Hz (average intensity: 1,500 rhodopsin isomerizations rod^{-1} s^{-1}; Michelson contrast: 100%). The order in which spots of different size were presented was randomly chosen for each cell. IPSC amplitudes were measured as baseline subtracted averages during 200 ms time windows. The duration of spike suppression was defined as the time following a stimulus during which the firing rate was below 50% of the average firing rate (Jacoby et al 2015).

4.2.4 Biolistics and imaging

Gold particles (1.6 μm diameter, BioRad) were coated with plasmids encoding cytosolic cyan fluorescent protein (CFP) and neuroligin 2 fused at its N-terminus to yellow fluorescent protein (YFP-NL2). Particles were delivered to RGCs from a helium-pressurized gun (BioRad) at approximately 40 psi (Kim et al 2015). After shooting, retinal flat mount preparations in $ACSF_{HEPES}$ - containing (in mM): 119 NaCl, 2.5 KCl, 2.5 $CaCl_2$, 1.3 $MgCl_2$, 1 NaH_2PO_4, 11 glucose and 20 HEPES (pH adjusted to 7.37 with NaOH) - were incubated in a humid oxygenated chamber at 33 – 35 ºC for 14 – 18 hrs. The tissue was then fixed for 30 min in 4%

paraformaldehyde in $mACSF_{HEPES}$ and washed PBS (3 x 10 min) before mounting and imaging. Confocal image stacks of biolistically labeled SbC-RGCs in *VG3-tdT* mice were acquired on Fv1000 laser scanning microscopes (Olympus) using a 60X 1.35 NA oil immersion objective. Synaptic connectivity was analyzed in image stacks with voxel size 0.103 μm (x/y-axis) – 0.3 μm (z-axis). Using local thresholding SbC-RGC dendrites, YFP-NL2 puncta and VG3-AC neurites were masked separately in Amira (FEI Company). Inhibitory synapses on SbC-RGCs formed by VG3-ACs were defined as YFP-NL2 clusters with a center of mass within 0.5 μm from a VG3-AC neurite. We confirmed that varying this distance from 0.25 – 1 μm did not qualitatively change the results. Given the size of synaptic puncta this range implies overlap or direct apposition of signals from YFP-NL2 and tdTomato in VG3-AC neurites. To compare the fraction of YFP-NL2 apposed by VG3-AC neurites to that caused by random signal overlap, the same analysis was repeated for each cell in image stacks in which the VG3-AC channel was rotated by 90° (i.e. switching x- and y-axes).

4.2.5 Statistics

Paired and unpaired *t* tests were used to assess the statistical significance of observed differences.

4.3 Results

To identify sources of inhibitory input to SbC-RCCs, we crossed mice expressing channelrhodopsin-2 fused to yellow fluorescent protein (ChR2-YFP, *ChR2* mice) in a Cre-dependent manner (Madisen et al 2012) to different driver lines, including *VG3-Cre* (Grimes et al 2011). Based on 2-photon guided recordings in *VG3-Cre ChR2* double transgenic mice (*VG3-ChR2* mice), we chose optogenetic stimulus parameters that match depolarizations of VG3-ACs

to their photoreceptor-mediated light responses (Figure 4.1). Optogenetic stimulation with these parameters elicited large postsynaptic currents in all (7/7) SbC-RGCs tested. These currents reverse at –68.7 ± 4.2 mV (Figures 4.2A – 4.2D), close to the expected reversal potential for chloride conductances (-60 mV) in our recording conditions, suggesting that VG3-ACs, which previously have been shown to provide excitatory input to several RGC types (Kim et al 2015, Krishnaswamy et al 2015, Lee et al 2014), provide inhibitory input to SbC-RGCs. The delay of ChR2-mediated inhibitory postsynaptic currents (IPSCs) is much shorter than that of photoreceptor-mediated IPSCs (Figure 4.3). Indeed, ChR2-mediated IPSCs in SbC-RGCs begin to rise < 2 ms after the voltage of VG3-ACs and peak before the voltage response (Figures 4.2E and 4.2F). The short delay of IPSCs and their persistence in the presence of AMPA and NMDA receptor blockers (Figure 4.3) rule out di-synaptic pathways driven by glutamate release from VG3-ACs as their source. ChR2-mediated IPSCs are abolished by application of strychnine (Figures 4.2G and 4.2H). Together, these results show that VG3-ACs provide direct glycinergic input to SbC-RGCs.

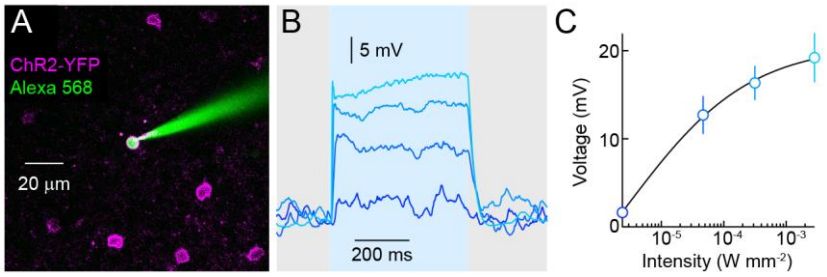

Figure 4.1 Optogenetic activation of VG3-ACs

(A) Representative 2-photon image of a VG3-AC targeted for patch clamp recording (Alexa 568 in *green*) in a *VG3-ChR2* (YFP fluorescence in *magenta*) retina. (B) Representative voltage responses of a VG3-AC stimulated with steps of blue light (426 – 446 nm, *shaded area*) of increasing intensity. (C) Summary data (mean ± SEM) of the intensity response function of optogenetic stimulation of VG3-ACs (n = 4).

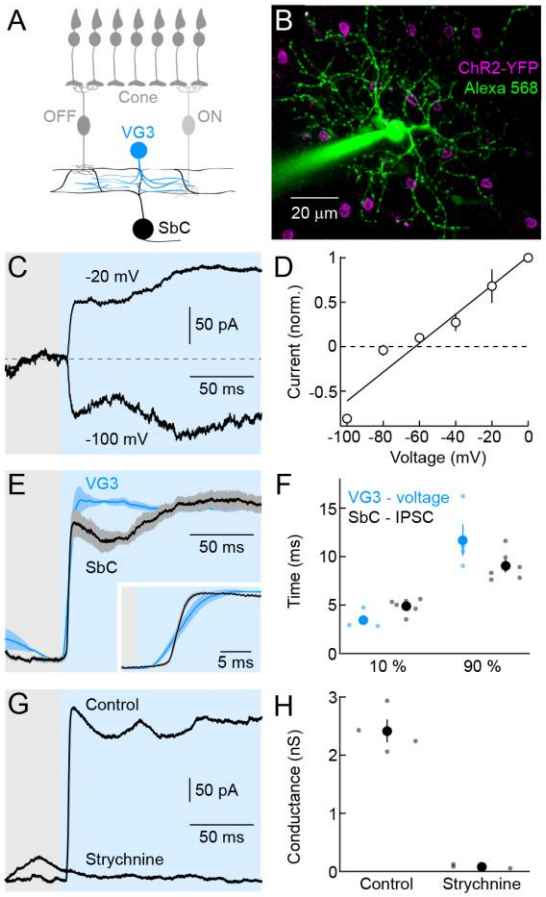

Figure 4.2 VG3-ACs provide direct glycinergic input to SbC-RGCs

(A) Schematic of the retina. Cone photoreceptors distribute signals to ON and OFF bipolar cells, which converge onto VG3-ACs. Neurites of VG3-ACs overlap with link processes between ON and OFF arbors of SbC-RGC dendrites. (B) Representative SbC-RGC recorded in a *VG3-ChR2* retina. The image is a z-axis projection of a 2-photon image stack. Whereas the Alexa 568 signal (*green*) was projected through the complete stack, projection of the YFP fluorescence (*magenta*) was restricted to the inner nuclear layer to highlight somata of VG3-ACs. (C, D) Representative traces (C) and summary data (D, mean ± SEM, n = 5) of currents recorded at different holding potentials in SbC-RGCs during optogenetic stimulation of VG3-ACs. (E) VG3-AC voltage (*blue*) and SbC-RGCs IPSC (*black*) responses to a bright step of blue light ($3.15 * 10^{-4}$ W mm^{-2}, 426 – 446 nm, *shaded area*). *Lines* (*shaded areas*) indicate normalized mean (± SEM) responses, facilitating comparisons of response timing. The *inset* shows responses at the stimulus onset on an expanded timescale. (F) Summary data of the time after stimulus onset before 10 % and 90 % of the peak amplitudes are reached (VG3-AC voltage, *blue*; SbC-RGC IPSC, *black*). *Dots* show data from individual cells (VG3-AC voltage, n = 4; SbC-RGC IPSC, n = 6) and *circles* (*errorbars*) indicate mean (± SEM) of the respective population ($p < 0.03$ for 10 %; $p > 0.1$ for 90 %). (G, H) Representative IPSC traces (G) and summary data of inhibitory conductances (H) of SbC-RGC elicited by optogenetic stimulation of VG3-ACs in absence or presence of strychnine. *Dots* represent data from individual cells (control, n = 4; strychnine, n = 3, $p < 0.001$) and *circles* (*errorbars*) indicate mean (± SEM) of the respective population.

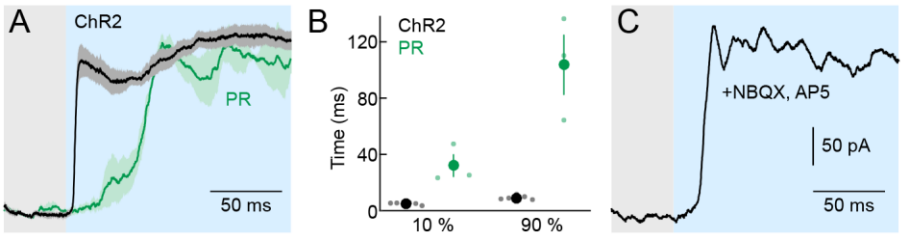

Figure 4.3 Kinetics and glutamate-blocker-resistance of optogenetic responses in SbC-RGCs

(A) Channelrhodpsin-2 (ChR2)-mediated (*black*) and photoreceptor-mediated (*green*) IPSCs in SbC-RGCs elicited by steps of blue light (3.15 $*10^{-4}$ W mm^{-2}, 426 – 446 nm, *shaded area*). *Lines* (*shaded areas*) indicate normalized mean (± SEM) responses, facilitating comparisons of response timing. (B) Summary data of the time after stimulus onset before 10 % and 90 % of the peak amplitudes are reached (ChR2-mediated, *black*; photoreceptor-mediated, *green*). *Dots* show data from individual cells (ChR2-mediated, n = 6; photoreceptor-mediated, n = 3) and *circles* (*errorbars*) indicate mean (± SEM) of the respective population ($p < 0.002$ and $p < 0.001$ for ChR2-mediated vs. photoreceptor-mediated responses to 10 % and 90 %, respectively). (C) Representative IPSC in and SbC-RGC elicited by optogenetic stimulation of VG3-ACs in the presence of NMDA (30 µM D-AP5) and AMPA (40 µM NBQX) receptor blockers. These blockers were added to inhibitors of metabotropic glutamate (20 µM L-AP4) and kainate receptors (10 µM ACET), which were used in all optogenetic experiments to block transmission of photoreceptor signals to bipolar cells.

SbC-RGCs are bistratified neurons whose ON and OFF dendrites are linked by numerous ascending and descending processes (Sivyer & Vaney 2010, Tien et al 2015). To determine the sites of inhibitory input from VG3-ACs, we biolistically labeled SbC-RGCs with cyan fluorescent protein (CFP) and YFP fused to neuroligin 2 (YFP-NL2), a selective marker of inhibitory synapses on RGC dendrites (Soto et al 2011), in mice that express tdTomato in VG3-ACs. The density of inhibitory synapses was highest on link processes between ON and OFF arbors (Figures 4.4A and 4.4B). A majority of these synapses were apposed by boutons of VG3-ACs, compared to a lower fraction of such appositions on ON and OFF dendrites (Figures 4.4C and 4.4D). Thus, VG3-ACs appear to provide glycinergic input to SbC-RGCs preferentially through synapses on link processes, a characteristic and conserved feature of SbC-RGC dendrites.

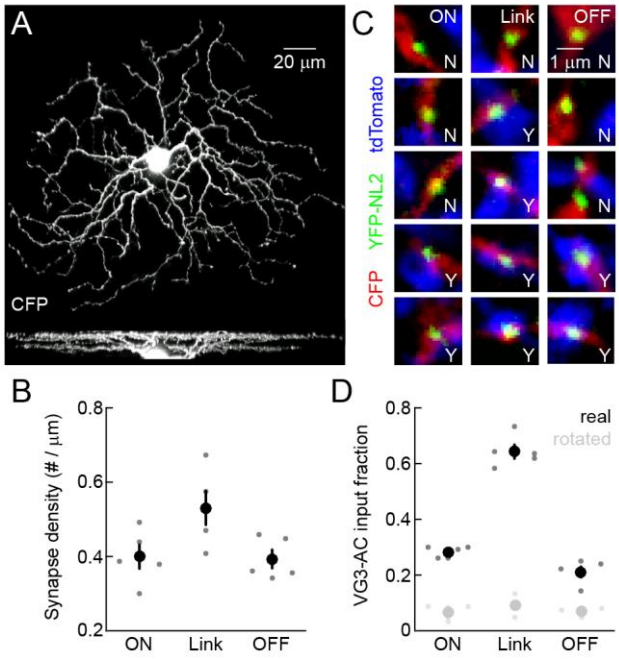

Figure 4.4 VG3-ACs form inhibitory synapses on link processes of SbC-RGC dendrites

(A) Z- (*top*) and y-axis (*bottom*) projections of a confocal image stack of a representative CFP-expressing SbC-RGC labeled by biolistics. (B) Summary data (n = 5) comparing inhibitory synapse density among ON dendrites, link processes and OFF dendrites ($p < 0.05$ for ON dendrites vs. link processes, $p < 0.03$ for OFF dendrites vs. link processes, and $p > 0.8$ for ON vs. OFF dendrites). Dots represent data from individual cells and *circles* (*errorbars*) indicate mean (± SEM) of the respective populations. (C) Excerpts of single image planes in the ON dendrite (*left column*), link process (*middle column*) of OFF dendrite (*right column*) portions of a confocal image stack of an SbC-RGC. SbC-RGC dendrites are labeled with CFP (*red*), inhibitory postsynaptic sites with YFP-NL2 (*green*), and VG3-AC neurites with tdTomato (*blue*, *VG3-tdT* retina). The presence and absence of VG3-AC boutons at inhibitory synapses on SbC-RGC dendrites is indicated by *Y* and *N*, respectively. (D) Summary data (n = 5) comparing the fraction of inhibitory synapses apposed by VG3-AC neurites among ON dendrites, link processes and OFF dendrites ($p < 10^{-6}$ for ON and OFF dendrites vs. link processes, $p < 0.001$ for ON vs. OFF dendrites). *Black dots* show data from individual cells and *black circles* (*errorbars*) represent mean (± SEM). For all processes (i.e. ON dendrites, link processes, and OFF dendrites), the fraction of synapses with appositions was lower ($p < 0.003$) when the VG3-AC signal was rotated by 90° (*gray dots* and *circles*), confirming the significance of this co-localization.

To elucidate the contribution of VG3-ACs to inhibition of SbC-RGCs during visual processing, we selectively removed VG3-ACs from mature circuits. Towards this end, we injected *VG3-DTR* and control mice intraperitoneally with diphtheria toxin starting at postnatal day 30 (s. *Experimental Procedures*) (Krishnaswamy et al 2015). VGluT3 staining showed that

the density of VG3-ACs was reduced by > 90 % one week after injections in *VG3-DTR* mice, but remained unchanged in littermate controls (Figures 4.5A and 4.5B) (Kim et al 2015). The density of other amacrine cells was unaffected in *VG3-DTR* mice (Figure 4.6), confirming the specificity of this manipulation. Comparing IPSCs elicited by contrast steps presented in spots of different size between *VG3-DTR* and control mice, we found that OFF but not ON inhibition to SbC-RGCs was reduced in a size-selective manner by removal of VG3-ACs (Figures 4.5C – 4.5F). Responses of VG3-ACs match the size selectivity of this deficit (Kim et al 2015). VG3-ACs respond more strongly to OFF than ON stimuli (Kim et al 2015). The preservation of ON inhibition in *VG3-DTR* mice suggests either that VG3-AC responses to ON stimuli fail to elicit glycine release or that other ON-responsive amacrine cells compensate for lost input from VG3-ACs (Jacoby et al 2015).

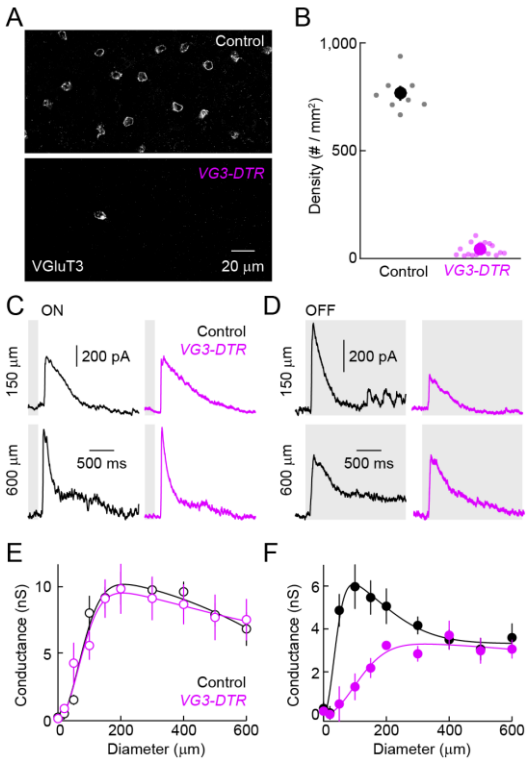

Figure 4.5 Genetic removal of VG3-ACs reduces inhibition of SbC-RGCs in a contrast- and size-selective manner

(A) Representative z-axis projections of confocal image stacks of retinal whole mounts stained for VGluT3 in control (*top*) and *VG3-DTR* mice (*bottom*) one week after diphtheria toxin injections. (B) Summary data of VG3-AC density in control (*black*) *VG3-DTR* (*purple*) retinas. *Dots* show data from individual retinas (control, n = 8; *VG3-DTR*, n = 18, $p < 10^{-20}$) and *circles* (*errorbars*) represent mean (± SEM). (C, D) Representative IPSCs in SbC-RGCs elicited by light increments (C, ON) and decrements (D, OFF) in small (150 μm diameter, *top*) or large (600 μm diameter, *bottom*) circles recorded in control (*left*, *black*) and *VG3-DTR* (*right*, *purple*) retinas. (E, F) Summary plots (mean ± SEM) comparing inhibitory synaptic conductances in SbC-RGCs of control (n = 5, *black*) and *VG3-DTR* (n = 4, *purple*) retinas elicited by ON (E) and OFF (F) stimuli of different sizes (i.e. circle diameters). Inhibitory conductances elicited by small and large ON stimuli are unaffected by deletion of VG3-ACs (e.g. $p > 0.7$ for control vs. *VG3-DTR* at 150 μm and 600 μm). Inhibitory conductances activated small ($p < 0.01$ for control vs. *VG3-DTR* at 150 μm) but not large ($p > 0.5$ for control vs. *VG3-DTR* at 600 μm) OFF stimuli are reduced by removal of VG3-ACs.

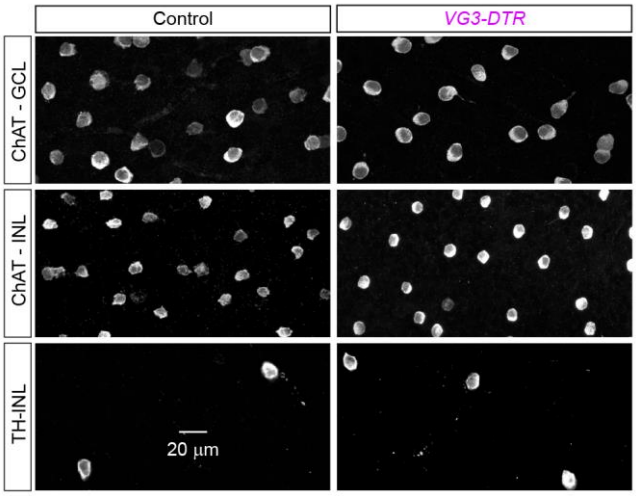

Figure 4.6 Selectivity of the genetic VG3-AC removal

Representative z-axis projections of confocal image stacks of control (*left column*) and *VG3-DTR* (*right column*) retinas stained for choline acetyltransferase (ChAT, *top* and *middle row*) and tyrosine hydroxylase (TH, *bottom row*). Projections were either restricted to the inner nuclear layer (INL, *middle* and *bottom row*) or the ganglion cell layer (GCL, *top row*). Images were taken one week after diphtheria toxin injections and show that the density of the respective amacrine cell types is unaffected by removal of VG3-ACs.

To determine how inhibitory input from VG3-ACs shapes spike responses of SbC-RGCs, we obtained current clamp recordings in *VG3-DTR* and control mice. Consistent with the reduced inhibitory input and reduced suppression of tonic excitation (Figure 4.7), spike suppression of SbC-RGCs by OFF stimuli was attenuated in a size-selective manner by removal

of VG3-ACs (Figures 4.8C and 4.8D). By contrast, suppression by ON stimuli was enhanced (Figures 4.8A and 4.8B). Voltage-clamp recordings revealed that this enhanced suppression is a result of a decrease in the ON-signed excitatory input to SbC-RGCs (Jacoby et al 2015, Tien et al 2015) in *VG3-DTR* compared to control mice (Figures 4.8E and 4.8F), suggesting presynaptic actions of VG3-ACs in this circuit.

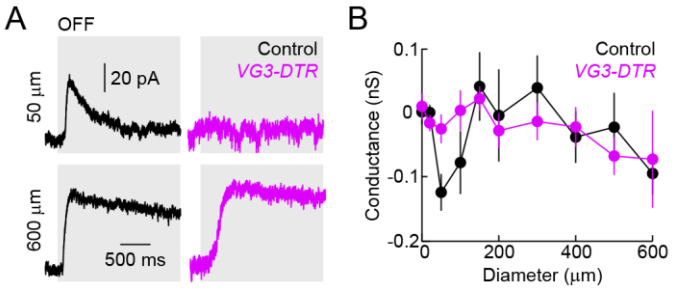

Figure 4.7 Genetic removal of VG3-ACs alters modulation of tonic excitatory input to SbC-RGCs by OFF stimuli in a size-selective manner

(A) Representative excitatory postsynaptic current traces of SbC-RGCs during presentation of light decrements (OFF) in small (50 µm diameter, *top*) and large (600 µm diameter, *bottom*) circles recorded in control (*left*, *black*) and *VG3-DTR* (*right*, *purple*) retinas. (B) Summary plots (mean ± SEM) of excitatory conductances of SbC-RGCs of control (n = 7, black) and *VG3-DTR* (n = 7, *purple*) retinas elicited by OFF stimuli of different sizes. In *VG3-DTR* mice, suppression of tonic excitation of SbC-RGCs by small OFF stimuli is reduced ($p < 0.02$ for control vs. *VG3-DTR* at 50 µm).

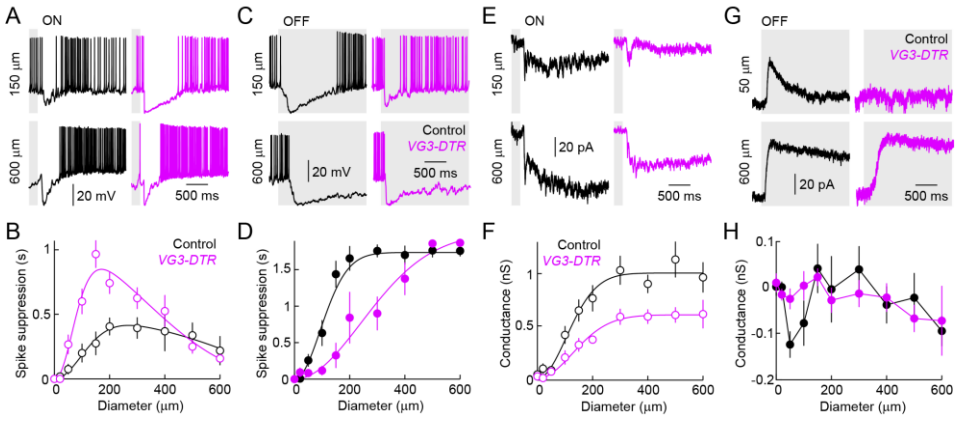

Figure 4.8 Genetic removal of VG3-ACs alters spike suppression and excitatory input of SbC-RGCs in a contrast- and size-selective manner

(A, C) Representative spike responses of SbC-RGCs to light increments (A, ON) and decrements (C, OFF) in small (150 μm diameter, *top*) and large (600 μm diameter, *bottom*) circles recorded in control (*left*, *black*) and *VG3-DTR* (*right*, *purple*) retinas. (B, D) Summary plots (mean ± SEM) comparing the duration of spike suppression of SbC-RGCs of control (n = 8, *black*) and *VG3-DTR* (n = 6, *purple*) retinas elicited by ON (B) and OFF (D) stimuli of different sizes. Spike suppression by small ON stimuli is enhanced ($p < 0.001$ for control vs. *VG3-DTR* at 150 μm) and spike suppression small OFF stimuli is reduced ($p < 0.001$ for control vs. *VG3-DTR* at 150 μm) by removal of VG3-ACs. By contrast, responses to large ON and OFF stimuli are unchanged ($p > 0.6$ and $p > 0.2$ for control vs. *VG3-DTR* for 600 μm ON and OFF stimuli, respectively). (E) Representative excitatory postsynaptic current traces elicited by small (150 μm diameter, *top*) and large (600 μm diameter, *bottom*) ON stimuli. (F) Summary data of excitatory conductances of SbC-RGCs in control (n = 7, black) and *VG3-DTR* (n = 7, *purple*) retinas activated by ON stimuli of different sizes. Excitatory input is reduced significantly for small ON stimuli ($p < 0.02$ for control vs. *VG3-DTR* at 150 μm).

4.4 Discussion

Here, we discover that VG3-ACs, which previously had been shown to provide glutamatergic input to four RGC types (Kim et al 2015, Krishnaswamy et al 2015, Lee et al 2014), provide glycinergic input to SbC-RGCs (Figure 4.2). Concurrent with our finding, another study came to the same conclusion (Lee et al 2016). In addition, we reconstruct circuits anatomically (Figure 4.4) and find that VG3-ACs form inhibitory synapses preferentially on ascending and descending processes that link the bistratified dendrites of SbC-RGCs. Finally, using cell-type-specific deletion in mature circuits, we show that VG3-ACs shape suppressive responses of SbC-RGCs in a contrast- and size-selective manner (Figures 4.5 and 4.8).

What mechanisms underlie the target specificity of excitatory and inhibitory neurotransmission from VG3-ACs? Glutamate and glycine could be co-released at the same synapses with specificity arising from postsynaptic receptor expression and/or localization, or they could be released selectively at synapses with different targets. In striatum, glutamate and acetylcholine are packaged into the same vesicles by synergistic action of VGluT3 and the vesicular acetylcholine transporter (VAChT) (Gras et al 2008); GABA and glycine share a

vesicular transporter (VIAAT) and are co-released in the spinal cord (Jonas et al 1998, Wojcik et al 2006); and GABA was recently shown to use the vesicular monoamine transporter (VMAT) to co-release with dopamine in striatum (Tritsch et al 2012). In each of these cases, both transmitters elicit signals in each postsynaptic target cell. In other neurons, including starburst amacrine cells (Lee et al 2010, Wei et al 2011, Yonehara et al 2011), dual transmitters are released from separate vesicle pools, which can segregate into different axon terminals (Chuhma et al 2014, Gagnon & Parent 2014, Onoa et al 2010). The distribution of VGluT3 is homogenous along VG3-AC neurites; and VIAAT, the vesicular transporter for glycine, appears not to be expressed by VG3-ACs (Haverkamp & Wassle 2004, Johnson et al 2004). Whether the selectivity of excitatory and inhibitory neurotransmission between VG3-ACs and RGC targets arises pre- or postsynaptic, and whether release of glycine involves mechanisms other than vesicle fusion (Rosenberg et al 2013), thus remains to be determined.

The observation that VG3-ACs use glutamate to excite neurons activated by contrast and motion, and glycine to inhibit neurons suppressed by contrast and motion illustrates how modular output signals can enhance the circuit function of a neuron. Similar modular organization is found in the input to SbC-RGCs. Inhibition from Crh1-ACs, AII-ACs, VG3-ACs and at least one more OFF-responsive amacrine cell combine to suppress tonic firing of SbC-RGCs (Figures 4.5 and 4.8) (Jacoby et al 2015, Tien et al 2015). Each convergent input contributes a distinct component of inhibition based on its preferential responses to ON or OFF, and small or large stimuli. Convergence modularity is also a feature of inhibitory input to direction selective ganglion cells (Hoggarth et al 2015), and may be a general organizing principle of inhibitory circuits in the retina.

The numerous ascending and descending processes between ON and OFF dendrites are a characteristic feature of SbC-RGCs (Sivyer & Vaney 2010, Tien et al 2015). Here, we find that these link processes are the primary site of synaptic input from VG3-ACs (Figure 4.4), whose neurites stratify between ON and OFF arbors of SbC-RGCs. SbC-RGC link processes and the lamination of VG3-ACs are conserved from rodents to primates (Haverkamp & Wassle 2004, Sivyer & Vaney 2010, Tien et al 2015), suggesting that their connectivity patterns are as well. In this unusual anatomical arrangement, VG3-ACs use their inhibitory transmitter in a target-specific manner to shape suppressive contrast responses of SbC-RGCs.

Chapter 5 : Development and Mature Patterns of Axonal Projections of Suppressed-by-Contrast Retinal Ganglion Cells

To process light information from the environment and drive appropriate visual behaviors, it is critical that retinal ganglion cell (RGC) types send signals to specific brain regions. Despite progress in identifying RGC types, the central projections of individual RGC types, and their contribution to visual processing and behaviors remain mostly unknown. Here, we used an intersectional transgenic strategy to label one unique RGC type that shows spike suppression in response to contrast (SbC-RGCs) in mice, and identified their projection targets. We found that SbC-RGCs project to the dorsal lateral geniculate nucleus (dLGN) and the superior colliculus (SC), the two major retinorecipient nuclei in image-forming visual circuits. SbC-RGCs also heavily innervate the ventral lateral geniculate nucleus (vLGN) but avoid the adjacent intergeniculate leaflet (IGL), nuclei that are thought to have similar non-image-forming functions. Time-course examination revealed that the innervation of SbC-RGC axons is highly accurate across development. Together, these findings facilitate future studies of the functional role of SbC-RGCs and of the mechanisms underlying axonal target selection.

5.1 Introduction

Different aspects of visual features are encoded in spike trains of distinct RGC types, which send axonal projections to diverse subcortical targets (Berson 2008, Dhande & Huberman 2014). In mice, 46 retinorecipient areas have been identified, serving various visual functions (Morin &

Studholme 2014). However, while recent studies in mice have made significant progress in cataloging RGC types, the projection patterns and visual functions of most RGC types remain unknown. This is due mainly to lack of transgenic lines that selectively label individual RGCs types (Baden et al 2016, Dhande & Huberman 2014).

Classically, visual functions of RGC projecting targets can be broadly separated into "image-forming" versus "non-image-forming" circuits, depending on whether they are involved in image representations directly (Cooper et al 1993, Pickard 1985). Much attention has been focused on retinorecipient targets in image-forming pathways. For example, the dLGN and the SC, two major subcortical nuclei sending visual information to the primary visual cortex directly and indirectly, receive ~30-40% and 85-90% of RGC projections in rodents, respectively (Martin 1986, Pickard 1985, Roth et al 2016, Sparks 1986, Wei et al 2015). Several studies of individual mouse strains revealed distinct laminar innervation patterns in the dLGN or/and the SC for each RGC type (Huberman et al 2008, Kim et al 2010, Rivlin-Etzion et al 2011). A growing numbers of non-image-forming circuits serving a variety of functions have also been mapped: direction-selective RGCs (DSGCs) to the accessory optic system (AOS) for reflexive eye movements to stabilizing images on the retina, and intrinsically photosensitive RGCs (ipRGCs) to the suprachiasmatic nucleus (SCN), the vLGN and the IGL for circadian rhythm entrainment (Berson et al 2002, Dhande et al 2013, Ecker et al 2010, Harrington 1997, Osterhout et al 2011, Oyster et al 1980). Intriguingly, compared to the well-studied neighboring thalamic nucleus the dLGN, little is known about the RGC types projecting to the vLGN and IGL other than ipRGCs (Hannibal & Fahrenkrug 2004, Hattar et al 2006, Hattar et al 2002, Monavarfeshani et al 2017).

Previously, we identified a unique mouse RGC type (SbC-RGCs) that decreases rather than increases firing rates in response to light increments and decrements (Tien et al 2015).

While the presence of SbC-RGCs in other species suggests they are a conserved RGC type, and matching suppressive responses have been recorded in several brain targets, a map of SbC-RGC projections to the brain is still missing (de Monasterio 1978, Ito et al 2017, Levick 1967, Piscopo et al 2013, Rodieck 1967, Sivyer et al 2010, Sumitomo et al 1979).

In this study, we label SbC-RGCs by an intersectional transgenic approach, and identified their axonal projections. Both subcortical regions known for image-forming processing, the dLGN and the SC, are innervated by SbC-RGCs. Surprisingly, the vLGN, but not IGL, are heavily innervated by SbC-RGCs, although both nuclei are thought to play similar roles in non-image-forming visual functions. Investigation of target innervation at different time points revealed the high accuracy of SbC-RGCs' axon target selection compared to other known RGC types with early-arriving axons. Together, these results provided useful clues for further probing the functional roles of SbC-RGCs.

5.2 Materials and Methods

5.2.1 Mice

Throughout this study, we used *Cck-ires-Cre* mice (Taniguchi et al 2011) (Jackson Laboratories) crossed to the mouse lines carrying *Brn3c*^{CKOAP} obtained from Badea Lab (Badea & Nathans 2011). All procedures were approved by the Animal Studies Committee of Washington University School of Medicine and performed in compliance with the National Institutes of Health Guide for the Care and Use of Laboratory Animals.

5.2.2 Histology

Retinas and brain slices were collected, stained and processed as previously described (Badea et al 2003, Johnson et al 2018). Briefly, mice were euthanized with CO_2 followed by decapitation

and enucleation. Eyes were transferred into oxygenated mouse artificial cerebrospinal fluid ($mACSF_{HEPES}$) containing (in mM): 119 NaCl, 2.5 KCl, 1 NaH_2PO_4, 2.5 $CaCl_2$, 1.3 $MgCl_2$, 20 HEPES, and 11 glucose (pH adjusted to 7.35 using NaOH). Retinas were either isolated and mounted flat on filter paper, or left in the eyecup for 25 min fixation with 4% paraformaldehyde in $mACSF_{HEPES}$. Meanwhile, mouse brains were removed and placed in 4% paraformaldehyde in PBS overnight in 4 ˚C. Next day, brains were wished with PBS, embedded in 4% low melting point agarose in PBS, and sectioned at 80-100 µm thickness. Retina whole mounts, eyecups and brain slices were heat-inactivated in PBS in a water bath for 1.5-2 hrs at 65-70 ˚C. Retina eyecups were embedded in 4% low melting point agarose in PBS, and sectioned at 60 µm thickness. AP staining was performed in 0.1 M Tris, 0.1 M NaCl, 50 mM $MgCl_2$, pH 9.5, 0.375 mg/ml of nitroblue tetrazolium (NBT) and 0.188 mg/ml 5-bromo-4-chloro-3-indolyl-phosphate (BCIP) (Sigma-Aldrich), for 2 hrs at room temperature to overnight at 4 ˚C with constant shaking. After staining, tissues were washed in PBS with 0.1 % Tween 20 three times, each 20 min, and postfixed with 4% paraformaldehyde in PBS overnight in 4 ˚C. For most of the representative figures, samples were dehydrated in an ethanol series (50 %, 75 %, 85 %, 95 %, 100 proof, each 20 minutes and 200 proof overnight in 4 ˚C). The following day, tissues were cleared with 2:1 bezyl benzoate/benzyl alcohol for imaging.

5.2.3 Enucleations

All enucleation procedures were conducted in mice older than 3 weeks. Mice were anesthetized intraperitoneally with ketamine (1 mg/10 g) and xylazine (1 mg/ 100 mg). The eye was gently lifted away from the orbit with forceps and freed from the optic nerve using surgical scissors. A small piece of gel foam (Vetspon, Novartis) was inserted in the orbit to stop bleeding using sterile forceps. The eyelid was sealed using tissue adhesive (Vetbond, 3M). Animals were

monitored for the following days for sign of infection, and euthanized for processed 3 weeks after enucleation.

5.2.4 Microscopy and Image Analysis

Tissue stained for AP was imaged on a bright-field microscope (Olympus BX51) using a 4 × 0.16 NA, 10 × 0.40 NA, or 20 × 0.70 NA air objective. The boundaries of retinorecipient targets were identified and determined by landmarks, and compared to mouse atlas (Franklin & Paxinos 2012, Godement et al 1984, Oh et al 2014). Images were analyzed in Fiji (Osterhout et al 2014, Schindelin et al 2012). For dLGN refinement measurement, the "line measurement" tool was used to determine the maximum distance innervated by RGC axons across the width of the dLGN, and three measurements (dorsal, middle, and ventral) per section were analyzed as described previously (Osterhout et al 2014). Three to five slices from each mouse with the largest dLGN areas were analyzed, depending on the mouse age (Diao et al 2017, Osterhout et al 2014).

5.3 Results

5.3.1 An Intersectional Transgenic Strategy to Preferentially Label SbC-RGCs

In previous studies, we identified SbC-RGCs using *Cck-ires-Cre Ai9* mice, which were known to label several other RGC types and amacrine cells (Fig. 5.1) (Tien et al 2015, Zhu et al 2014). To map the downstream retinorecipient zones receiving inputs from SbC-RGCs, we wanted to generate mice lines in which SbC-RGCs are more selectively labeled. The morphological studies in *Brn3c*$^{AP/+}$ expressing RGCs showed that one RGC type exhibited morphological features of SbC-RGCs: bistratified dendrites with descending processes from the OFF layer (Badea &

Nathans 2011, Tien et al 2015). Thus we crossed *Cck-ires-Cre* mice with *Brn3c*^{CKOAP} mice to see whether this intersectional approach would allow us to target SbC-RGCs more specifically (Badea & Nathans 2011). In cells expressing both *Cck-ires-Cre* and *Brn3c*, Cre-mediated recombination will result in human placental alkaline phosphatase (AP) expression under the control of the *Brn3c* promoter (Badea et al 2009, Badea & Nathans 2011). AP staining was performed in retinas from *Cck-ires-Cre; Brn3c*^{CKOAP} double positive mice (*CCK-Brn3c*$^{AP/+}$) (Figure 5.2A-5.2C). The AP^{+} RGCs distribute in a mosaic-like pattern throughout *CCK-Brn3c*$^{AP/+}$ retinas, suggesting that the AP^{+} RGCs primarily consist of a homogeneous cell type (Fig. 5.2A and Fig. 5.2C, compared to Fig. 5.1). Moreover, the majority of AP^{+} RGCs are bistratified with diving dendrites reminiscent of SbC-RGCs (Fig. 5.2B). A small fraction of labeled cells (~6-10 %) were monostratified resembled the other *Brn3c*$^{AP/+}$-expressing RGC types described previously (Badea & Nathans 2011, Rousso et al 2016). Because this low percentage does not represent the whole population of mono-stratified *Brn3c*$^{AP/+}$ expressing RGCs, their labeling could result from leaky expression of Cre, or indeed only partial of monostratified *Brn3c*$^{AP/+}$ expressing RGCs express both *Cck-ires-Cre* and *Brn3c*. Collectively, these observations suggest that SbC-RGCs are preferentially labeled in *CCK-Brn3c*$^{AP/+}$ mice.

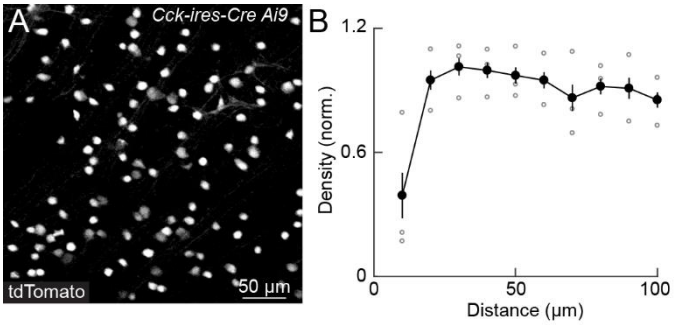

Figure 5.1 Distribution of tdTomato-expressing cells in *Cck-ires-Cre Ai9* mice

(A) Confocal image of tdTomato-expressing cells in the ganglion cell layer (GCL) of a whole-mount *Cck-ires-Cre Ai9* retina. (B) Density recovery profiles of tdTomato-expressing cells in the GCL.

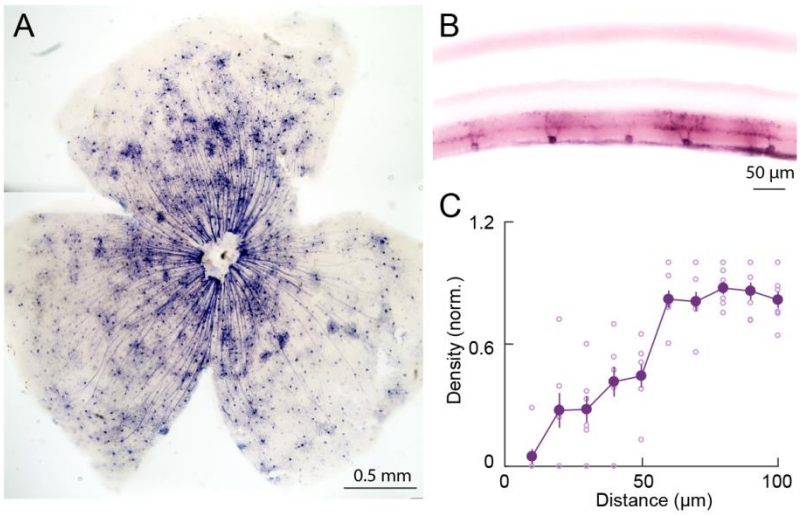

Figure 5.2 An intersectional strategy to label SbC-RGCs in the mouse retina

(A) Flat mount and (B) vibrotome section of retinas from *CCK-Brn3c*$^{AP/+}$ mice showing SbC-RGCs were preferentially stained for AP activity. (C) Population data of density recovery profiles of AP^{+} labeled RGCs (6 ROIs from 2 retinas) show a mosaic arrangement with characteristic exclusion zones.

5.3.2 SbC-RGCs Project to Both Image-Forming and Non-Image-Forming Brain Areas

To determine the brain areas that SbC-RGCs send the visual information to, we developed AP staining in brain slices from *CCK-Brn3c*$^{AP/+}$ mice. AP^{+} neurites were observed in optic nerve and several central visual nuclei, without significant difference between *Cck-Brn3c*$^{AP/+}$ mice and *Brn3c* knockout mice (*CCK-Brn3c*$^{AP/AP}$) (Fig. 5.3A-5.3C, Fig. 5.4). Since AP was also expressed in neurons in the deeper layer of the SC, we first needed to confirm that those AP^{+} neurites observed in visual nuclei are retinofugal fibers. We thus examined brain slices from *CCK-Brn3c*$^{AP/+}$ mice with either left or right eyes removed (Fig. 5.3D-5.3G). The arbors from nonretinal source will not be affected by enucleation; however, for AP^{+} neurites coming from

RGCs axons, single eye enucleation would result in significant decrease in arbor innervation in the contralateral sides with ipsilateral sides mostly unaffected in the visual nuclei we observed (Seabrook et al 2017). Indeed, we found that in the contralateral areas receiving inputs from the removed retina, AP signals were gone; by contrast, the signals in ipsilateral regions receiving inputs from the remained retina persisted (Fig. 5.3D-5.3G). Therefore, the AP^+ neurites in those visual nuclei are from AP^+ RGCs, which mostly represent SbC-RGCs.

Labeled SbC-RGC fibers project to the SC and dLGN, the two major retinorecipient zones in image-forming visual circuits (Fig. 5.3A and 5.3B). Unlike the few known RGC types showing confined arbors in a narrow sublamina, AP^+ arbors in the SC expand almost throughout the whole stratum griseum superficiale layer (SGS) as well as the thin top layer stratum zonale (Fig. 5.3A) (Kim et al 2010). The innervation in the dLGN also revealed a laminar pattern different from the known RGC types, covering ~2/3 of dLGN from the optic tract to the medial border (Fig. 5.3B). Although the dense labeling made it challenging to distinguish the arborization patterns between SbC-RGCs and the other 6-10 % monostratified RGCs, because AP^+ neurites cover the whole retinotopic map of both the SC and the dLGN consistently across animals, we concluded that SbC-RGCs project to these two subcortical nuclei.

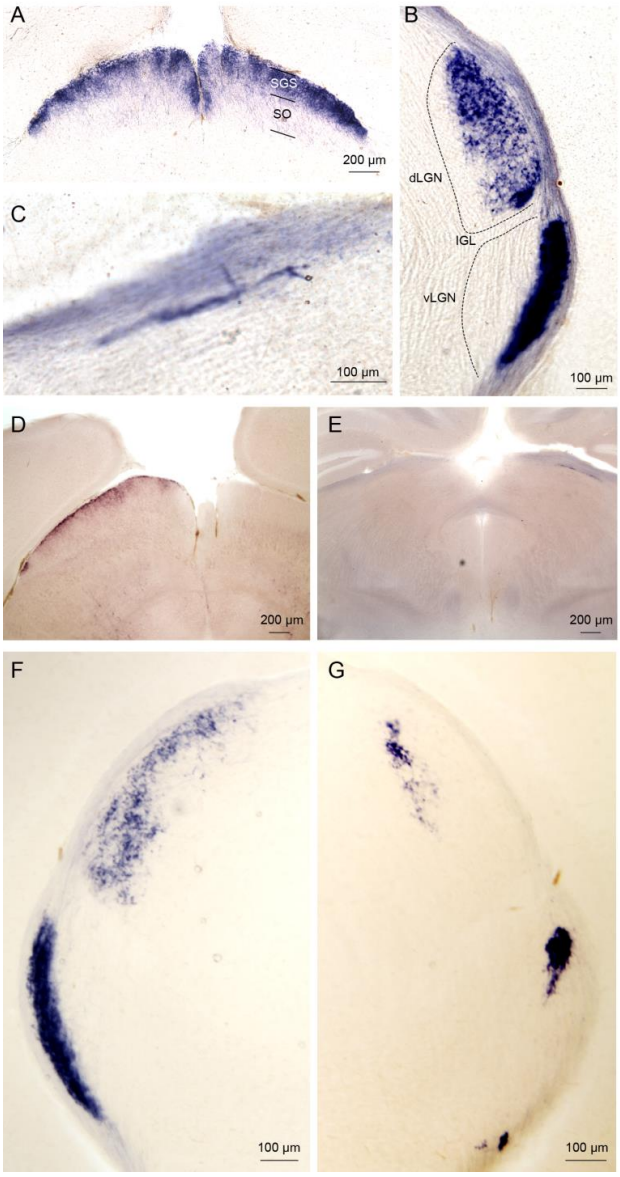

Figure 5.3 Brain projections from SbC-RGCs

(A)-(C) Coronal brain sections from *CCK-Brn3c*$^{AP/+}$ adult mice (>P30) reveal central projections in the SC (A), dLGN and vLGN (B), and the NOT (C) of *CckCre-Brn3c*-expressing RGCs histochemically stained for AP. (D)-(G) The projections contralateral to the removed eye were significantly reduced, confirming RGCs are the source of AP^{+} axons in those regions. (D), (F) and (G) The left-eye enucleation resulted in devoid of AP signals in the contralateral side (right side) of the SC (D) and of the thalamic nuclei (G), whereas the ipsilateral side (left side) of the SC (D) and of the thalamic nuclei (F) projections were mainly preserved. (E) Right eye removal resulted in the loss of AP signals in the contralateral side (left side) of the NOT. SGS, the stratum griseum superficiale; SO, the stratum opticum; dLGN and vLGN, dorsal and ventral lateral geniculate nucleus; NOT, the nucleus of the optic tract.

Intriguingly, AP^+ signals in nuclei involved in non-image-forming visual circuits were also observed (Fig. 5.3B and 5.3C). The vLGN shows dense AP^+ labeling throughout the whole nucleus (Fig. 5.3B). However, the adjacent IGL, which shares many projections and physiological properties with the vLGN, is devoid of AP^+ signals (Fig. 5.3B). Also, few AP^+ axons terminate in the nucleus of the optic tract (NOT), one major component of the AOS mediating the optokinetic reflex (Fig. 5.3C). Compared to the dense innervation in the NOT by RGCs labeled with CTB eye injection or transgenic lines in previous studies, these sparse AP^+ signals in the NOT suggest either those axons come from the 6-10 % mono-stratified RGCs, or SbC-RGCs are comprised of subtypes, with only few projecting to the NOT(Dhande et al 2013). In sum, in addition to projecting to image-forming visual subcortical areas (the dLGN and the SC), SbC-RGCs also send retinal information to the vLGN, with the source of AP^+ axons in the NOT indiscernible.

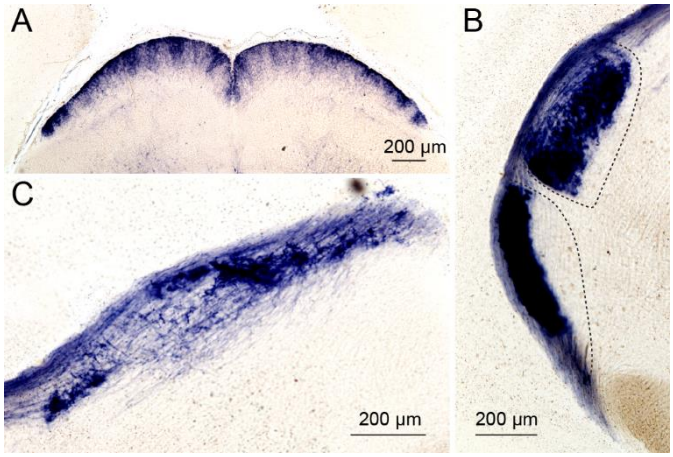

Figure 5.4 Central projections in *CCK-Brn3c*$^{AP/AP}$ mice

(A)-(C) The innervation patterns of *CckCre-Brn3c*-expressing RGCs in *Brn3c* knock out mice (*CCK-Brn3c*$^{AP/AP}$) are indistinguishable from the innervation patterns of *CCK-Brn3c*$^{AP/+}$ mice.

5.3.3 SbC-RGCs Innervation is Highly Accurate across Development

Previously, the developmental studies of RGC labeled in transgenic lines suggest a correlation between the time of axon arrival and the number of transient, incorrect target innervation (Osterhout et al 2014). That is, early-arriving RGC axons initially tend to make mistakes in target selection, and then the projections in wrong places will be removed later in the development. Moreover, the timing of innervation is nuclei-specific in spite of the same RGC axon (McNeill et al 2011, Osterhout et al 2014). Therefore, the SbC-RGC projections in different visual nuclei were examined at different developmental stages to see whether SbC-RGCs also exploit the same strategy that early arrival axons innervate more incorrect targets, and that the timing of multiple target innervation is regulated differentially.

AP^+ axons have already arrived in their targets by postnatal day 0 (P0), including the most distal retinorecipient nucleus, the SC (Fig. 5.5A and 5.5F). However, axon arborizations were only observed in the dLGN and the vLGN at P0 (Fig. 5.5F). The axons in the NOT and the SC have not branch at this time point (Fig. 5.5A and data not shown). From the sagittal section, it is clear that the majority of AP^+ axons in the superficial layer of the SC came from optic tract and not from AP+ labeled cells in the deep layer of the SC (Fig. 5.6). Axon arborizations in the SC and the NOT were detected at P5, and the innervation of thalamic nuclei and the SC increases subsequently, reaching mature patterns between P10 and P15 (Fig. 5.5B-5.5E and 5.5G-5.5J). The development of NOT innervation was variable (Fig. 5.5L-5.5O). Despite of the dense labeling in the SC and the thalamic nuclei precluding detailed analysis of individual arborization patterns, occasionally two types of RGC arbor patterns were observed in the SC due to heterogeneous expression levels of AP (Fig. 5.5D). One type elaborates in the upper stratum griseum superficialls (uSGS) while the other innervates the lower SGC (lSGS). Single cell

labeling would be required to determine whether they are SbC-RGC axons in different developmental state or from different RGC types. Most importantly, mistargeting into other retinorecipient zones were not been observed between P0 and P20, indicating that the innervation of early-arriving SbC-RGC axons is accurate, starting from the dLGN and the vLGN, followed by the SC innervation.

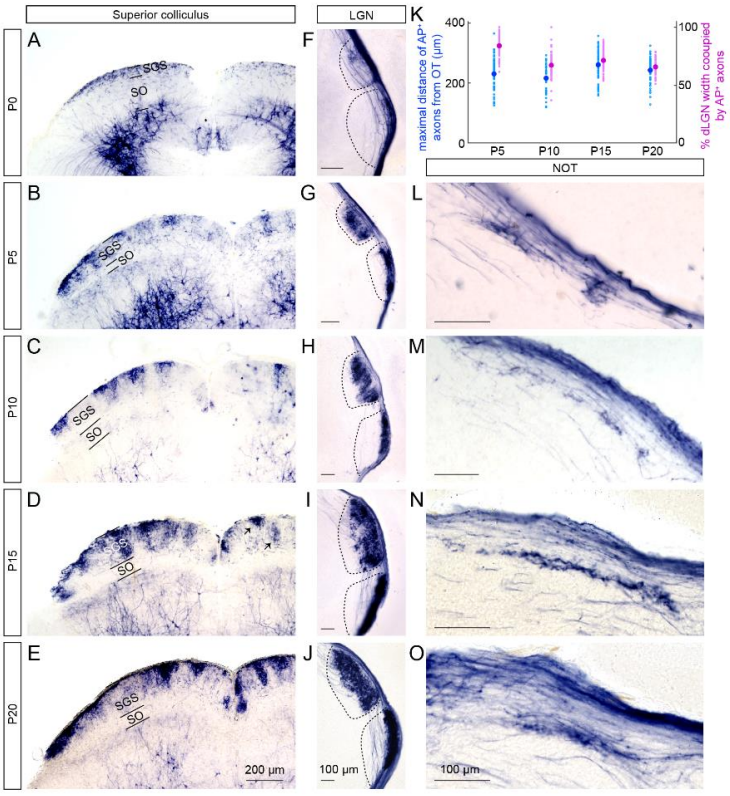

Figure 5.5 Accurate regulation of axon target matching of *CckCre-Brn3c*-expressing RGCs

(A)-(E) SbC-RGC axons innervating in the SC at P0 (A), P5 (B), P10 (C), P15 (D) and P20 (E). Arrows in (D), AP^+ axons innervating at different sublaminae of the SC. (F)-(J) SbC-RGCs projections in the dLGN and vLGN at P0 (F), P5 (G), P10 (H), P15 (I), and P20 (J). (K), SbC-RGC axon innervation in the dLGN at different developmental time points. Blue dots, maximum distance of AP^+ axons from the optic tract (OT). Purple dots, percentage of total width of the dLGN occupied by AP^+ axons. One-way ANOVA with Tukey's multiple comparison was performed. For maximum distance, *P5* vs *P15* $p < 0.001$; *P10* vs *P15* $p < 0.001$; *P10* vs *P20* $p < 0.05$. For the percentage of total width, *P5* vs *P10* $p < 0.001$; *P5* vs *P15* $p < 0.001$; *P5* vs *P20* $p < 0.001$; *P15* vs *P20* $p < 0.01$. (L)-(O), Innervation of the NOT by *CckCre-Brn3c*-expressing RGCs at P5 (L), P10 (M), P15 (N) and P20 (O). SGS, the stratum griseum superficiale; SO,

the stratum opticum; dLGN and vLGN, dorsal and ventral lateral geniculate nucleus; NOT, the nucleus of the optic tract.

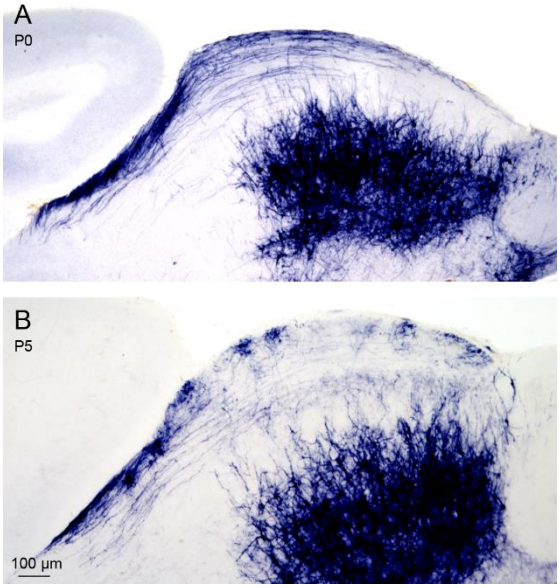

Figure 5.6 Sagittal view of AP^{+} axons in the SC in *CCK-Brn3c$^{AP/AP}$* pups

(A)-(B) The AP+ axons observed in the SC originate from optic tract rather than neurons in the deeper layer of the SC. Also, the axons initially observed in the SGS layer at P0 (A) retract within the SO layer by P5 (B), which is consistent with previous findings (Sachs et al 1986). SGS, the stratum griseum superficiale; SO, the stratum opticum.

Detailed examination of dLGN innervation also revealed that initially SbC-RGC axons reach to almost the medial boundary of the nucleus at P5, but the ratio of dLGN width occupied significantly decreased to the mature ratio at P10 (Fig. 5.5G-K). The decreased ratio cannot be accounted for by retraction of overshot axons; in fact, the maximal distance of SbC-RGC axons slightly increases between P5 and P15. This means after the initial rapid growing phase by P5, SbC-RGC axon growth slows down while the dLGN expands significantly.

5.4 Discussion

Here, we used an intersectional transgenic approach (*Cck-ires-Cre* and *Brn3c*) to preferentially label SbC-RGCs, one unique RGC type previously found in mice, rabbits, cats and primates (de Monasterio 1978, Levick 1967, Rodieck 1967, Sivyer et al 2010, Tien et al 2015). This allowed us to determine that SbC-RGCs send their suppressed-by-contrast signals to both image-forming and non-image-forming visual circuits, including the SC, the dLGN and the vLGN. Additionally, the axon innervation of SbC-RGCs is nuclei-specific (first in the dLGN and the vLGN) and accurate across development.

The occasional observation (~6-10 %) of non-SbC-RGCs casts doubts on whether the innervation patterns truly reflect SbC-RGC's projections. We believe SbC-RGCs do project to the dLGN, the vLGN and the SC from following reasons. First, the AP^+ axons consistently innervate throughout the whole retinotopic map of these three nuclei as we examined all the brain sections. It is unlikely that the 6-10 % labeling is able to cover the whole visual space. Secondly, the 6-10% mono-stratified *Brn3c*$^+$ RGCs is likely the *Brn3c*$^+$ cells reported in another transgenic line, *Foxp2*^{Cre}*-GFP*, which also labels other three distinct RGC types (Rousso et al 2016). However, the thalamic nuclei innervation by GFP^+ axons in *Foxp2*^{Cre}*-GFP* mice is very different from what we observed in *CCK-Brn3c*$^{AP/+}$ mice: only the "shell" of the dLGN is innervated by *Foxp2Cre-GFP* labeled RGCs, with vGLN GFP signals barely detected. Even if the *Brn3c*$^+$ monostratified RGCs (but not the other three RGC types) contribute to all the thalamic nuclei innervation in *Foxp2Cre-GFP* mice, which is an extreme case, it can not explain the AP^+ axons in the "core" of the dLGN and the dense labeling in vLGN we observed in *CCK-Brn3c*$^{AP/+}$ mice. In other words, the AP^+ axons innervating in the dLGN and vLGN are likely from the SbC-RGCs. For the SC, although the innervation was observed in both *Foxp2*^{Cre}*-GFP*

mice and *CCK-Brn3c*$^{AP/+}$ mice, given that 85-90% of the mouse RGCs project to the SC, it is very possible that both SbC-RGCs and the 6-10% labeled mono-stratified RGCs send axons to the SC. It is worth noting that occasionally we found axons elaborating in different sublamina in the SC (Fig. 5.5D), suggesting projections from two RGC types or innervation at different developmental states. The layer-specific innervation is an important feature because it has been suggested that deeper collicular layers may contain coarser visual information (Kim et al 2010). Single cell labeling via tamoxifen-inducible CreER mediated *Brn3c* expression (e.g., *R26CreER* or *CCK-CreER* crossed with *Brn3c*^{CKOAP} mice) would be helpful in distinguishing innervation patterns from different RGC types, if any. Intriguingly, GFP$^+$ signals in the NOT were not detected in the *Foxp2*^{Cre}*-GFP* mice, suggesting AP$^+$ axons in the NOT may come from SbC-RGCs; alternatively, only few Brn3$^+$ mono-stratified RGCs project to the NOT, and their GFP signals in the *Foxp2*^{Cre}*-GFP* are too dim to be reliably detected. Again, single cell labeling would address this question. Taken together, we conclude that SbC-RGCs project to the SC, the dLGN and the vLGN, with the NOT innervation remaining somewhat uncertain. Future experiments including direct brain imaging of RGC axonal terminals as well as brain injections to retrogradely label RGCs projecting to those subcortical regions will further confirm these SbC-RGCs-to-brain connections.

The finding that SbC-RGCs project to the vLGN, but not the adjacent IGL is interesting. The IGL/vLGN have long been thought to play a role in circadian rhythm regulation based on anatomical and functional evidence (Harrington 1997). Anatomically, some ipRGCs projecting to the SCN, the circadian clock in the brain, also project to the IGL/vLGN (Ecker et al 2010, Hattar et al 2006). In addition, many cells in the IGL (few in the vLGN for cats and hamsters) were found to project to the SCN (Harrington 1997, Harrington et al 1987, Morin 2013, Pu &

Pickard 1996). Functionally, light exposure and conditioned stimuli able to entrain circadian rhythms had been shown to increase cFos-immunoreactivity in the IGL/vLGN (Amir & Stewart 1996, Harrington 1997, Park et al 1993). However, results from IGL/vLGN lesions are ambiguous to interpret the visual function of IGL/vLGN, mainly due to the unintentional damage to the optic tract and the adjacent dLGN. The observation that SbC-RGCs' innervation in the vLGN but not IGL suggests a potentially different role of the vLGN from the IGL. The effect of pharmacogenetic or optogenetic silencing SbC-RGC signals in vLGN on visual responses may be helpful in identifying additional visual functions of vLGN (Burgess et al 2017, Huberman & Niell 2011, Zmarz & Keller 2016).

In contrast to the RGC types studied so far, the early-arriving SbC-RGC axons innervate correct targets accurately without making developmental mistakes (Fig. 5.5) (Osterhout et al 2014). SbC-RGCs innervation may serve a role in guiding axons arriving at the later stages. Previously, the extracellular matrix reelin was found to be critical for ipRGCs' innervation in vLGN/IGL by screening genes differentially expressed in thalamic nuclei (Su et al 2011). Similar screening for genes coding for extracellular matrix proteins or guidance cues specifically in the vLGN but not IGL would be useful for understanding the molecular mechanisms for this nucleus-specific targeting.

Chapter 6 : Conclusions and Future Directions

6.1 Homeostatic Plasticity in *B6-DTA* Retina

Homeostatic plasticity plays an essential role in maintaining stable activity in the developing nervous system, including the retina. Although mechanisms of homeostatic plasticity have been studied extensively, it was unclear that to what extent homeostatic plasticity preserves circuit function. Using cell-type-specific manipulations *in vivo*, our experiments in the mouse retina were able to show that the characteristic sensory computations of ONα-RGCs are preserved following removal of their dominant BC input. Detailed examinations revealed that removing B6 cells from developing circuits triggers cell-type-specific rewiring, which precisely restores light response properties such as contrast sensitivity and temporal tuning of ONα-RGCs.

One question worthy of further exploration is what sensing mechanisms ONα-RGCs use to detect the significant loss of presynaptic partners. Several studies have indicated multiple pathways may work together, or in parallel, to detect perturbations (Davis 2013). The cell-type-specific rewiring observed in *B6-DTA* mice could be triggered through postsynaptic activity-dependent signaling (e.g., Ca^{2+} concentration in ONα-RGCs), presynaptic activity-dependent signaling (e.g., neurotransmission from BCs), and activity-independent mechanisms (e.g., the physical presence of B6 cells) (Davis 2013, Fernandes & Carvalho 2016, Frank 2014, MacLean et al 2003, Sutton et al 2007). Experiments including chronic hyperpolarization of ONα-RGCs by expressing potassium channels such as Kir 2.1 in wild-type retinas, and constitutive depolarization by introducing excitatory DREADDs into ONα-RGCs in *B6-DTA* retinas could clarify whether decrease in firing rate (reducing postsynaptic Ca^{2+} concentration) is sufficient to

induce the homeostatic rewiring (Wiegert et al 2017). However, suitable genetic markers for specifically targeting ONα-RGCs have yet to be identified, and overexpression of ion channels may induce other forms of homeostasis, which could complicate data interpretation (MacLean et al 2003). Examinations of anatomy and light responses of ONα-RGC circuits in mice expressing tetanus toxin light chain in B6 cells would provide insights into the role of neurotransmission in homeostatic plasticity (Henry et al 2012, Okawa et al 2014a, Okawa et al 2014c).

Our studies focused on ONα-RGC circuits. Whether other RGC circuits receiving inputs from B6 cells also restore their light response properties homeostatically in *B6-DTA* mice remains to be explored (Dunn & Wong 2014, Helmstaedter et al 2013). Comparison of multiple RGC types' activity recorded by MEA between wild-type and *B6-DTA* retinas can identify any RGC types whose light responses are influenced by removing B6 cells. However, the contribution of B6 cells to light responses of most RGC types remains unclear. As a result, a lack of significant differences between wild-type and *B6-DTA* RGC circuits could indicate homeostatic plasticity or minor roles of B6 cells in other RGC circuits.

6.2 Functional Roles of SbC-RGCs in Visual Processing

The visual world our brains perceived is built on diverse spiking patterns of distinct RGC types, each encoding selective visual features and projecting to specific brain regions (Dhande et al 2015). While much attention has focused on characterizing the light responses of distinct RGC types, our understanding of circuit mechanisms underlying these responses, of the central RGC projections, and of their contributions to visual functions is still rudimentary. In this dissertation, I identified a conserved RGC type with unusual suppressive responses to contrasts (SbC-RGCs) in mice (Tien et al 2015). I found that suppressive responses mainly result from inhibitory synaptic inputs. Taking advantage of mouse genetics, I found that the dual-transmitter VGluT3-

expressing amacrine cells provide glycinergic input to the SbC-RGCs specifically in response to small dark spots (Tien et al 2016).

While the unusual suppressive responses of SbC-RGCs provide inspiration, the contributions of SbC-RGCs to vision remain mysterious (Masland & Martin 2007, Tien et al 2015). Using an intersectional genetic approach, I preferentially labeled SbC-RGCs and mapped their central projections, including the two subcortical nuclei for image-forming functions: the SC and dLGN. SbC-RGCs also densely innervate in the vLGN, which has long been thought to be in non-image-forming visual circuits (Harrington 1997). Therefore, in the future we are aiming to address two main questions, which are related to each other: (1) the contribution of SbC-RGCs to vision, and (2) the distinct roles of SbC-RGCs' signals in SC, dLGN and vLGN.

Before pursuing these questions, it is important to confirm the central connections of SbC-RGCs either by directly brain imaging/recording or retrogradely labeling as ongoing experiments (Buzsaki et al 2015, Feinberg & Meister 2015, Jun et al 2017, Kim et al 2017). Next, we are going to use the same intersectional transgenic approach to either selectively remove SbC-RGCs by expressing DTA toxin, or selectively silence SbC-RGCs activity optogenetically or chemogenetically (Tien et al 2016, Wiegert et al 2017). We will then compare visual discrimination between wildtype (before silencing) and SbC-RGC knockout (silencing) mice (Burgess et al 2017). We can inactivate SbC-RGCs' activity globally or locally to investigate the differential contributions of individual SbC-RGCs central connections to vision (Wiegert et al 2017). It would also be worth mapping the downstream SbC-RGC circuits to further investigate how the suppressive signals contribute to visual processing (Kim et al 2016).

References

Akrouh A, Kerschensteiner D. 2013. Intersecting circuits generate precisely patterned retinal waves. *Neuron* 79: 322-34

Amir S, Stewart J. 1996. Resetting of the circadian clock by a conditioned stimulus. *Nature* 379: 542-5

Antonini A, Stryker MP. 1993. Rapid remodeling of axonal arbors in the visual cortex. *Science (New York, N.Y.)* 260: 1819-21

Apostolides PF, Trussell LO. 2013. Rapid, activity-independent turnover of vesicular transmitter content at a mixed glycine/GABA synapse. *The Journal of neuroscience : the official journal of the Society for Neuroscience* 33: 4768-81

Arshavsky VY, Lamb TD, Pugh EN, Jr. 2002. G proteins and phototransduction. *Annual review of physiology* 64: 153-87

Asari H, Meister M. 2012. Divergence of visual channels in the inner retina. *Nat Neurosci* 15: 1581-9

Azeredo da Silveira R, Roska B. 2011. Cell types, circuits, computation. *Curr Opin Neurobiol* 21: 664-71

Badea TC, Cahill H, Ecker J, Hattar S, Nathans J. 2009. Distinct roles of transcription factors brn3a and brn3b in controlling the development, morphology, and function of retinal ganglion cells. *Neuron* 61: 852-64

Badea TC, Nathans J. 2011. Morphologies of mouse retinal ganglion cells expressing transcription factors Brn3a, Brn3b, and Brn3c: analysis of wild type and mutant cells using genetically-directed sparse labeling. *Vision research* 51: 269-79

Badea TC, Wang Y, Nathans J. 2003. A noninvasive genetic/pharmacologic strategy for visualizing cell morphology and clonal relationships in the mouse. *The Journal of neuroscience : the official journal of the Society for Neuroscience* 23: 2314-22

Baden T, Berens P, Bethge M, Euler T. 2013a. Spikes in mammalian bipolar cells support temporal layering of the inner retina. *Current biology : CB* 23: 48-52

Baden T, Berens P, Franke K, Roman Roson M, Bethge M, Euler T. 2016. The functional diversity of retinal ganglion cells in the mouse. *Nature* 529: 345-50

Baden T, Schubert T, Chang L, Wei T, Zaichuk M, et al. 2013b. A tale of two retinal domains: near-optimal sampling of achromatic contrasts in natural scenes through asymmetric photoreceptor distribution. *Neuron* 80: 1206-17

Bartley AF, Huang ZJ, Huber KM, Gibson JR. 2008. Differential activity-dependent, homeostatic plasticity of two neocortical inhibitory circuits. *Journal of neurophysiology* 100: 1983-94

Behrens C, Schubert T, Haverkamp S, Euler T, Berens P. 2016. Connectivity map of bipolar cells and photoreceptors in the mouse retina. *Elife* 5

Berson DM. 2008. *Retinal ganglion cell types and their central projections*. The Senses: a comprehensive reference (Vision 1). 491-520 pp.

Berson DM, Dunn FA, Takao M. 2002. Phototransduction by retinal ganglion cells that set the circadian clock. *Science* 295: 1070-3

Betley JN, Wright CV, Kawaguchi Y, Erdelyi F, Szabo G, et al. 2009. Stringent specificity in the construction of a GABAergic presynaptic inhibitory circuit. *Cell* 139: 161-74

Blankenship AG, Feller MB. 2010. Mechanisms underlying spontaneous patterned activity in developing neural circuits. *Nature reviews. Neuroscience* 11: 18-29
Bloomfield SA, Dacheux RF. 2001. Rod vision: pathways and processing in the mammalian retina. *Progress in retinal and eye research* 20: 351-84
Borghuis BG, Marvin JS, Looger LL, Demb JB. 2013. Two-photon imaging of nonlinear glutamate release dynamics at bipolar cell synapses in the mouse retina. *J Neurosci* 33: 10972-85
Breuninger T, Puller C, Haverkamp S, Euler T. 2011. Chromatic bipolar cell pathways in the mouse retina. *The Journal of neuroscience : the official journal of the Society for Neuroscience* 31: 6504-17
Briggman KL, Helmstaedter M, Denk W. 2011. Wiring specificity in the direction-selectivity circuit of the retina. *Nature* 471: 183-8
Britten KH, Shadlen MN, Newsome WT, Movshon JA. 1992. The analysis of visual motion: a comparison of neuronal and psychophysical performance. *J Neurosci* 12: 4745-65
Buch T, Heppner FL, Tertilt C, Heinen TJ, Kremer M, et al. 2005. A Cre-inducible diphtheria toxin receptor mediates cell lineage ablation after toxin administration. *Nature methods* 2: 419-26
Burgess CP, Lak A, Steinmetz NA, Zatka-Haas P, Bai Reddy C, et al. 2017. High-Yield Methods for Accurate Two-Alternative Visual Psychophysics in Head-Fixed Mice. *Cell reports* 20: 2513-24
Burr D. 2005. Vision: in the blink of an eye. *Curr Biol* 15: R554-6
Buzsaki G, Stark E, Berenyi A, Khodagholy D, Kipke DR, et al. 2015. Tools for probing local circuits: high-density silicon probes combined with optogenetics. *Neuron* 86: 92-105
Cai D, Cohen KB, Luo T, Lichtman JW, Sanes JR. 2013. Improved tools for the Brainbow toolbox. *Nat Methods* 10: 540-7
Calkins DJ, Sterling P. 2007. Microcircuitry for two types of achromatic ganglion cell in primate fovea. *J Neurosci* 27: 2646-53
Cembrowski MS, Wang L, Sugino K, Shields BC, Spruston N. 2016. Hipposeq: a comprehensive RNA-seq database of gene expression in hippocampal principal neurons. *eLife* 5: e14997
Chalupa LM, Williams RW. 2008. *Eye, retina, and visual system of the mouse*. Cambridge, Mass.: MIT Press. xii, 754 p., 48 p. of plates pp.
Chang L, Breuninger T, Euler T. 2013. Chromatic coding from cone-type unselective circuits in the mouse retina. *Neuron* 77: 559-71
Chapot CA, Behrens C, Rogerson LE, Baden T, Pop S, et al. 2017. Local Signals in Mouse Horizontal Cell Dendrites. *Current biology : CB* 27: 3603-15 e5
Chuhma N, Mingote S, Moore H, Rayport S. 2014. Dopamine neurons control striatal cholinergic neurons via regionally heterogeneous dopamine and glutamate signaling. *Neuron* 81: 901-12
Contini M, Raviola E. 2003. GABAergic synapses made by a retinal dopaminergic neuron. *Proceedings of the National Academy of Sciences of the United States of America* 100: 1358-63
Coombs J, van der List D, Wang GY, Chalupa LM. 2006. Morphological properties of mouse retinal ganglion cells. *Neuroscience* 140: 123-36
Cooper HM, Herbin M, Nevo E. 1993. Visual system of a naturally microphthalmic mammal: the blind mole rat, Spalax ehrenbergi. *J Comp Neurol* 328: 313-50

Davis GW. 2013. Homeostatic signaling and the stabilization of neural function. *Neuron* 80: 718-28
Davis GW, Muller M. 2015. Homeostatic control of presynaptic neurotransmitter release. *Annual review of physiology* 77: 251-70
de Monasterio FM. 1978. Properties of ganglion cells with atypical receptive-field organization in retina of macaques. *J Neurophysiol* 41: 1435-49
Demb JB, Singer JH. 2015. Functional Circuitry of the Retina. *Annual Review of Vision Science* 1: 263-89
Desai NS, Cudmore RH, Nelson SB, Turrigiano GG. 2002. Critical periods for experience-dependent synaptic scaling in visual cortex. *Nature neuroscience* 5: 783-9
Dhande OS, Estevez ME, Quattrochi LE, El-Danaf RN, Nguyen PL, et al. 2013. Genetic dissection of retinal inputs to brainstem nuclei controlling image stabilization. *The Journal of neuroscience : the official journal of the Society for Neuroscience* 33: 17797-813
Dhande OS, Huberman AD. 2014. Retinal ganglion cell maps in the brain: implications for visual processing. *Curr Opin Neurobiol* 24: 133-42
Dhande OS, Stafford BK, Lim JA, Huberman AD. 2015. Contributions of Retinal Ganglion Cells to Subcortical Visual Processing and Behaviors. *Annual review of vision science* 1: 291-328
Diao Y, Cui L, Chen Y, Burbridge TJ, Han W, et al. 2017. Reciprocal Connections Between Cortex and Thalamus Contribute to Retinal Axon Targeting to Dorsal Lateral Geniculate Nucleus. *Cerebral cortex*: 1-15
Duan X, Krishnaswamy A, De la Huerta I, Sanes JR. 2014. Type II cadherins guide assembly of a direction-selective retinal circuit. *Cell* 158: 793-807
Dunn FA, Wong RO. 2012. Diverse strategies engaged in establishing stereotypic wiring patterns among neurons sharing a common input at the visual system's first synapse. *J Neurosci* 32: 10306-17
Dunn FA, Wong RO. 2014. Wiring patterns in the mouse retina: collecting evidence across the connectome, physiology and light microscopy. *J Physiol* 592: 4809-23
Ebert DH, Greenberg ME. 2013. Activity-dependent neuronal signalling and autism spectrum disorder. *Nature* 493: 327-37
Ebrey T, Koutalos Y. 2001. Vertebrate photoreceptors. *Progress in retinal and eye research* 20: 49-94
Ecker JL, Dumitrescu ON, Wong KY, Alam NM, Chen SK, et al. 2010. Melanopsin-expressing retinal ganglion-cell photoreceptors: cellular diversity and role in pattern vision. *Neuron* 67: 49-60
Eggers ED, Lukasiewicz PD. 2011. Multiple pathways of inhibition shape bipolar cell responses in the retina. *Visual neuroscience* 28: 95-108
Enroth-Cugell C, Robson JG. 1966. The contrast sensitivity of retinal ganglion cells of the cat. *J Physiol* 187: 517-52
Euler T, Detwiler PB, Denk W. 2002. Directionally selective calcium signals in dendrites of starburst amacrine cells. *Nature* 418: 845-52
Euler T, Haverkamp S, Schubert T, Baden T. 2014. Retinal bipolar cells: elementary building blocks of vision. *Nature reviews. Neuroscience* 15: 507-19
Feinberg EH, Meister M. 2015. Orientation columns in the mouse superior colliculus. *Nature* 519: 229-32

Fernandes D, Carvalho AL. 2016. Mechanisms of homeostatic plasticity in the excitatory synapse. *Journal of neurochemistry* 139: 973-96
Field DJ, Hayes A, Hess RF. 1993. Contour integration by the human visual system: evidence for a local "association field". *Vision research* 33: 173-93
Fisher LJ. 1979. Development of synaptic arrays in the inner plexiform layer of neonatal mouse retina. *J Comp Neurol* 187: 359-72
Fox MA, Sanes JR. 2007. Synaptotagmin I and II are present in distinct subsets of central synapses. *J Comp Neurol* 503: 280-96
Frank CA. 2014. How voltage-gated calcium channels gate forms of homeostatic synaptic plasticity. *Frontiers in cellular neuroscience* 8: 40
Franke K, Baden T. 2017. General features of inhibition in the inner retina. *J Physiol* 595: 5507-15
Franke K, Berens P, Schubert T, Bethge M, Euler T, Baden T. 2017. Inhibition decorrelates visual feature representations in the inner retina. *Nature* 542: 439-44
Franklin KBJ, Paxinos G. 2012. *Paxinos and Franklin's The mouse brain in stereotaxic coordinates*. 1 volume (unpaged) pp.
Gagnon D, Parent M. 2014. Distribution of VGLUT3 in highly collateralized axons from the rat dorsal raphe nucleus as revealed by single-neuron reconstructions. *PloS one* 9: e87709
Glickfeld LL, Reid RC, Andermann ML. 2014. A mouse model of higher visual cortical function. *Curr Opin Neurobiol* 24: 28-33
Godement P, Salaun J, Imbert M. 1984. Prenatal and postnatal development of retinogeniculate and retinocollicular projections in the mouse. *J Comp Neurol* 230: 552-75
Gollisch T, Meister M. 2010. Eye smarter than scientists believed: neural computations in circuits of the retina. *Neuron* 65: 150-64
Gras C, Amilhon B, Lepicard EM, Poirel O, Vinatier J, et al. 2008. The vesicular glutamate transporter VGLUT3 synergizes striatal acetylcholine tone. *Nature neuroscience* 11: 292-300
Greene MJ, Kim JS, Seung HS, EyeWirers. 2016. Analogous Convergence of Sustained and Transient Inputs in Parallel On and Off Pathways for Retinal Motion Computation. *Cell reports* 14: 1892-900
Grimes WN, Schwartz GW, Rieke F. 2014. The synaptic and circuit mechanisms underlying a change in spatial encoding in the retina. *Neuron* 82: 460-73
Grimes WN, Seal RP, Oesch N, Edwards RH, Diamond JS. 2011. Genetic targeting and physiological features of VGLUT3+ amacrine cells. *Visual neuroscience* 28: 381-92
Grimm D, Kay MA, Kleinschmidt JA. 2003. Helper virus-free, optically controllable, and two-plasmid-based production of adeno-associated virus vectors of serotypes 1 to 6. *Molecular therapy : the journal of the American Society of Gene Therapy* 7: 839-50
Grubb MS, Burrone J. 2010. Activity-dependent relocation of the axon initial segment fine-tunes neuronal excitability. *Nature* 465: 1070-4
Hannibal J, Fahrenkrug J. 2004. Target areas innervated by PACAP-immunoreactive retinal ganglion cells. *Cell and tissue research* 316: 99-113
Harrington ME. 1997. The ventral lateral geniculate nucleus and the intergeniculate leaflet: interrelated structures in the visual and circadian systems. *Neuroscience and biobehavioral reviews* 21: 705-27

Harrington ME, Nance DM, Rusak B. 1987. Double-labeling of neuropeptide Y-immunoreactive neurons which project from the geniculate to the suprachiasmatic nuclei. *Brain research* 410: 275-82

Hartveit E, Veruki ML. 2012. Electrical synapses between AII amacrine cells in the retina: Function and modulation. *Brain research* 1487: 160-72

Hattar S, Kumar M, Park A, Tong P, Tung J, et al. 2006. Central projections of melanopsin-expressing retinal ganglion cells in the mouse. *J Comp Neurol* 497: 326-49

Hattar S, Liao HW, Takao M, Berson DM, Yau KW. 2002. Melanopsin-containing retinal ganglion cells: architecture, projections, and intrinsic photosensitivity. *Science* 295: 1065-70

Haverkamp S, Wassle H. 2004. Characterization of an amacrine cell type of the mammalian retina immunoreactive for vesicular glutamate transporter 3. *The Journal of comparative neurology* 468: 251-63

Haverkamp S, Wassle H, Duebel J, Kuner T, Augustine GJ, et al. 2005. The primordial, blue-cone color system of the mouse retina. *The Journal of neuroscience : the official journal of the Society for Neuroscience* 25: 5438-45

Helmstaedter M, Briggman KL, Turaga SC, Jain V, Seung HS, Denk W. 2013. Connectomic reconstruction of the inner plexiform layer in the mouse retina. *Nature* 500: 168-74

Hengen KB, Lambo ME, Van Hooser SD, Katz DB, Turrigiano GG. 2013. Firing rate homeostasis in visual cortex of freely behaving rodents. *Neuron* 80: 335-42

Henry FE, McCartney AJ, Neely R, Perez AS, Carruthers CJ, et al. 2012. Retrograde changes in presynaptic function driven by dendritic mTORC1. *The Journal of neuroscience : the official journal of the Society for Neuroscience* 32: 17128-42

Hnasko TS, Edwards RH. 2012. Neurotransmitter corelease: mechanism and physiological role. *Annual review of physiology* 74: 225-43

Hoggarth A, McLaughlin AJ, Ronellenfitch K, Trenholm S, Vasandani R, et al. 2015. Specific wiring of distinct amacrine cells in the directionally selective retinal circuit permits independent coding of direction and size. *Neuron* 86: 276-91

Huberman AD, Manu M, Koch SM, Susman MW, Lutz AB, et al. 2008. Architecture and activity-mediated refinement of axonal projections from a mosaic of genetically identified retinal ganglion cells. *Neuron* 59: 425-38

Huberman AD, Niell CM. 2011. What can mice tell us about how vision works? *Trends in neurosciences* 34: 464-73

Ichinose T, Fyk-Kolodziej B, Cohn J. 2014. Roles of ON cone bipolar cell subtypes in temporal coding in the mouse retina. *The Journal of neuroscience : the official journal of the Society for Neuroscience* 34: 8761-71

Ito S, Feldheim DA, Litke AM. 2017. Segregation of Visual Response Properties in the Mouse Superior Colliculus and Their Modulation during Locomotion. *The Journal of neuroscience : the official journal of the Society for Neuroscience* 37: 8428-43

Jacobs GH. 1993. The distribution and nature of colour vision among the mammals. *Biological reviews of the Cambridge Philosophical Society* 68: 413-71

Jacoby J, Zhu Y, DeVries SH, Schwartz GW. 2015. An Amacrine Cell Circuit for Signaling Steady Illumination in the Retina. *Cell reports*

Jadzinsky PD, Baccus SA. 2013. Transformation of visual signals by inhibitory interneurons in retinal circuits. *Annual review of neuroscience* 36: 403-28

Johnson J, Sherry DM, Liu X, Fremeau RT, Jr., Seal RP, et al. 2004. Vesicular glutamate transporter 3 expression identifies glutamatergic amacrine cells in the rodent retina. *The Journal of comparative neurology* 477: 386-98
Johnson KP, Zhao L, Kerschensteiner D. 2018. A Pixel-Encoder Retinal Ganglion Cell with Spatially Offset Excitatory and Inhibitory Receptive Fields. *Cell reports* 22: 1462-72
Jonas P, Bischofberger J, Sandkuhler J. 1998. Corelease of two fast neurotransmitters at a central synapse. *Science* 281: 419-24
Jun JJ, Steinmetz NA, Siegle JH, Denman DJ, Bauza M, et al. 2017. Fully integrated silicon probes for high-density recording of neural activity. *Nature* 551: 232-36
Kefalov VJ. 2012. Rod and cone visual pigments and phototransduction through pharmacological, genetic, and physiological approaches. *The Journal of biological chemistry* 287: 1635-41
Kerschensteiner D. 2014. Spontaneous Network Activity and Synaptic Development. *The Neuroscientist : a review journal bringing neurobiology, neurology and psychiatry* 20: 272-90
Kerschensteiner D, Morgan JL, Parker ED, Lewis RM, Wong RO. 2009. Neurotransmission selectively regulates synapse formation in parallel circuits in vivo. *Nature* 460: 1016-20
Khaliq ZM, Raman IM. 2005. Axonal propagation of simple and complex spikes in cerebellar Purkinje neurons. *J Neurosci* 25: 454-63
Kim CK, Adhikari A, Deisseroth K. 2017. Integration of optogenetics with complementary methodologies in systems neuroscience. *Nature reviews. Neuroscience* 18: 222-35
Kim EJ, Jacobs MW, Ito-Cole T, Callaway EM. 2016. Improved Monosynaptic Neural Circuit Tracing Using Engineered Rabies Virus Glycoproteins. *Cell reports* 15: 692-99
Kim IJ, Zhang Y, Meister M, Sanes JR. 2010. Laminar restriction of retinal ganglion cell dendrites and axons: subtype-specific developmental patterns revealed with transgenic markers. *J Neurosci* 30: 1452-62
Kim T, Soto F, Kerschensteiner D. 2015. An excitatory amacrine cell detects object motion and provides feature-selective input to ganglion cells in the mouse retina. *eLife* 4
Klugmann M, Symes CW, Leichtlein CB, Klaussner BK, Dunning J, et al. 2005. AAV-mediated hippocampal expression of short and long Homer 1 proteins differentially affect cognition and seizure activity in adult rats. *Molecular and cellular neurosciences* 28: 347-60
Krishnaswamy A, Yamagata M, Duan X, Hong YK, Sanes JR. 2015. Sidekick 2 directs formation of a retinal circuit that detects differential motion. *Nature* 524: 466-70
Lagali PS, Balya D, Awatramani GB, Munch TA, Kim DS, et al. 2008. Light-activated channels targeted to ON bipolar cells restore visual function in retinal degeneration. *Nat Neurosci* 11: 667-75
Lee S, Chen L, Chen M, Ye M, Seal RP, Zhou JZ. 2014. An Unconventional Glutamatergic Circuit in the Retina Formed by vGluT3 Amacrine Cells. *Neuron* 84: 708-15
Lee S, Kim K, Zhou ZJ. 2010. Role of ACh-GABA cotransmission in detecting image motion and motion direction. *Neuron* 68: 1159-72
Lee S, Zhang Y, Chen M, Zhou ZJ. 2016. Segregated Glycine-Glutamate Co-transmission from vGluT3 Amacrine Cells to Contrast-Suppressed and Contrast-Enhanced Retinal Circuits. *Neuron*
Levick WR. 1967. Receptive fields and trigger features of ganglion cells in the visual streak of the rabbits retina. *J Physiol* 188: 285-307

Liang Z, Freed MA. 2010. The ON pathway rectifies the OFF pathway of the mammalian retina. *The Journal of neuroscience : the official journal of the Society for Neuroscience* 30: 5533-43
Lyubarsky AL, Daniele LL, Pugh EN, Jr. 2004. From candelas to photoisomerizations in the mouse eye by rhodopsin bleaching in situ and the light-rearing dependence of the major components of the mouse ERG. *Vision Res* 44: 3235-51
Mackay DM. 1970. Elevation of visual threshold by displacement of retinal image. *Nature* 225: 90-2
MacLean JN, Zhang Y, Johnson BR, Harris-Warrick RM. 2003. Activity-Independent Homeostasis in Rhythmically Active Neurons. *Neuron* 37: 109-20
Madisen L, Mao T, Koch H, Zhuo JM, Berenyi A, et al. 2012. A toolbox of Cre-dependent optogenetic transgenic mice for light-induced activation and silencing. *Nat Neurosci* 15: 793-802
Madisen L, Zwingman TA, Sunkin SM, Oh SW, Zariwala HA, et al. 2010. A robust and high-throughput Cre reporting and characterization system for the whole mouse brain. *Nat Neurosci* 13: 133-40
Maffei A, Fontanini A. 2009. Network homeostasis: a matter of coordination. *Curr Opin Neurobiol* 19: 168-73
Maffei A, Nelson SB, Turrigiano GG. 2004. Selective reconfiguration of layer 4 visual cortical circuitry by visual deprivation. *Nature neuroscience* 7: 1353-9
Magnus CJ, Lee PH, Atasoy D, Su HH, Looger LL, Sternson SM. 2011. Chemical and genetic engineering of selective ion channel-ligand interactions. *Science (New York, N.Y.)* 333: 1292-6
Margolis DJ, Detwiler PB. 2007. Different mechanisms generate maintained activity in ON and OFF retinal ganglion cells. *The Journal of neuroscience : the official journal of the Society for Neuroscience* 27: 5994-6005
Marshak DW. 1989. Peptidergic neurons of the macaque monkey retina. *Neuroscience research. Supplement : the official journal of the Japan Neuroscience Society* 10: S117-30
Marshak DW, Mills SL. 2014. Short-wavelength cone-opponent retinal ganglion cells in mammals. *Visual neuroscience* 31: 165-75
Martin PR. 1986. The projection of different retinal ganglion cell classes to the dorsal lateral geniculate nucleus in the hooded rat. *Experimental brain research* 62: 77-88
Masland RH. 2001a. The fundamental plan of the retina. *Nat Neurosci* 4: 877-86
Masland RH. 2001b. Neuronal diversity in the retina. *Curr Opin Neurobiol* 11: 431-6
Masland RH. 2012a. The neuronal organization of the retina. *Neuron* 76: 266-80
Masland RH. 2012b. The tasks of amacrine cells. *Visual neuroscience* 29: 3-9
Masland RH, Martin PR. 2007. The unsolved mystery of vision. *Current biology : CB* 17: R577-82
Matsuoka RL, Chivatakarn O, Badea TC, Samuels IS, Cahill H, et al. 2011a. Class 5 transmembrane semaphorins control selective Mammalian retinal lamination and function. *Neuron* 71: 460-73
Matsuoka RL, Nguyen-Ba-Charvet KT, Parray A, Badea TC, Chedotal A, Kolodkin AL. 2011b. Transmembrane semaphorin signalling controls laminar stratification in the mammalian retina. *Nature* 470: 259-63
McNeill DS, Sheely CJ, Ecker JL, Badea TC, Morhardt D, et al. 2011. Development of melanopsin-based irradiance detecting circuitry. *Neural development* 6: 8

Monavarfeshani A, Sabbagh U, Fox MA. 2017. Not a one-trick pony: Diverse connectivity and functions of the rodent lateral geniculate complex. *Visual neuroscience* 34: E012
Morgan JL, Dhingra A, Vardi N, Wong RO. 2006. Axons and dendrites originate from neuroepithelial-like processes of retinal bipolar cells. *Nature neuroscience* 9: 85-92
Morgan JL, Lichtman JW. 2013. Why not connectomics? *Nature methods* 10: 494-500
Morgan JL, Schubert T, Wong RO. 2008. Developmental patterning of glutamatergic synapses onto retinal ganglion cells. *Neural development* 3: 8
Morgan JL, Soto F, Wong RO, Kerschensteiner D. 2011. Development of cell type-specific connectivity patterns of converging excitatory axons in the retina. *Neuron* 71: 1014-21
Morin LP. 2013. Neuroanatomy of the extended circadian rhythm system. *Experimental neurology* 243: 4-20
Morin LP, Studholme KM. 2014. Retinofugal projections in the mouse. *J Comp Neurol* 522: 3733-53
Murphy GJ, Rieke F. 2006. Network variability limits stimulus-evoked spike timing precision in retinal ganglion cells. *Neuron* 52: 511-24
Nawy S, Jahr CE. 1990. Suppression by glutamate of cGMP-activated conductance in retinal bipolar cells. *Nature* 346: 269-71
Nawy S, Jahr CE. 1991. cGMP-gated conductance in retinal bipolar cells is suppressed by the photoreceptor transmitter. *Neuron* 7: 677-83
Niell CM, Stryker MP. 2008. Highly selective receptive fields in mouse visual cortex. *The Journal of neuroscience : the official journal of the Society for Neuroscience* 28: 7520-36
Niell CM, Stryker MP. 2010. Modulation of visual responses by behavioral state in mouse visual cortex. *Neuron* 65: 472-9
Noda H, Adey WR. 1974. Retinal ganglion cells of the cat transfer information on saccadic eye movement and quick target motion. *Brain Res* 70: 340-5
Noh J, Seal RP, Garver JA, Edwards RH, Kandler K. 2010. Glutamate co-release at GABA/glycinergic synapses is crucial for the refinement of an inhibitory map. *Nature neuroscience* 13: 232-8
Nusbaum MP, Blitz DM, Swensen AM, Wood D, Marder E. 2001. The roles of co-transmission in neural network modulation. *Trends in neurosciences* 24: 146-54
O'Malley DM, Sandell JH, Masland RH. 1992. Co-release of acetylcholine and GABA by the starburst amacrine cells. *The Journal of neuroscience : the official journal of the Society for Neuroscience* 12: 1394-408
Oesch NW, Kothmann WW, Diamond JS. 2011. Illuminating synapses and circuitry in the retina. *Curr Opin Neurobiol* 21: 238-44
Oh SW, Harris JA, Ng L, Winslow B, Cain N, et al. 2014. A mesoscale connectome of the mouse brain. *Nature* 508: 207-14
Okawa H, Della Santina L, Schwartz GW, Rieke F, Wong RO. 2014a. Interplay of cell-autonomous and nonautonomous mechanisms tailors synaptic connectivity of converging axons in vivo. *Neuron* 82: 125-37
Okawa H, Hoon M, Yoshimatsu T, Della Santina L, Wong RO. 2014b. Illuminating the multifaceted roles of neurotransmission in shaping neuronal circuitry. *Neuron* 83: 1303-18
Okawa H, Hoon M, Yoshimatsu T, Della Santina L, Wong ROL. 2014c. Illuminating the multifaceted roles of neurotransmission in shaping neuronal circuitry. *Neuron* 83: 1303-18

Onoa B, Li H, Gagnon-Bartsch JA, Elias LA, Edwards RH. 2010. Vesicular monoamine and glutamate transporters select distinct synaptic vesicle recycling pathways. *The Journal of neuroscience : the official journal of the Society for Neuroscience* 30: 7917-27

Osterhout JA, El-Danaf RN, Nguyen PL, Huberman AD. 2014. Birthdate and outgrowth timing predict cellular mechanisms of axon target matching in the developing visual pathway. *Cell reports* 8: 1006-17

Osterhout JA, Josten N, Yamada J, Pan F, Wu SW, et al. 2011. Cadherin-6 mediates axon-target matching in a non-image-forming visual circuit. *Neuron* 71: 632-9

Oyster CW, Simpson JI, Takahashi ES, Soodak RE. 1980. Retinal ganglion cells projecting to the rabbit accessory optic system. *J Comp Neurol* 190: 49-61

Park HT, Baek SY, Kim BS, Kim JB, Kim JJ. 1993. Profile of Fos-like immunoreactivity induction by light stimuli in the intergeniculate leaflet is different from that of the suprachiasmatic nucleus. *Brain research* 610: 334-9

Pickard GE. 1985. Bifurcating axons of retinal ganglion cells terminate in the hypothalamic suprachiasmatic nucleus and the intergeniculate leaflet of the thalamus. *Neuroscience letters* 55: 211-7

Piscopo DM, El-Danaf RN, Huberman AD, Niell CM. 2013. Diverse visual features encoded in mouse lateral geniculate nucleus. *The Journal of neuroscience : the official journal of the Society for Neuroscience* 33: 4642-56

Pozo K, Goda Y. 2010. Unraveling mechanisms of homeostatic synaptic plasticity. *Neuron* 66: 337-51

Pu M, Pickard GE. 1996. Ventral lateral geniculate nucleus afferents to the suprachiasmatic nucleus in the cat. *Brain research* 725: 247-51

Purves D, Lichtman JW. 1980. Elimination of synapses in the developing nervous system. *Science (New York, N.Y.)* 210: 153-7

Ramocki MB, Zoghbi HY. 2008. Failure of neuronal homeostasis results in common neuropsychiatric phenotypes. *Nature* 455: 912-8

Ren J, Qin C, Hu F, Tan J, Qiu L, et al. 2011. Habenula "cholinergic" neurons co-release glutamate and acetylcholine and activate postsynaptic neurons via distinct transmission modes. *Neuron* 69: 445-52

Riccomagno MM, Kolodkin AL. 2015. Sculpting neural circuits by axon and dendrite pruning. *Annu Rev Cell Dev Biol* 31: 779-805

Rivlin-Etzion M, Zhou K, Wei W, Elstrott J, Nguyen PL, et al. 2011. Transgenic mice reveal unexpected diversity of on-off direction-selective retinal ganglion cell subtypes and brain structures involved in motion processing. *The Journal of neuroscience : the official journal of the Society for Neuroscience* 31: 8760-9

Rodieck RW. 1967. Receptive fields in the cat retina: a new type. *Science* 157: 90-2

Root DH, Mejias-Aponte CA, Zhang S, Wang HL, Hoffman AF, et al. 2014. Single rodent mesohabenular axons release glutamate and GABA. *Nature neuroscience* 17: 1543-51

Rosenberg D, Artoul S, Segal AC, Kolodney G, Radzishevsky I, et al. 2013. Neuronal D-serine and glycine release via the Asc-1 transporter regulates NMDA receptor-dependent synaptic activity. *The Journal of neuroscience : the official journal of the Society for Neuroscience* 33: 3533-44

Roska B, Werblin F. 2003. Rapid global shifts in natural scenes block spiking in specific ganglion cell types. *Nat Neurosci* 6: 600-8

Ross J, Morrone MC, Goldberg ME, Burr DC. 2001. Changes in visual perception at the time of saccades. *Trends Neurosci* 24: 113-21
Roth MM, Dahmen JC, Muir DR, Imhof F, Martini FJ, Hofer SB. 2016. Thalamic nuclei convey diverse contextual information to layer 1 of visual cortex. *Nature neuroscience* 19: 299-307
Rousso DL, Qiao M, Kagan RD, Yamagata M, Palmiter RD, Sanes JR. 2016. Two Pairs of ON and OFF Retinal Ganglion Cells Are Defined by Intersectional Patterns of Transcription Factor Expression. *Cell reports* 15: 1930-44
Sachs GM, Jacobson M, Caviness VS, Jr. 1986. Postnatal changes in arborization patterns of murine retinocollicular axons. *J Comp Neurol* 246: 395-408
Sakatani T, Isa T. 2007. Quantitative analysis of spontaneous saccade-like rapid eye movements in C57BL/6 mice. *Neurosci Res* 58: 324-31
Sanes JR, Masland RH. 2015. The types of retinal ganglion cells: current status and implications for neuronal classification. *Annual review of neuroscience* 38: 221-46
Sanes JR, Yamagata M. 2009. Many paths to synaptic specificity. *Annu Rev Cell Dev Biol* 25: 161-95
Saunders A, Granger AJ, Sabatini BL. 2015. Corelease of acetylcholine and GABA from cholinergic forebrain neurons. *eLife* 4
Schindelin J, Arganda-Carreras I, Frise E, Kaynig V, Longair M, et al. 2012. Fiji: an open-source platform for biological-image analysis. *Nature methods* 9: 676-82
Schmitz F, Konigstorfer A, Sudhof TC. 2000. RIBEYE, a component of synaptic ribbons: a protein's journey through evolution provides insight into synaptic ribbon function. *Neuron* 28: 857-72
Schwartz GW, Okawa H, Dunn FA, Morgan JL, Kerschensteiner D, et al. 2012. The spatial structure of a nonlinear receptive field. *Nat Neurosci* 15: 1572-80
Seabrook TA, Burbridge TJ, Crair MC, Huberman AD. 2017. Architecture, Function, and Assembly of the Mouse Visual System. *Annual review of neuroscience* 40: 499-538
Shekhar K, Lapan SW, Whitney IE, Tran NM, Macosko EZ, et al. 2016. Comprehensive Classification of Retinal Bipolar Neurons by Single-Cell Transcriptomics. *Cell* 166: 1308-23 e30
Sivyer B, Taylor WR, Vaney DI. 2010. Uniformity detector retinal ganglion cells fire complex spikes and receive only light-evoked inhibition. *Proc Natl Acad Sci U S A* 107: 5628-33
Sivyer B, Vaney DI. 2010. Dendritic morphology and tracer-coupling pattern of physiologically identified transient uniformity detector ganglion cells in rabbit retina. *Visual neuroscience* 27: 159-70
Slomowitz E, Styr B, Vertkin I, Milshtein-Parush H, Nelken I, et al. 2015. Interplay between population firing stability and single neuron dynamics in hippocampal networks. *eLife* 4
Soto F, Bleckert A, Lewis R, Kang Y, Kerschensteiner D, et al. 2011. Coordinated increase in inhibitory and excitatory synapses onto retinal ganglion cells during development. *Neural development* 6: 31
Soto F, Ma X, Cecil JL, Vo BQ, Culican SM, Kerschensteiner D. 2012. Spontaneous activity promotes synapse formation in a cell-type-dependent manner in the developing retina. *The Journal of neuroscience : the official journal of the Society for Neuroscience* 32: 5426-39

Soto F, Watkins KL, Johnson RE, Schottler F, Kerschensteiner D. 2013. NGL-2 regulates pathway-specific neurite growth and lamination, synapse formation, and signal transmission in the retina. *J Neurosci* 33: 11949-59
Sparks DL. 1986. Translation of sensory signals into commands for control of saccadic eye movements: role of primate superior colliculus. *Physiological reviews* 66: 118-71
Strata P, Harvey R. 1999. Dale's principle. *Brain research bulletin* 50: 349-50
Su J, Haner CV, Imbery TE, Brooks JM, Morhardt DR, et al. 2011. Reelin is required for class-specific retinogeniculate targeting. *The Journal of neuroscience : the official journal of the Society for Neuroscience* 31: 575-86
Sumbul U, Song S, McCulloch K, Becker M, Lin B, et al. 2014. A genetic and computational approach to structurally classify neuronal types. *Nat Commun* 5: 3512
Sumitomo I, Sugitani M, Fukuda Y, Iwama K. 1979. Properties of cells responding to visual stimuli in the rat ventral lateral geniculate nucleus. *Experimental neurology* 66: 721-36
Sutton MA, Taylor AM, Ito HT, Pham A, Schuman EM. 2007. Postsynaptic Decoding of Neural Activity: eEF2 as a Biochemical Sensor Coupling Miniature Synaptic Transmission to Local Protein Synthesis. *Neuron* 55: 648-61
Tailby C, Solomon SG, Dhruv NT, Majaj NJ, Sokol SH, Lennie P. 2007. A new code for contrast in the primate visual pathway. *J Neurosci* 27: 3904-9
Taniguchi H, He M, Wu P, Kim S, Paik R, et al. 2011. A resource of Cre driver lines for genetic targeting of GABAergic neurons in cerebral cortex. *Neuron* 71: 995-1013
Tasic B, Menon V, Nguyen TN, Kim TK, Jarsky T, et al. 2016. Adult mouse cortical cell taxonomy revealed by single cell transcriptomics. *Nature neuroscience* 19: 335-46
Tien NW, Kim T, Kerschensteiner D. 2016. Target-Specific Glycinergic Transmission from VGluT3-Expressing Amacrine Cells Shapes Suppressive Contrast Responses in the Retina. *Cell Rep* 15: 1369-75
Tien NW, Pearson JT, Heller CR, Demas J, Kerschensteiner D. 2015. Genetically Identified Suppressed-by-Contrast Retinal Ganglion Cells Reliably Signal Self-Generated Visual Stimuli. *J Neurosci* 35: 10815-20
Tien NW, Soto F, Kerschensteiner D. 2017. Homeostatic Plasticity Shapes Cell-Type-Specific Wiring in the Retina. *Neuron* 94: 656-65 e4
Tritsch NX, Ding JB, Sabatini BL. 2012. Dopaminergic neurons inhibit striatal output through non-canonical release of GABA. *Nature* 490: 262-6
Turrigiano GG. 2008. The self-tuning neuron: synaptic scaling of excitatory synapses. *Cell* 135: 422-35
Turrigiano GG, Leslie KR, Desai NS, Rutherford LC, Nelson SB. 1998. Activity-dependent scaling of quantal amplitude in neocortical neurons. *Nature* 391: 892-6
Turrigiano GG, Nelson SB. 2004. Homeostatic plasticity in the developing nervous system. *Nature reviews. Neuroscience* 5: 97-107
Ueda Y, Iwakabe H, Masu M, Suzuki M, Nakanishi S. 1997. The mGluR6 5' upstream transgene sequence directs a cell-specific and developmentally regulated expression in retinal rod and ON-type cone bipolar cells. *J Neurosci* 17: 3014-23
Vaaga CE, Borisovska M, Westbrook GL. 2014. Dual-transmitter neurons: functional implications of co-release and co-transmission. *Current opinion in neurobiology* 29: 25-32
Van Essen DC, Anderson CH, Felleman DJ. 1992. Information processing in the primate visual system: an integrated systems perspective. *Science* 255: 419-23

Van Hooser SD. 2007. Similarity and diversity in visual cortex: is there a unifying theory of cortical computation? *The Neuroscientist : a review journal bringing neurobiology, neurology and psychiatry* 13: 639-56
Vaney DI. 1986. Morphological identification of serotonin-accumulating neurons in the living retina. *Science* 233: 444-6
Wang L, Krauzlis RJ. 2018. Visual Selective Attention in Mice. *Current biology : CB* 28: 676-85 e4
Wang YV, Weick M, Demb JB. 2011. Spectral and temporal sensitivity of cone-mediated responses in mouse retinal ganglion cells. *J Neurosci* 31: 7670-81
Wassle H, Puller C, Muller F, Haverkamp S. 2009. Cone contacts, mosaics, and territories of bipolar cells in the mouse retina. *J Neurosci* 29: 106-17
Wefelmeyer W, Puhl CJ, Burrone J. 2016. Homeostatic Plasticity of Subcellular Neuronal Structures: From Inputs to Outputs. *Trends in neurosciences* 39: 656-67
Wei P, Liu N, Zhang Z, Liu X, Tang Y, et al. 2015. Processing of visually evoked innate fear by a non-canonical thalamic pathway. *Nat Commun* 6: 6756
Wei W, Hamby AM, Zhou K, Feller MB. 2011. Development of asymmetric inhibition underlying direction selectivity in the retina. *Nature* 469: 402-6
Werblin FS. 2011. The retinal hypercircuit: a repeating synaptic interactive motif underlying visual function. *J Physiol* 589: 3691-702
Wiegert JS, Mahn M, Prigge M, Printz Y, Yizhar O. 2017. Silencing Neurons: Tools, Applications, and Experimental Constraints. *Neuron* 95: 504-29
Williams ME, de Wit J, Ghosh A. 2010. Molecular mechanisms of synaptic specificity in developing neural circuits. *Neuron* 68: 9-18
Wojcik SM, Katsurabayashi S, Guillemin I, Friauf E, Rosenmund C, et al. 2006. A shared vesicular carrier allows synaptic corelease of GABA and glycine. *Neuron* 50: 575-87
Yamagata M, Sanes JR. 2008. Dscam and Sidekick proteins direct lamina-specific synaptic connections in vertebrate retina. *Nature* 451: 465-9
Yamagata M, Sanes JR. 2012. Expanding the Ig superfamily code for laminar specificity in retina: expression and role of contactins. *J Neurosci* 32: 14402-14
Yogev S, Shen K. 2014. Cellular and molecular mechanisms of synaptic specificity. *Annu Rev Cell Dev Biol* 30: 417-37
Yonehara K, Balint K, Noda M, Nagel G, Bamberg E, Roska B. 2011. Spatially asymmetric reorganization of inhibition establishes a motion-sensitive circuit. *Nature* 469: 407-10
Yu CR, Power J, Barnea G, O'Donnell S, Brown HE, et al. 2004. Spontaneous neural activity is required for the establishment and maintenance of the olfactory sensory map. *Neuron* 42: 553-66
Zaghloul KA, Boahen K, Demb JB. 2003. Different circuits for ON and OFF retinal ganglion cells cause different contrast sensitivities. *J Neurosci* 23: 2645-54
Zhang S, Qi J, Li X, Wang HL, Britt JP, et al. 2015. Dopaminergic and glutamatergic microdomains in a subset of rodent mesoaccumbens axons. *Nature neuroscience* 18: 386-92
Zhu Y, Xu J, Hauswirth WW, DeVries SH. 2014. Genetically targeted binary labeling of retinal neurons. *J Neurosci* 34: 7845-61
Zmarz P, Keller GB. 2016. Mismatch Receptive Fields in Mouse Visual Cortex. *Neuron* 92: 766-72